Analysis of the influence of negatively buoyant jets on curved open-channel flow by means of numerical and experimental methods

Xueming Wang

Thesis submitted to the University of Ottawa
in partial Fulfillment of the requirements for the
Doctorate in Philosophy degree in Civil Engineering

Department of Civil Engineering
Faculty of Engineering
University of Ottawa

Abstract

In urban areas, discharging wastewater into rivers is a common way to dispose of contaminants, and it is usually the most economical. Accurate information about how effluents are distributed in the receiving water body is desirable when designing industrial plants. Flow structures will be influenced by an effluent's dilution processes during the mixing. Meanwhile, the cross-stream motions resulting from the streamline curvature can redistribute both the velocity and the shear stress, which favors the mixing behavior compared to a straight channel. However, the interactions between jet mixing behavior and the bend flow requires further investigation.

In the present study, jets with different densities were discharged horizontally into a laboratory flume with a 135-degree open channel bend, and both the main and secondary flow behaviors in the bend were observed after the introduction of effluents. The acquired three-dimensional velocity data were used to validate numerical models of the effluent-bend flow. Numerical turbulence models such as the standard k-ε eddy viscosity model, non-linear k-ε model (Shih quadratic k-ε), and the k-ω SST (shear stress transport) model were employed to evaluate their accuracy. OpenFOAM was selected in the analysis for proposing better numerical models since it gives high-quality results to individualized complex fluid flows, and as an open source CFD software it can be beneficial to further develop and maintain.

The first part of this study presents the implementation of the physical modelling of the proposed problems. Detailed descriptions of the experimental process were elaborated. Specifically, the three velocity components at four cross-sectional planes in the bend section were measured with and without saltwater jets by using the stereo Particle Image Velocimetry (PIV)

technique in the laboratory flume. The experimental results show that the more pronounced effects with the jets were found at the beginning and exit of the bend. Although the jets had little effect on the maximum streamwise velocity, it was found that the occurrence of the negatively buoyant jets would affect the patterns and properties of the secondary flow in the bend.

The second part of this study investigated the mechanisms underlying the two cells system, particularly when interacting with a discharged effluent jet. Detailed experimental data were used in interpreting the large center-region cell as well as small structures in the 135-degree open channel bend. A term-by-term analysis of the downstream vorticity equation was executed to investigate the various mechanisms underlying these cross-stream flow motions considering the influence of the negatively buoyant jets. The results indicated the generation and the dissipation of the streamwise vorticity with the effective terms of the vorticity equation.

The third part of this study evaluated the performance of three different turbulence models with the experimental measurements. It can be concluded that fully 3D numerical models are capable of simulating the primary flow pattern in a strongly curved channel with the presence of a negatively buoyant jet. The comparison also shows that, although the outer bank cell was not predicted, the k-omega SST model can satisfactorily predict some of the smaller flow features in bend flow, such as the inner bank circulation cell and the overall form of the vorticity distributions. The results enable more reliable predictions for the characteristics and development of jets in a bend.

Acknowledgements

I would like to express my utmost gratitude to my supervisors, Dr. Majid Mohammadian and Dr. Colin Rennie, because it is impossible for me to start this research without their assistance. I appreciate their all-encompassing guidance, constant encouragement, and the most patient help very much, without those, I would never develop a strong passion for the field of water resources engineering.

I would like to acknowledge Mark Lapointe, Xinyun Wang, Ruoyao Ou, Shilong Liu, at the Water Resources Engineering Laboratory (University of Ottawa) for their assistance in preparing and conducting the experiments.

I would like to thank the China Scholarship Council (CSC) for providing me the scholarship and financial support for my graduate study.

I would like to thank my parents, Dianzhang Wang and Zhonglin Yuan who are encouraging and supporting me to become engaged in water resources engineering in the first place. I would also like to thank my husband Lifan Liu, for his unconditional love and support, and my parents in law, Kehun Liu and Xiaoyu Zhao. They have spent a lot more time than me in taking care of me and my family and are very supportive for my studies and career plans.

Last but not least, I would like to thank my friends at the University of Ottawa, such as Amir Gharavi, Behnaz Ghodoosipou, Shilong Liu, Yarzar Tun, Xiaohui Yan, for providing the support and friendship that I needed.

Table of Contents

List of Figures

List of Tables

List of Symbols

a_0	jet initial cross-sectional area (m^2)
B/b	bend width (m)
D	isotropic diffusion coefficient
D_j	nozzle diameter (m)
F_0	Froude number of jets
Fr	densimetric Froude number
g	gravitational acceleration (m/s^2)
H	water depth (m)
k	kinetic energy
L_b	plume/crossflow length scale (m)
L_m	jet/crossflow length scale (m)
L_Q	Source length scale (m)
L_T	puff/thermal transition length scale (m)
L_M	Momentum length scale (m)
M_0	Kinematic momentum flux (m^4/s^2)
P	the pressure (N/m^2)
p_{rgh}	hydrostatic pressure for the pressure calculations

Q	flow rate (m^3/s)
R_{cf}	crossflow parameter
Rc	curvature radius (m)
Rf	curvature-flux-Richardson number
Re	Reynolds number of the main flow
S_{ij}	the strain tensor
U	flow velocity (m/s)
u_i	velocity in x,y,z direction (m/s)
u'_s, u'_n, u'_z	fluctuating velocity components (m/s)
u_0	velocity of the buoyant jets (m/s)
u_a	ambient water velocity (m/s)
u_j	jet velocity (m/s)
Um	main flow velocity (m/s)
Us	jet discharging velocity (m/s)
$u_{s\text{-}depth}$	depth-averaged streamwise velocity (m/s)
u_{smax}	maximum streamwise velocity (m/s)
v_s, v_n, v_z	velocities in the streamwise, transverse, and vertical direction (m/s)
S	salinity and dilution

t	time (s)
x_i	the coordinates in Cartesian frame
δ_{ij}	the Kronecker delta
ϵ	dissipation rate for k in *k-ε*
μ	molecular viscosity (N.s/m^2)
σ	angle measured counterclockwise to the horizontal
σ_k	a closure coefficient
τ_{ij}	Reynolds stress
τ_{nl}	non-linear stress
υ	kinematic viscosity (m^2/s)
υ_t	the turbulent eddy viscosity (m^2/s)
ω_n, ω_z	the n- and z-components of the vorticity
ω_s	vorticity vector in the streamwise direction
ϕ	the scalar concentration
θ	angle measured counterclockwise to the streamwise direction (°)

List of Acronyms

ADV	acoustic Doppler velocimetry;
ADCP	Acoustic Doppler current profiler
ASM	algebraic stress models
CFD	computational fluid dynamics;
DES	detached-eddy simulation;
JICR	jet in cross-flow
LES	large-eddy simulation;
LDA	laser-Doppler Anemometry
LIF	laser-Induced Fluorescence
NS	Navier Stokes
OBC	outer bank cell
OpenFOAM	open-source field operation and manipulation;
PIV	particle image velocimetry;
PTV	particle tracking velocimetry;
RANS	Reynolds-Averaged Navier-Stokes equations;
RNG	renormalization group
SGS	subgrid scale;

SIMPLEC	velocity-pressure-free-surface coupled correction
SST	shear stress transport;
VOF	volume of fluid;
1D	one-dimensional;
2D	two-dimensional;
3D	three-dimensional

Chapter 1 Introduction

1.1 Introduction

Natural rivers serve as channels for transporting water and sediment. Each river has its own characteristics due to unique topographical and morphological conditions, climate impacts, and biological and ecological functions. In addition to the relatively shallow water depth, meandering is considered to be another ordinary feature in natural rivers. It is almost impossible to find a straight river section with a length longer than 10 channel-widths (LEOPOLD, 1960). River bends caused by morphodynamical processes have drawn much attention, since flow patterns in bends are more complicated than those in straight reaches. The reason behind the complexity of the flow structures in a bend is the centrifugal force applied to the flow, which causes redistributions in the velocity and stress in the channel. The unbalanced stress distribution generates secondary currents and results in the highly turbulent flow structures in a bend. Generally, there are two circulation cells caused by the streamline curvature, i.e., the classical helical flow which covers a large part of the cross-section and a weaker counter-rotating cell at the outer bank side. Many researchers have been working on interpreting velocity profiles in channel bends, especially the role of turbulence, yet an accurate prediction of 3D flow structures remains a prevalent question.

In natural meandering rivers, the riverbed is always evolving since the flow creates pools at the outer bank region and point bars along the inner bank. Changes in the shape of cross-sections and bathymetry lead to variations in water depth, which then contribute directly to the redistribution of velocity. The altered flow structure causes negative or positive pressure gradients in the flow, and pressure gradients affect the flow behavior especially for the separation of the boundary layers (Constantinescu et al., 2011). For instance, sediment deposits at the inner bank reduce the cross-section area, which accelerates the flow passing this zone, which is also known as "topographic steering" toward the channel thalweg (Constantinescu et al. 2013). Additional complications may appear when geometry of the river courses display large-scale morphodynamical signatures; essentially, the velocity distributions, secondary flow development, turbulence structures, as well as the shear stress would all be affected (Abad and García, 2009a). A lot of researchers have been working on flow structures resulting from special morphological features within bends, such as horizontal flow recirculation (Ferguson et al., 2003; Blanckaert et al., 2013), flow separation (Andrle, 1994; Beltaos et al., 2012), and streamwise oriented vortical cells (Constantinescu et al. 2013). In other words, there is a complicated interaction between the secondary flow and the flow over the bed forms when meandering channels contain bed forms. The aim of the present study is to minimize extra complication from the flow and to investigate how the jets would influence the bend structure. Therefore, we need a relatively large jet and a simple configuration bend flow, especially the two circulation-cell pattern. The formation of the outer bank cell is favored by rough, steep outer banks and intermediate to near bankfull flow stages (Hey and Thorne, 1975; Bathurst et al., 1977; Markham and Thorne, 1992, Engel and Rhoads, 2016). Hence, a flat, smooth bed (without sediment) condition has been considered to avoid further complexity.

Experimental or physical model investigations and numerical simulations are considered to be feasible and reliable approaches to study the streamline curvature. There has been a substantial amount of experimental research, both in the field and in laboratories, leading to the earlier works about the understanding of flow behaviors in open channel bends (Frothingham and Rhoads, 2003, Nanson, 2010; Schnauder and Sukhodolov; 2012, Engel and Rhoads, 2017; Blanckaert, 2009; Blanckaert, 2010; Jamieson et al., 2010). Consequently, simplified 1-dimensional models and two-dimensional depth averaged models were proposed as the most commonly used methods for predicting flows in rivers. However, the neglect of the vertical or transverse components of the flow has yielded limitations in the flow structure determination, especially when cross-stream circulation plays a dominant role in the flow. Although some analytical models have extended the ability to predict curvature induced flow, taking into account the three-dimensional characteristics (quasi-3D models), only moderate precision can be achieved with simple flow configurations (Zeng, 2008). Furthermore, the understanding of the relevant mechanisms behind secondary circulations and capturing the complex structures of flow dynamics have put forward a higher demand for spatial resolution of measured data. The scarcity of reliable quantitative confirmations of the flow along the entire bend hampered the exploration of flow modeling in open channel bends.

There are many measurement techniques for flow field observations, and an appropriate technique should consider the required resolution, parameters, and accuracy. For example, acoustic Doppler Velocimetry (ADV) measures the instantaneous velocity components, which allows the analysis of turbulence, even small-scale flow fluctuations.

However, the drawbacks of the ADV approach are obvious; specifically, the single or multiple transmitters can only generate data with a small sampling volume; hence, it can be quite time consuming for large areas of observation. Furthermore, it can be risky to place the instrument in deep and fast flows. (MARK AND HOTCHKISS, 2007). Acoustic Doppler current profilers (ADCPs) are also commonly used in river flow measurements. It has been reported that this technique significantly improves the local bed shear stress assessment; however, data acquired near the ADCP instrument and measurements under shallow-water conditions need to be critically evaluated (MUELLER ET AL., 2007). In addition, another advanced technique in measuring velocity is particle image velocimetry (PIV) which is completely different from the point measurement methods that involve probes to receive flow velocity at a single point. In brief, the flow is seeded with tracer particles (e.g., hollow glass particles) and these particles in the flow can be illuminated with a light sheet formed by a laser beam. With a succession of laser pulses, the positions of the particles illuminated by two subsequent lasers are recorded. After post-processing, an entire region with high–resolution two- or three-dimensional instantaneous velocity fields is measured simultaneously within the illuminated plane (HOPKINS ET AL., 2000; ATKINS, 2016). There is no doubt that PIV has considerable advantages compared to other velocity measurement techniques, especially in lab measurements, and the resolution and detail can also contribute to the development of numerical modeling (WESTERWEEL ET AL., 2013).

With the improvement in computer power, computational fluid dynamics (CFD) modeling has been of significant interest in curved open channel flows in recent years. In light of the turbulence closure schemes, the predictive ability varies with different turbulence models. Data generated from a validated numerical model complements the results from the experimental observations; hence, a more comprehensive understanding of the mechanisms of open channel bends can be achieved with the combination of experimental and numerical analysis. Reynolds-Averaged Navier-Stokes (RANS) based turbulence models are the most utilized models, having a wide range of applications due to their computational efficiency and sufficient accuracy. There has been much research carried out on curved channel flows, including the analysis of water surface, mass transport, bed topography and boundary shear layer (Zeng et al., 2008; Huang et al., 2009; van Balen et al., 2010; Caldwell and Edmonds, 2014). Despite these extensive studies, it is still worth investigating the capability of the RANS models in resolving the complex 3D flow structures and the problems encountered in the prediction process.

It is widely accepted that discharging domestic and industrial effluents into rivers, estuaries, and oceans is the most common disposal method in urban areas (Colt and Tchobanoglous, 1978). Questions related to the momentum and mass transport in channel bends are crucial in the evaluation of environmental hydraulics (Ye and McCorquodale, 1998). Flow structures might vary compared to bends without jets, as the receiving water body is interrupted by the presence of effluents. Meanwhile, changes in geometrical and topographical properties can in turn also distinctly alter the mass transport. Experimental studies have shown that a bend-induced spiral motion (secondary flow) can greatly enhance the mixing potential of a meandering channel flow and can have a notable influence on the rate of longitudinal dispersion. Studies of transverse mixing behavior have confirmed that secondary flows play a considerable role in the downstream transport of pollutants (Engmann, 1986). Effluents or brine with a different density (lower or higher) compared to the receiving water body are commonly discharged as turbulent jets. Specifically, there are two major categories of outfalls according to the density of discharged solute. Effluents that have a higher density than that of the ambient water, and therefore will sink after being discharged, are called negatively buoyant jets. Although extensive experimental work has been performed on effluent-mixing in quiescent receiving water bodies, there has been little detailed information on outfall systems in the flowing ambient, especially with complex geometries such as channel bends. This may be because it is difficult to capture the interaction between the flow structure and discharge jets.

The transport and mixing processes in open channel flow involve various physical processes that can be divided into three categories: molecular diffusion, turbulent diffusion, and shear dispersion (Boxall and Guymer, 2003). Fisher (1969) was the first to explore how meandering channels and secondary motion affect mixing processes, and he concluded that it was the high turbulence intensity associated with secondary motion that increased the transverse mixing of the pollutants (Moncho-Esteve, 2017). Then, Smith (1983) recalculated the dispersion coefficient and proposed that this value could also be negative. Boxall and Guymer (2003) verified Smith's formula and suggested a new method that was capable of predicting the variation of the transverse mixing coefficient in the streamwise direction considering river meandering effects. Jeon et al. (2007) proposed a new equation to calculate the transverse dispersion coefficient, with which flow properties can be better explained in a wide range of natural streams. With the aid of computer technology, the development of secondary motion and its effects on pollutant mixing in flow meandering can also be studied three-dimensionally in more detail. van Balen et al. (2010) studied the scalar dispersion by injecting an instantaneous line source in a strongly curved open-channel bend with multiple water-depth by using both RANS models and large eddy simulation (LES) models. They concluded that the contaminants tended to accumulate at the decelerating region of the bend, and the decelerating effect increased with increasing water depth. Moncho-Esteve et al. (2017) studied the transport and mixing of pollutants in a meandering open channel with different positions of release using a LES model, and they reported that stronger and faster mixing was found with the scalar released in the center of a cross-section. Zhu et al. (2022) also investigated the mixing properties influenced by meandering; by changing the release location, they confirmed that high mixing efficiency was observed when the point source was placed at the center of the cross-section, and they noticed that higher mixing could also be found near the bend apex. In addition to the scalar mixing behavior and dispersion coefficient prediction in a bend, flow field structures influenced by the solute discharge is also challenging and requires further investigation. Therefore, it is also necessary to validate numerical models for flow structure observation and effluent mixing phenomena.

1.2 Objectives of the Study

The main objective of the current study is to investigate the variations of flow structures caused by dense jets discharged in a strongly curved open-channel bend. Another objective is to understand the mechanisms of dense effluents mixing in bend flows for improving the design of outfalls in bends. We also intend to evaluate a properly calibrated 3D numerical model which can provide better simulations of the complex 3D flow field in river bends.

In the first part, a specially designed physical model for the present study was used in the Hydraulics Lab of the Civil Engineering Department. To assess the interaction between the mixing behavior of the dense jets and the flow structures in the bend, three different density values were considered. The PIV technology was employed, to a large degree, for collecting non-intrusive high-resolution images of the flow. A flat, smooth bed (without sediment) condition has been considered to avoid further complexity. It has been noticed that a better dilution capacity can be obtained with jets discharged at the outer bank side, and it is more feasible to install horizontal outfall systems for sewage treatment plants. Therefore, the dense jets were discharged horizontally in the straight part, upstream at the outer bank side of the bend. The measuring method was verified by collecting the three-dimensional velocities at the straight part upstream of the flume. Finally, four cross-sections were selected in the present study based on the results of the dye tests while minimizing the distortion resulting from the curved bank wall and the perspective effect. The successfully collected velocity data help investigate the flow fields and design relevant experimental research.

In the second part, a quantified analysis of the vorticity equation was elaborated to understand the mechanisms underlying the influences caused by negatively buoyant jets. The existence of cross-stream circulations is known as a characteristic feature of curved open-channel flows. Given the width to depth ratio and the geometry of the bend, a two-circulation-cells pattern was expected to be detected in the current experimental results. It has been widely accepted that the driving force of the center-region cell is the centrifugal effect due to the streamline curvature, while the outer bank cell has not yet been well explained. One of the most theoretical and conceptual approaches to analyze open-channel secondary flows is using the mean vorticity equations directly (Nikora and Roy, 2012). The vorticity equation (stemming from the Navier–Stokes momentum equation) provides information about the source and dissipating terms of the flow. By considering the physical interpretation from different terms in the equation, the production and dissipation of the vorticity can be attributed to a specific mechanism. Then, a term-by-term evaluation of the vorticity equation was performed to determine the contribution of different terms that related to the specific dynamics and the role of turbulence while the density of the jets was changing. Accordingly, a more detailed picture of the interaction between the negatively buoyant jets with two-circulation-cells in an open-channel bend can be attained.

In the third part, a total of six turbulence models were trialed using the OpenFOAM platform. Three widely adopted RANS turbulence models with better performance were chosen to evaluate the accuracy and to verify the capacity of their application. Meanwhile, various boundary conditions were also tested to improve the stability and accuracy of the numerical modeling. The performances of selected models were assessed by comparing their results with velocity data collected in the bend flume using the PIV technique. To the best of the authors' knowledge, the numerical modeling of the flow structures considering the mixing behavior with a continuously scalar releasing in open-channel bends in OpenFOAM has not been previously reported. Once the models have been validated, they can provide insight into the dynamics of the flow pattern and the turbulence in open-channel bends, and it also helps provide guidance for their applications for practical use in further studies.

The current study focuses on RANS models because the models have been extensively validated, and satisfied performance can be achieved once the models are well constructed, and it is important to know the predictive capability of RANS models in bends. The experiments used for model validation only concerned the velocity, and scalar measurements were not included in the present study. According to the classification of jets in crossflow, it related to the problems in the final stage and near the far-field.

1.3 Novelty and contributions

Flow behaviors in bends have been studied in the laboratory and using CFD modeling, but few studies have been done considering three-dimensional effects with the introduction of effluents. Therefore, the major novel aspects and contributions of this study are summarized as follows:

- To the best knowledge of the author, this is the first study that involved continuously discharged horizontal crossflow negatively buoyant jets as an influencing factor to a bend flow.
- This is the first study measuring the velocity distributions of a scaler discharged continuously into an open-channel bend using the PIV technique. Several cases were studied by changing the density of effluents. Both the cross-stream velocity and turbulence stress components were measured. The experimental setup in this study is essential because the data collection of a cross-sectional plane is

instantaneous with each individual test, and no interpolation was needed in generating the velocity distribution in a cross-sectional plane. A clear acrylic bend flume ensured the requirement of a clear optical path in the application of PIV technology, and the current set-up also enables a relatively consecutive measurement in bend cross-sections.

- Finally, several numerical models were evaluated for bend flow with effluent mixing by comparing to the experimental velocity results. Different turbulence models were applied based on the OpenFOAM platform to investigate the effect of negatively buoyant jets in a channel bend. The results provide valuable information on the reliability of turbulence models for prediction of effluent mixing in meandering channel flows.

The results and findings of this study could help minimize the impacts of dense discharges on water systems when designing outfalls in engineering systems. Additionally, this study could also be taken as a reference for future studies

1.4 Thesis structure

This thesis is organized as follows:

1) Chapter 1: introduction.

2) Chapter 2: a literature review. The literature reviewed for this research focused on the experimental methods and governing equations, turbulence models, negatively buoyant jet classification, and previous models.

3) Chapter 3: a journal paper entitled "Experimental Studies on the Influence of Negatively Buoyant Jets on Flow Distribution in a 135-Degree Open Channel Bend". This paper has been published in Water.

4) Chapter 4: a journal paper entitled "Investigation of the secondary flow structures in channel bends with negatively buoyant jets". This paper has been completed and is ready to submit to journals.

5) Chapter 5: a journal paper entitled "Influence of Negatively Buoyant Jets on a Strongly Curved Open-Channel Flow Using RANS Models with Experimental Data". This paper has been published in Water.

6) Chapter 6: summary and conclusions.

Chapter 2 Literature review

Hydraulic processes of curved rivers are always of great importance due to the complicated flow configurations and their impacts on river engineering, such as river regulation, navigability, bank protection, and dispersion of heat and pollutants (Song et al., 2012). In river bends, the water surface tilts due to the centrifugal force caused by the streamline curvature. This tilting then leads to a transverse flow or secondary flow, due to which the main flow exhibits a three-dimensional helical motion. Helical flow affects the transversal slope of water surface, velocity redistribution, sediment and pollutant transport, bank erosion, channel migration. Studies of secondary flows are also useful for the analysis of mass transport processes and navigation in natural rivers (Falcon, 1984). To better understand how effluents are dispersed and their impacts on the flow structures in bends, background on the flow behaviors in bend channels and the properties of turbulent jet discharges is provided in this chapter.

2.1 Secondary flow in bend channel

2.1.1 Secondary flow velocity

It has been over a century since Thomson (1876) found that there were both longitudinal and transverse flows in bend channels. Early investigations about river bend flows were carried out through field experiments in the 1970s and 1980s (Jackson, 1975; Hey and Thorne, 1975; Bridge and Jarvis, 2010; Hickin, 1978; Dietrich, 1982), leading to a further understanding of the spatial distribution of the velocities, the maximum velocity, and secondary flows. Regarding laboratory flumes, research on the flow behavior with fixed bed and mobile bed tests, flow structures of both a single bend and consecutive bends, as well as sediment transport have raised more attention. It has been confirmed that higher velocity will at first be observed near the inside of the bend at its beginning, and then the higher velocity zone starts to shift away from the inner bank towards the outer bank to a certain degree due to the development of a secondary flow. This process continues throughout the entire bend. Hence, the higher velocity zone occurs close to the outer bank of the channel near the exit of the bend and stays for a long distance until another meander occurs, causing another change in the velocity distribution (ENGELUND AND SKOVGAARD, 1973; ENGMANN, 1986). Despite all these efforts, there is still much to investigate about flow behaviors in bends.

Flow redistribution in open-channel bends has been considered by investigating the interruption caused by the secondary flow. In the early 20th century, many researchers solved problems of flow by assuming axial symmetry of the flow field. Rozovskii (1957) analyzed the longitudinal velocity distribution and proposed an equation for the radial component of the secondary currents. However, this equation contained functions that needed to be calculated with a specific diagram, resulting in problems in quantitative analysis. Then, Engelund (1974) proposed a non-axisymmetric computational method by assuming that the velocity vector at any point on the river bottom should be consistent with the direction of the shear stress at that point. However, the value of the transverse velocity would fluctuate with the increase of Chézy coefficient. Kikkawa (1976) and Odgaard (1986) derived the secondary flow velocity equation using a linear distribution assumption of the secondary flow in the vertical direction and in the longitudinal component of the velocity vector, an exponential distribution was involved. Lately, Song et al. (2003) proposed an equation based on the Reynolds equation with a mixing length scale, and the exponential longitudinal velocity distribution was also adopted.

2.1.2 Evaluation of the secondary flow

Streamline curvature brings a lot of effects, and one of the characteristic features of open-channel flows is the existence of cross-stream circulation (Rozovskii, 1957; Engelund, 1974; Struiksma et al., 1985; Blanckaert & de Vriend, 2004). The centrifugal force varies with the water depth, and it is greater near the water surface and decreases toward the bed. It has effect on the flow when it enters the bend (Falcon, 1984), and particularly, the flow moves through a helical path in the bend, resulting in a transverse inclination of the free water surface where the water close to the surface of the river is driven outward and the water near the bottom is driven inward (Duan, 2004). In the end, the imbalance between the centrifugal force and the transverse water surface gradient force causes the water to be pushed outward and thus accumulate in the outer part of the channel. This flow pattern is termed as a secondary flow or spiral flow (Figure 2.1).

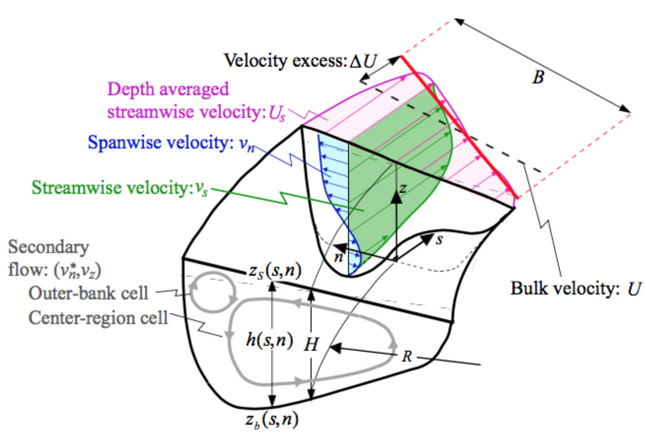

Figure 2.1 Definition sketch for curved channel flow (from Blanckaert & Vriend, 2004 and Song et al., 2012)

Researchers have tried to quantify the intensity of a secondary flow by examining the shear stress and velocity properties, as well as the secondary flow circulation, with respect to the bend geometry (KASHYAP ET AL, 2012). Other than calculating the secondary flow velocity component directedly (presented in the previous section), there were also models predicting the secondary flow by simply calculating its growth that proportionally to the relatively curvature H/R (the ratio of flow depth to centerline radius of curvature). It has also been reported that the secondary flow circulation could increase as R/B decreases (BLANCKAERT,2009). However, these simple parameterized models are only valid in mildly and moderate curved bends. The prediction can be highly inaccurate when applied in sharp bends since the nonlinear interaction between the primary and the secondary flow in sharp bends are negligible.

Most of them focused on the ratio between the average flow depth and the centerline radius of curvature H/R (curvature ratio), and they considered this ratio as a predominant parameter for evaluating the behavior of the secondary circulation in the bend (ROZOVSKII,1957; BATHURST ET AL., 1977, ENGELUND, 1974; ZIMMERMAN, 1978; FROTHINGHAM AND RHOADS, 2003; NANSON ET AL., 2010). Rozovskii concluded that the strength of the secondary flow had a linear relationship with the curvature ratio (ROZOVSKII, 1957; DE VRIEND, 1977; JOHANNESSON AND PARKER, 1989A), and Hickin (1978) found that the magnitude of the secondary flow increased rapidly as the ratio of the curvature radius of bend (R/B) declines from 4 to a minimum value of 1.41. However, this linear approach was proved to have the restriction that it was only valid in mildly curved channels (BLANCKAERT, 2009), as the normalized magnitude growth of the secondary flow induced by the curvature ratio was found to be limited in strongly curved channels (WEI ET AL., 2016). Therefore, more parameters such as R/B (where B is the width of the channel), B/H (aspect ratio), and the dimensionless Chézy friction coefficient C_f (C_f dimensionless roughness coefficient) need to be considered when interpreting the behavior of a secondary flow. More recently, research on the parameterization for the secondary flow has emphasized the nonlinear interaction between the primary and secondary flow, and the effects of R/B and C_f^{-1}H/B on the flow in bends have been thoroughly investigated in order to fit the entire range of curved channels (i.e., mild, moderate, and sharp bends) (BLANCKAERT AND DE VRIEND, 2003, 2010; OTTEVANGER ET AL., 2011,2012; KASHYAP ET AL, 2012; WEI ET AL, 2016).

Table 2.1 Experimental parameters of bend from typical lab flumes

Researcher	Year	Number of Bend	Degree	*B (m)*	*H (m)*	*R (m)*	*L (m)*	*Fr*
Shukry	1950	1	180	0.300	0.290	0.300	1.070	0.461
Rozovskii	1957	1	180	0.800	0.058	0.800	3.000	0.340
Yen	1965	2	90	1.830	0.150	8.540	4.260	0.580
Fischer	1969	2	90	0.763	0.022-0.052	2.060	-	-
Chang	1971	2	90	2.340	0.115	8.530	4.270	0.325
Fukuoka	1971	13	90	0.254	0.057	0.914	0.476	0.473
Fukuoka	1971	13	90	0.254	0.054	0.914	0.476	0.275
De Veriend	1979	1	180	1.700	0.200	0.425	6.000	0.400
Seibert	1982	2	180	0.250	0.200	1.000	0.500	0.230
Steffler	1984	1	270	1.070	0.061	3.660	2.400	0.491
					0.085	3.660	2.400	0.460
Ervine	1993	2	120	0.900	0.050 - 0.300	2.740	-	-
			110	0.900	0.050 - 0.300	2.740	0.937	-
Booij	1996	1	180	0.500	0.052	4.100	6.700	0.280
Muto	1997	9	60	0.150	0.052	0.425	0.376	0.431

		9	120	0.150	0.051	0.425	0.376	0.359
		11	180	0.150	0.053	0.425	0.000	0.307
K.Sudo et al	1998	1	90	0.104	-	0.208	4.160	-
Ghanmi	1999	2	90	0.500	0.150	1.500	3.500	0.247
Loveless	2000	4	60	1.600	0.150	1.334	-	-
K.Sudo et al	2000	1	180	0.104	-	0.208	4.160	-
K.Sudo et al	2001	1	90	0.080	-	0.160	3.200	-
Blanckaert	2002	1	193	1.300	0.108	1.700	5.000	0.390
					0.159	1.700	5.000	0.350
					0.212	1.700	5.000	0.260
					0.141	1.700	5.000	0.410
Wang	2008	6	180	0.400	0.050	1.000	0.000	0.047
He	2009	2	180	0.400	0.100	1.000	0.000	0.327
Abhari	2010	1	90	0.600	0.200	1.800	5.652	-
Jamieson et al.	2010	1	135	1				
Han	2011	1	90	0.610	0.091	0.455	2.400	0.252
Ottevanger	2012	5	180	0.600	0.143	1.440	-	-
Kashyap et al.	2012	1	135	1.000	0.150 - 0.200	1.500	-	-
Wei et al	2016	1	193	1.000	0.085 - 0.257	1.700	9.000	0.1, 0.23, 0.32, 0.4, 0.5
Bai et al	2018	1	180	1.5	0.06			
Schreiner et al.	2018	1	135	1				

Moreover, in addition to modifying the velocity profile, the momentum transport equation can also be investigated with term-by-term evaluations to reveal the mechanisms underlying the streamline curvature (Blanckaert and de Vriend, 2004). Related work has then been done referring to the velocity redistribution, bed topography, bed shear stress redistribution and migration pattern (Blanckaert, 2010; Termini, 2015; Farhadi, 2018; ESFAHANI, 2020). Besides, the key terms in the kinetic energy equation and the enstrophy equation were also analyzed for understanding of the process of the energy transformation and the resistance in meandering rivers (HU ET AL., 2019).

Studies on flow configurations in bends have attracted wide attention since the 1870s, and a large amount of experimental research has been done with different bend parameters (Table 2.1).

2.1.3 The outer bank cell

Apart from the classic helical motion, also known as the main vortex, another type of cross-stream current occurs at the outer bank of a bend, which is known as the outer bank vortex (Figure 2.1). Instead of covering most of the center region in a cross-sectional plane, the outer bank vortex is relatively weak and is found close to the outer boundary. The previous observations of the outer bank cell were considered as robust since the river under investigation had a small aspect ratio and with high flow rate (RUSSELL AND VENNELL, 2019). De Vriend (1981) concluded that the outer-bank cell suddenly appeared at higher values of the turbulent Dean number (similar to the curved laminar flow) or high curvature in the curved channel with a rectangular cross-section. Thorne (1985) associated bank erosion with the complex secondary current in bend flows, which was also accepted by a large number of researchers. However, Blanckaert and Graf (2001, 2004) conducted an experimental analysis in a strongly curved channel, and they proved that the outer bank cell keeps the high-momentum fluid away from the near-bank region. Then, Blanckaert and Vriend (2004) investigated the underlying dynamics using the vorticity equation and the kinetic energy transfer and suggested that the outer bank cell arises from the combining effect of flow instability or turbulence anisotropy and the centrifugal force. Despite all this, quantitative illustration about the impact parameters on outer bank cells is still a problem due to lack of fine-resolution experimental data.

de Vriend (1981) attempted to simulate the secondary currents using a depth-averaged eddy viscosity, but he failed in resolving the outer bank cell. Christensen et al. (1999) conducted an RSM simulation with a linear k-ϵ closure, and they successfully reproduced the outer bank cell. van Balen et al. (2009,2010) compared LES models with RANS models and concluded that the outer bank cell could only be captured by LES models. Xiao et al. (2017) evaluated the 3D RANS models with experimental and field data, and reasonable accuracy was obtained with RANS models in simulating flow fields in curved open channels.

2.1.4 Numerical studies of bend channel

The rapid development of computers has brought a series of mathematical models for hydraulic engineering, and investigations into problems involving velocity distribution, shear stress states, water quality evaluation, and sediment transport have become feasible by means of numerical simulations. Numerical modeling provides more information compared to experimental work and can also significantly reduce the cost. Therefore, the use of numerical simulations has significantly increased in the past few decades.

For a long time, one-dimensional (1D) models were used prevalent in practical hydraulic applications (BRUNNER, 2006; HUANG AND GREIMANN, 2007), especially when analyzing long river reaches (Lai, 2010), while two-dimensional (2D) models are capable of simulating certain flow features that one-dimensional models cannot, and the velocity properties and behavior of the water surface in bends can be obtained with acceptable accuracy. However, multidimensional modelling is obviously more precise, since flows in channel bends are three-dimensional in nature.

Leschziner and Rodi (1979) first introduced the use of the finite-volume method to solve problems in strongly curved channels. However, the influences of flow separation and hydraulic jumps were ignored in order to save on computational expense. Leschziner and Rodi (1979) solved transport equations for turbulence kinetic energy k and its dissipation rate ϵ, and then, with the refined k-ε turbulence model, they predicted transverse surface slopes and secondary velocity fields. Demuren and Rodi (1986) investigated longitudinal and vertical velocity fields and developed a 3D mathematical model to obtain the secondary flow and mass transport properties in a channel bend. They validated the model with the velocity and concentration data, and they later extended the model to fit channels with width-to-depth ratios ranging from 4 to 20 for smooth and rough beds.

Three-dimensional (3D) numerical approaches have enabled more accurate numerical predictions, especially when the interactions of flow structures needed to be considered, and they definitely provide more details of flow structures (Duan, 2004). Cheng and Farokhi (1992) proposed a model that incorporated new algebraic formulations for eddy viscosity with the standard k-ε turbulence model to consider the effects of streamline curvature, while Ye and McCorquodale (1998) also brought in a refined k-ε model that included the anisotropic influence caused by streamline curvature, free surface, and solid walls. Later, Booij (2003) executed large eddy simulations (LESs) to inspect the flow behavior in a rotating annular flume and concluded that the LES model had better performance for estimating the main flow, secondary flow, and turbulence energy than the RANS models. Lu et al (2004) modified the k-ε model with an improved SIMPLEC (velocity-pressure-free-surface coupled correction) algorithm, and by applying the model on a 180-degree bend, it was found that the model could well predict the flow velocity, behavior of the secondary flow, distribution of bed shear, and variation of flow depth in both the span-wise and longitudinal directions (Lu et al, 2004). More recently, Stoesser et al. (2010) compared the numerical results generated from the RANS and LES methods, and good agreement was observed through the comparison, i.e., both approaches could predict the outer bank cell in addition to the primary helical flow. However, the RANS method overpredicted the size and strength of the outer-bank cell, while LES could estimate it well in the area from the bend apex to the bend exit. Gholami et al. (2014) validated a numerical model with experimental results for a strongly curved 90° bend and concluded that the VOF methods (*k-ε RNG)*) are able to predict both the velocity field in a channel as well as the free surface of the water.

Studies on the experimental research of flow configurations in bends has been done with different turbulence models and different geometry (Table 2.2).

Table 2.2 Non-exhaustive list of numerical simulations of open-channel bend flows

Experimental Data	Year of lab test	Author	Year of Simulation	Turbulence Model	Results
Shukry	1950	Feng et al	2008	k-ε/k-ε RNG/RSM	water surface, velocity
		Li et al	2009	realizable k-ε	water surface, velocity
		Tan et al	2012	k- ω	water surface, velocity,streamline
Rozovskii	1957	Meselhe et al	2000	k-ε	velocity
		Duan	2004	zero equation	water elevation, flow structure
		Nguyen	2007	k-ε	water surface, velocity
		Zhou	2009	zero equation	water surface, velocity, secondary flow
Yen	1965	Meselhe et al	2000	k-ε	secondary flow, wall shear stress
		Huang	2001	k-ω	water surface, velocity, wall shear stress
		Xiao	2013	zero equation	velocity
Chang	1971	Demuren et al	1986	k-ε	velocity, salinity, bed shear stress
		Ye	1998	k-ε	water surface, velocity, salinity
		Duan	2004	zero equation	velocity, salinity
		Huang	2006	k-ε	water surface, velocity, secondary flow
		Hu	2009	k-ε	velocity
		Li	2012	-	water surface, velocity, salinity
Fukuoka	1971	Demuren et al	1986	k-ε	velocity
de Veriend	1979	Ye	1997	k-ε	water surface, velocity
		Duan	2004	zero equation	water elevation, flow structure
Siebert	1982	Stoeseer	2010	k-ε/k-w/LES	main flow, secondary flow, wall stress
Steffler	1984	Zhou	2009	zero equation	water surface, velocity, secondary flow
Ervine	1993	Morvan	2002	k-ε	velocity

Booij	1996	Booij	2004	k-ε/LES	water surface, velocity, secondary flow
		Van Balen et al	2009	LES	water surface, velocity, turbulence
Muto	1997	Moncho Esteve et al	2010	LES	water surface, velocity, secondary flow, turbulence magnitude
Ghanmi	1999	Ghanmi	1999	zero equation	velocity
Loveless	2000	Wormleaton et al	2006	k-ε	water surface, velocity, secondary flow
Blanckaert	2002	van Balen et al	2010	k-ε/LES	velocity, bed shear stress
		Constantiniescu et al	2011	SA Model	water surface, velocity, turbulence momentum, wall shear stress
Lu	2004	Lu	2004	k-ε	velocity, secondary motion, bed shear, flow depth
Matsuura	2004	Khosronejad et al.	2007	k-ω/ k-ε	three velocity components, bed topography
Wang	2008	Li et al	2009	realizable k-ε	vertical velocity in transverse section, longitudinal surface velocity
		Zhou	2009	zero equation	velocity
Han	2011	Han et al	2011	RSM	water surface, velocity, bed shear stress
		Ramamurthy et al	2013	k-ε /RSM/ LES	velocity
Kashyap et al.	2012	Kashyap et al.	2012	*k-ε /k-w/ RSM*	velocity, bed shear stress, vorticity
Constantinescu et al.	2013	Constantinescu et al.	2013	LES	Velocity, shear stress, vorticity

2.2 Effluent distribution

Buoyant jets can be divided into two categories by comparing the density between the jets and the ambient receiving fluid, while effluents with a higher density than that of the ambient receiving environment are called negatively buoyant jets. The mixing behaviors of these jets have drawn a lot of attention both in engineering and overall scientific research, and during the last 50 years, increasing numbers of numerical and experimental studies have been done on this subject in order to better interpret the relevant mixing processes. In this section, existing numerical and experimental works on negatively buoyant jets are summarized.

2.2.1 Flow classification of buoyant jets

Reichardt (1942) used Gaussian profiles as a first-order solver to approximate the velocity and scalar distribution in jets' cross-sectional planes, and this is considered to be a rudiment of the integral theory (JIRKA, 2004). Later, a new concept called the jet entrainment theory was brought into the field of jet-mixing analysis. Morton (1956) was the first to apply Taylor's (1945) "jet entrainment hypothesis" in predicting jet-spreading behaviors, and he also proposed a model for buoyant jets. According to Morton and Taylor's theory, a downstream ambient fluid tends to enter a turbulent jet's zone through the jet edge with a periphery of $2\pi B$, where the velocity of the entrained fluid is proportional to the mean jet centerline velocity (JIRKA, 1982). The fluid entrainment theory has brought many advances in the development of integral buoyant jet models for flow structure detection, with more complex jet properties and ambient conditions (JIRKA, 2004). A well summarized review of an integral model was produced by Jirka (2004), including its development and advantages, mechanics and principles in using length-scale analysis, and formulation and evaluation of the latest adaptation. In the following, the framework and procedures for buoyant jet classification will be introduced.

The schematic conditions for submerged buoyant jets are shown in Figure 2.2, and variables with the subscripts u_a and u_0 represent ambient water and buoyant jets respectively, and as depicted in this figure, the width and depth of the ambient water are W and H respectively. The fluid velocity is U, and ρ is fluid density. The effluent discharge angle is denoted by θ and σ (measured counterclockwise to the streamwise direction), which correspondingly indicate the vertical and horizontal orientations of the diffuser. Specifically, a strict crossflowing discharge condition can be defined with θ being equal to 0 and α being 90 degrees. The distance between the nozzle and the nearest bank is Y_N, and the height above the bottom is h_0. The nozzle diameter is D_j, generating a jet initial cross-sectional area (a_0) equal to $\pi D^2/4$.

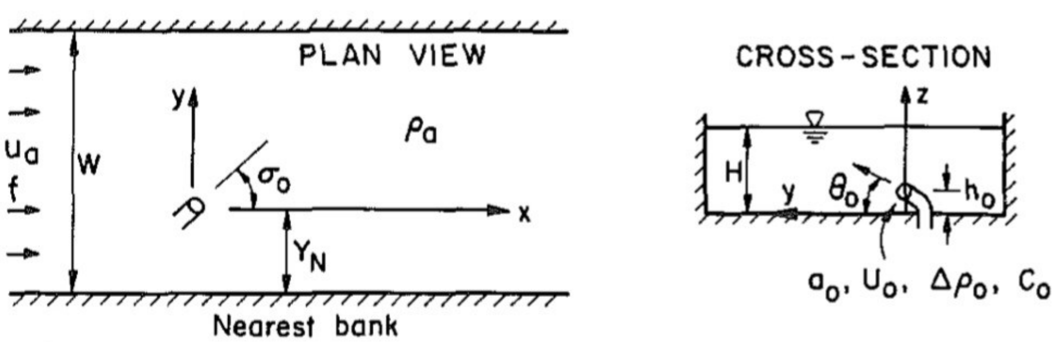

(a) (b)

Figure 2.2 Geometry of submerged buoyant jet (FROM JIRKA AND DONEKER, 1991)

The classification is based on the different length scales of the submerged buoyant jets. The length scales are derived from the hydraulic parameters of the jets, i.e., the kinematic momentum flux M_0,

$$Q_0 = U_0 a_0, \qquad M_0 = Q_0 U_0, \qquad J_0 = Q_0 g_0' \tag{2.1}$$

$$g_0' = \left(\frac{\rho_a - \rho_0}{\rho_a}\right) g \tag{2.2}$$

where g is gravitational acceleration.

The five length scales used to define the jets stages are written as follows (Jirka and Doneker, 1991):

$$L_Q = Q_0 / M_0^{1/2} = a_0^{1/2} = \text{discharge length scale}$$

$$L_M = M_0^{3/4} / J_0^{1/2} = \text{jet/plume transition length scale}$$

$$L_m = M_0^{1/2} / U_a = \text{jet/crossflow length scale}$$

$$L_b = J_0 / U_a^3 = \text{plume/crossflow length scale}$$

$$L_T = M_0^{2/3} / (J_0 U_a)^{1/3} = \text{puff/thermal transition length scale}$$

L_Q is the scale that depends on the nozzle size, and it usually has an effect on the zone of flow establishment. Jet behavior in the flow establishment zone is highly related to the initial condition of the momentum and discharge rate, and ambient fluid in this zone has a minimal influence on the jets. L_M is a measure indicating the transition zone where the effluent transitions from a jet to a plume. The motions arising from the initial conditions play a gradually smaller role in the spread of the jet, and afterwards, the buoyancy governs the mixing and subsequent lateral spreading. L_m measures the length beyond which the discharge momentum loses dominance, and the crossflow takes over, causing the jet to deflect. L_b is the start point of the pure plume region, where the jet is strongly advected with the crossflow. L_T is the length of the far field transition phase, where it can readily be affected by the strong advection in the ambient water (JIRKA AND DONEKER, 1991). Figure 2.3 provides images from the literature describing jet zone classifications at various scales.

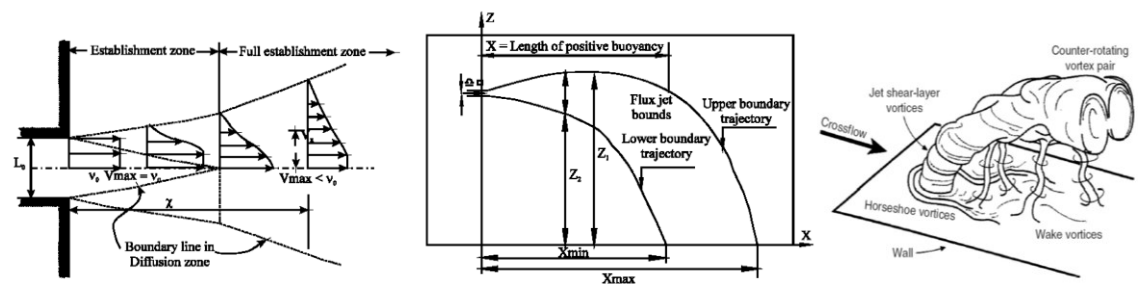

(a) (b) (c)

Figure 2.3 (a) Schematic demonstration of jets diffusion(ALBERSTON, 1950) and (b) trajectory boundaries of a jet (AHADIYAN AND MUSAVI-JAHROMI,2009) (c) Sketch of vortex systems of jet in cross-flow (JICF) (FRIC AND ROSHKO, 1994).

According to the non-dimensional processing, some interrelationship can be found between the source Froude number F0 and the crossflow parameter R_{cf}.

$$F_0 = \frac{U_0}{\sqrt{g_0' \, a_0^{1/2}}} = \frac{L_M}{L_Q} \tag{2.3}$$

$$R_{cf} = \frac{U_0}{U_a} = \frac{L_m}{L_Q} \tag{2.4}$$

Jirka and Doneker (1991) proposed a classification scheme for negatively buoyant jets discharging into both homogenous and stratified ambient fluid. Comparison and validation of the classification covered plenty of experimental data (JORDINSON, 1956; KEFFER AND BAINES,1963; SCORER,1959). The instruction was elucidated as a flowchart shown in Figure2.4. Detailed information can be obtained in the following papers (JIRKA AND DONEKER; 1991 AND 2004).

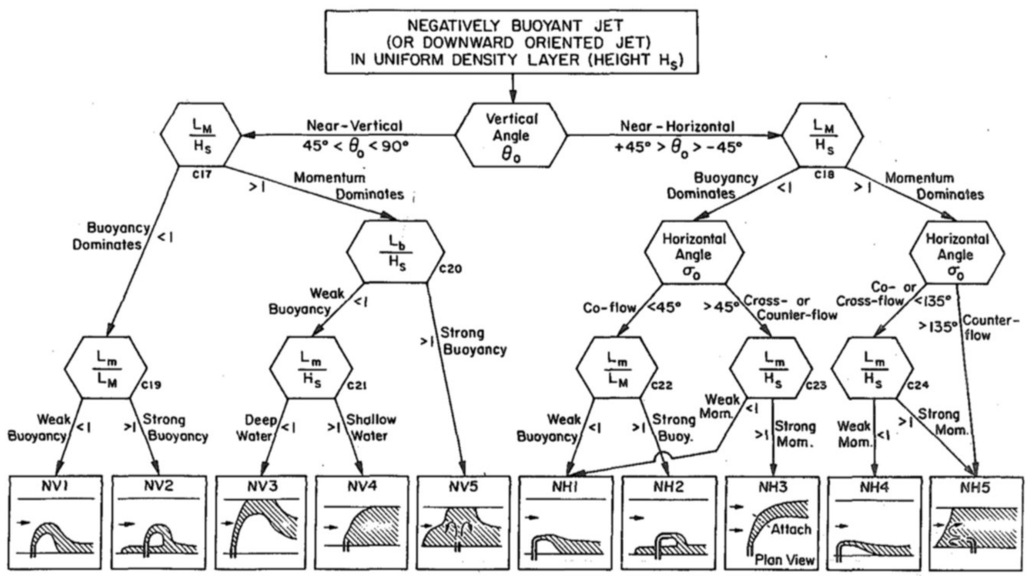

Figure 2.4 The classification scheme for submerged negatively buoyant discharge in uniform ambient water layer (JIRKA AND DONEKER, 1991).

2.2.2 Experimental studies

Negatively buoyant turbulent jets have been well studied experimentally over the past few decades. In early works, old-fashioned pitot tubes were widely used in measuring mean flow velocity. To obtain higher quality data in more recent years, however, techniques such as acoustic Doppler velocimetry (ADV), particle tracer method, hot-wire anemometry, and so forth have been introduced for hydraulic tests in order to obtain 3D measurements for both velocity and concentration. Lately, studies of buoyant jets have experienced tremendous improvements through innovations and experimental technologies. For instance, methods for experimental measurements have been enhanced by applying laser technology to hydraulic experiments. One method that has proved to be accurate and convenient for obtaining experimental data is laser scanning. At first, the Laser-Doppler Anemometry (LDA) method was used due to its advantages in measuring instantaneous velocity, and after that, Particle Tracking Velocimetry (PTV) and Particle Image Velocimetry (PIV) were highly recommended for velocity distribution measurements. Then, laser-based methods called Light Attenuation (LA) and Laser Induced Fluorescence (LIF) showed obvious superiority in measuring fluid concentrations. These methods provide a way to extract reliable data in a specific field of interest with fewer errors.

Zeitoun et al. (1970) fist conducted a series of experiments investigating how discharge angles influence jet behaviors, and trajectories and dilution rates were measured using a point-based conductivity meter. They suggested that among all the tested angles, the longest trajectory was achieved with the negatively buoyant jets discharged at 60-degree to the horizontal. Roberts and Toms (1987) later conducted experiments with dense jets inclined at 60 degrees and compared the results with those for vertical dense jet. In a paper published in 1972, Pincince and List carried out experiments on brine disposed into a flowing stream; they compared their experimental data with the results from their integral model and concluded that the model was able to predict the jet trajectories with reasonable accuracy, although the dilution was significantly underestimated. Roberts et al. (1997) used a combination of laser-induced fluorescence (LIF) and micro-conductivity probes to obtain data measurements close to the boundary for a single-port diffuser inclined at 60 degrees, and they found that at the lower boundary, the lowest dilution which was termed as the impact point was found at the centerline.

Later, Cipolina et al. (2005) studied mixing trajectories with four parameters, namely, the nozzle diameter and inclination, and jet density and flow rate. By including a wide range of densimetric Froude numbers (from 30 to 120), for various discharge angles, i.e., 30°, 45°, and 60°, they concluded that correlation between the densimetric Froude number and the discharge angle could easily be established once the parameters were normalized by the nozzle geometry, however, no dilution data were obtained. Kikkert et al. (2007a, 2007b) subsequently reported concentration measurements for jets with angles of 15°, 30°, 45°, and 60° in stagnant water using both light attenuation (LA) and LIF technologies and got good results to predict the jet flow path and the trajectory using an analytical method. Bashitialshaaer et al. (2013) performed an investigation on the behavior of inclined negatively buoyant jets by changing four parameters of the jets, including, nozzle diameter, inclination angle, jet density and flow rate. With a dimensionless analysis, Bashitialshaaer et al. (2013) concluded that jet geometry can be related to the densiometric Froude number, and they concluded that with predicted vertical and horizontal distance to the maximum centerline level, one can derive other geometric quantities from the same regression relationships. Jiang et al. (2014) conducted experiments in shallow water condition of inclined dense jets and identified three different mixing regimes. They found there were various linear coefficients in transitional regime and confirmed that the water surface constrained jet mixing behavior.

2.2.3 Mixing of effluents in bend

Bends induced secondary currents alters the mixing behavior in both the longitudinal and transverse directions (FISCHER, 1969). Earlier works about the dilution mixing defined the dispersion coefficients in different directions in terms of the infinitely long and uniform geometry streams (TAYLOR, 1953; ARIS, 1956). Fischer extended Taylor's concept to infinitely long uniform meandering streams both in continuously one direction (one bend) (FISCHER,1968) and alternate directions (consequent bends) according to the flow velocity components (FISCHER, 1969), which gave an analytical approach for the mixing behavior of a bend. He also found that the change of bend directions was noticed to affect the dispersion only in wider streams. However, the results of the averaged concentration at each cross section from Fischer were justified to be applied where the cross-stream mixing was not important and only limited accuracy were shown. Smith (1983) considered the longitudinal contaminant dispersion in varying flows, including the change of the width of channel, length of bends, water depth, and the curvature properties. To a certain extent, Smith's works consolidated the concept of Fischer (1969), but Smith's equations and validations were derived based on a depth-averaged assumption, with which the vertical dispersion of the scalar was considered well mixed.

At that time, the evaluations of the mixing of pollutants in meandering streams were carried out analytically and empirically and with one- or two-dimensional treatment assumptions for the dispersion by involving the velocity profile in the calculations. However, the complex three-dimensional properties of the flow in curved channels require three-dimensional considerations for the effect of the secondary flow on the flow field, variation of the shear stress, and the actual mixing process of mass and pollutant analysis. Therefore, mathematical models that accounts for the three-dimensional nature of curved channels with less restrictions seem more reliable.

Demuren and Rodi (1986) calculated pollutant dispersion in meandering channels with a with a k-ε turbulence model that considered the streamline curvature effects. By trying with a large range of the width-to-depth ratios, they concluded that the effect of streamline curvature would dominate the behavior of turbulent mass flux mixing only in case of narrow channel with smooth bed and more than one eddy was found in the flow. Ye and McCorquodale (1997) also applied a three-dimensional k-ε turbulence model to investigate the mass transport in a bend flow, including the variation of the free surface and bathymetry, and they indicated that secondary flow in curved channels played an important role in the mass mixing. Later, van Balen et al. (2010) demonstrated the scalar dispersion of a line sour and a line source in a strongly curved channel by comparing the performance between a LES model and a RANS model. They found that the gradient-diffusion hypothesis (the concentration was calculated by using the eddy diffusion coefficients in the corresponding direction). More recently, Pilechi et al (2016) proposed a numerical estimation approach to predict the transverse mixing coefficient in bend flows, and they found that the prediction agreed well with both experimental results and empirical analytical conclusions. However, due to the shallow condition of flow, the vertical mixing was defined as well developed beyond the initial zone, therefore, they used a 2D model to calculate the contaminant mixing. Schreiner et al. (2018) developed an approach to determine the jet trajectory by taking account of the presence of the curvature induced secondary flow as well as the formula for the trajectory in straight channels with crossflows. However, the proposed formula cannot provide the contaminant concentration in the bend.

Mixing in river is crucial to investigate in channel bends due to its importance on urban life and environmental resources preservation. Extensive studies have been done on curved channel flows. However, attention that has been paid to the scalar dispersion in curved open channels is insufficient, especially considering the three-dimensional features of bend flows. Besides, from a practical point of view, it is better to substitute the non-buoyant sources in the previous studies with buoyant sources for more accurate predictions of the scalar spreading behavior in channel bends. Therefore, further research is required as references for this topic.

2.2.4 Simplified numerical models

With the aid of computer simulations, it is easier to provide valuable insights into the formation of flow structures and the prediction of dilution, although moderate precision can be obtained with experimental data analysis. As well, from a practical viewpoint, numerical simulations can evaluate more complex flow conditions, while simplifications and assumptions are always required with reduced scales when implementing experiments. However, experimental data that are collected from the flow with real turbulent structures can be used to calibrate and enhance the abilities of numerical models.

In the previous section, the flow classification method based on the fluid entrainment theory was briefly introduced. Jets behaviors can be classified through their cross-section data profiles, considering various source and ambient conditions (JIRKA, 2004). To be more specific, five regimes, i.e., pure jet, pure plume, pure wake, advected line puff, and advected line thermal, with variable ambient conditions, are treated separately in order to better evaluate and predict the turbulent buoyant flux. Many integral models have been proposed for the analysis of jet-mixing, including CORMIX, VISUAL PLUMES, VISJET, and so on (PALOMAR ET AL, 2012). The most widely used CORMIX model consists of three components, namely CORMIXl (DONEKER AND JIRKA 1990), CORMIX2 (AKAR AND JIRKA 1990), and CORMIX3 (JONES AND JIRKA 1991), which solve problems regarding submerged outfalls, various diffusers, and surface outfalls respectively (GAWAD ET AL, 1996). For more information with respect to details of the integral models' formulations, please see Jirka (2004).

2.2.5 Numerical studies using CFD

By means of the above mentioned simplified numerical integral methods, details of the development in the diffusion process are missing, especially, reproducing the turbulent structures is the primary difficulty. To achieve better accuracy with a wide range of jet types, computational fluid dynamics (CFD) modeling makes a compensation in improving the certainty of jet spreading predictions. The main idea of CFD is to solve governing equations by means of computational techniques, leading to a series of numerical models that are approximations of the true solutions of the Navier Stokes (NS) equations (ALFONSI, 2009). In most cases, getting the information of the mean flow is more important than grasping every detail of instantaneous fluctuations. Given this matter, Reynolds decomposition was introduced to subtract those fluctuations and average the NS equations, which laid a foundation of Reynolds averaged Navier Stokes (RANS) models. To facilitate the averaging, various quantities such as the velocity components are decomposed into two parts, a time-averaged part and a fluctuation part. Boussinesq (Boussinesq, 1877) was the first to propose a closure of the NS equations by bringing in a concept of eddy viscosity. Later, Prandtl (1925) interpreted the eddy viscosity by introducing an approach called the mixing length, which was the first successful attempt to the NS equation closure problem. However, these eddy viscosity-based models have their limitations in properly interpreting some complex flow structures and specific action of the Reynolds stress tensor (Alfonsi, 2009). Second-order closure schemes, on the other hand, directly calculate the Reynolds stresses. However, it is quite time consuming to solve six additional transport equations of Reynolds stress components, especially when the Reynolds number is high. Despite both the linear viscosity and nonlinear viscosity RANS models have been widely used for decades, researchers are still keen to solve problems with more complex flow structures.

In the meantime, large eddy simulation (LES) was proposed in order to resolve the anisotropic eddy viscosity properties of the flow. With a length filter, small turbulent structures are resolved separately by time and spatial averaging in a small-scale sub-grid model, while time-resolved large eddies are directly calculated to represent the features of turbulent flow (Yang, 2014). Many of the recent LES based numerical studies consider jets in crossflow are mostly vertical jets, such as Yuan et al. (1999), Sheet & Ferziger (1999), Schluter and Schonfeld (2000), Salewski et al. (2008), Ziefle and Kleiser (2009), Cavar and Meyer (2010), and Ivanova et al. (2011 and 2013).

Besides those turbulence models, direct numerical simulation (DNS) solves the NS equations directly, in other words, no turbulence model is used in the calculation. At first, DNS attempts only considered cases with Reynolds number as low as 35. Then, with the studies done by Rogallo and Moin (1984), the first DNS for practical interpretation of homogenous turbulence was obtained. Subsequently, DNS has been applied more widely due to the advanced computing techniques. Hence, it is certain that DNS leads to very high computational cost, but it offers accurate results. DNS studies dealing with jet in crossflow have been conducted, e.g. Rudman (1996), Sau (2004), Muppidi and Mahesh (2005).

Research about horizontal jets is relatively scanty compared to vertical jets or incline jets. El-Amin et al (2010) used realizable k-ε model to analyze buoyant horizontal jets by changing the temperature and Reynolds numbers of the jets. They observed stratification phenomena in their experimental and numerical results and made a conclusion that horizontal jets have their particular features in the transitional part, such as bifurcation and stratification. Later, Ghaisas et al. (2015) performed large eddy simulations on turbulent buoyant horizontal jets, and it had been found that the Richardson numbers and the Reynolds number influenced the deflection of jets and the jet symmetry respectively. Gao et al (2017) considered different densimetric Froude number and jet-to-current velocity ratio by applying the renormalization group (RNG) k-ε model on buoyant horizontal jets in a counterflow, and they proposed a relationship between the distance to the nozzle and the centerline dilution. Chen and Hsiao (2018) showed that the jet behavior in the presence of surfaces waves is affected by the parameters such as water depth, wave height over wave depth and buoyancy, and simulated the near field jet trajectory and diffusion using the standard k-ε model.

From an overall viewpoint, research on negatively buoyant jets in a bend flow is very scarce both in experimental and numerical works. Existing studies related to this topic, taking the mixing of the JICR as an example, focus more on the starting part of the vortex structure but neglect the far field effect caused by the main flow. Although research on scalar dispersion and mass transport in open channels has been performed for a long time, the tracer sources of the dispersion terms barely have continuous interaction with the main flow. Moreover, due to the significant complexity in the problems discussed above, flow structures are fully three-dimensional. Methods and models that are three-dimensional should be more suitable. Therefore, the large eddy simulation and the PIV technology, which are considered as more advanced analysis approaches, were employed in the present study for negative jets in crossflow with various densities in a channel bend.

2.3 Theoretical background of numerical simulations

Due to the high cost of time and techniques for experimental data, it is difficult to measure the entire flow field. Validated numerical models can be alternatives for interpreting flow behavior. With computational simulations, it is feasible to accurately examine any specific location in the entire field and to extract the features of the flow. The background of computational fluid dynamics and its methodology will be introduced. Turbulence models as well as the software that is used in this research will also be elaborated upon.

2.3.1 Governing equations in CFD

Navier-Stokes equations for Newtonian incompressible fluids describe the governing equations for fluid motion mainly based on Newton's second law. The momentum conservation equation in Einsteinian notation is described as

$$\rho\frac{\partial u_i}{\partial t}+\rho\frac{\partial\left(u_j u_i\right)}{\partial x_j}=\frac{\partial\tau_{ij}}{\partial x_j}-\frac{\partial p}{\partial x_i}+\rho g_i \tag{2.5}$$

where u_i is velocity, p is the pressure, ρ is the fluid density, t is time, g is gravitational acceleration and x_i is the coordinates in Cartesian frame.

The viscous stress is considered as:

$$\tau_{ij}=\mu\left(\frac{\partial u_i}{\partial x_j}+\frac{\partial u_j}{\partial x_i}\right) \tag{2.6}$$

Where, μ is the molecular viscosity.

The continuity equation based on the conservation of the mass leads to:

$$\frac{\partial u_i}{\partial x_i}=0 \tag{2.7}$$

The advection-diffusion equation for a scalar parameter is considered as

$$\frac{\partial(\phi)}{\partial t}+\frac{\partial(u_i\phi)}{\partial x_i}=D\frac{\partial^2\phi}{\partial x_i^2} \tag{2.8}$$

Where, ϕ is the scalar concentration and D is isotropic diffusion coefficient.

The Navier-Stokes equations can be solved only numerically. Even then, unless DNS is performed, the equations are first simplified by time and/or spatial averaging. The approaches that are used to find the solutions for the simplified equations are called turbulence closure schemes. Different methods with relevant assumptions have been proposed to obtain the approximate value, which then would be summarized as a turbulence model. Generally, there are two categories of turbulence models. The most important branch includes models that utilize the Boussinesq hypothesis. In 1877, Boussinesq postulated that the momentum transfer caused by turbulent eddies can be modeled using eddy viscosity. The Boussinesq assumption states that the Reynolds stress terms are proportional to the traceless mean strain rate tensor.

2.3.2 Turbulence models

In order to achieve closure of the governing equations, it is assumed that every variable has two components: the average part (time averaged) and the oscillatory part. Take velocity as an example; the flow velocity should be the superposition of mean velocity with its fluctuation part:

$$u(x,t) = \bar{u}(x) + u'(x,t) \ \text{ or, more simply, } u = U + u' \tag{2.7}$$

where the average can be defined as

$$\bar{u}(x) = \lim_{T\to\infty} \frac{1}{T} \int u(x,t)dt \tag{2.8}$$

$$\bar{\phi}(x) = \lim_{T\to\infty} \frac{1}{T} \int \phi(x,t)dt \tag{2.9}$$

The Navier-Stokes equations can be written after averaging as

$$\rho \frac{\partial \bar{u}_i}{\partial t} + \rho \bar{u}_j \frac{\partial \bar{u}_i}{\partial x_j} = -\frac{\partial p}{\partial x_i} + \frac{\partial}{\partial x_j}\left[\mu\left(\frac{\partial \bar{u}_i}{\partial x_j} + \frac{\partial \bar{u}_j}{\partial x_i}\right) - \rho \overline{u_i' u_j'}\right] + \rho g_i \tag{2.10}$$

$$\tau_{ij}^R = -\overline{u_i' u_j'} \tag{2.11}$$

The term τ_{ij} is called Reynolds stress, which represents the transfer of fluid momentum due to turbulent fluctuations. In order to obtain the value of this term, various approaches are used. In this study, two turbulence models that are used in our research will be introduced.

(1) $\boldsymbol{k - \epsilon}$ Model

The $k - \epsilon$ model is one of the most popular two-equation eddy viscosity turbulence models. This model is based on transport equations for turbulent kinetic energy (k) and dissipation rate (ϵ) (LAUNDER AND SPALDING 1974). Here, a brief description of this model is presented. The transport equation for k is written as:

$$\frac{\partial k}{\partial t} + \bar{u}_i \frac{\partial k}{\partial x_i} = \nu_t \left[\frac{\partial \bar{u}_j}{\partial x_i} + \frac{\partial \bar{u}_i}{\partial x_j}\right]\frac{\partial \bar{u}_j}{\partial x_i} + \frac{\partial}{\partial x_i}\frac{\nu_t}{\sigma_k}\frac{\partial k}{\partial x_i} - \varepsilon + \nu \frac{\partial^2 k}{\partial x_i \partial x_j} \tag{2.12}$$

Two main approximations are required to write the main equation for k as

$$\frac{\partial k}{\partial t} + \bar{u}_j \frac{\partial k}{\partial x_j} = \tau_{ij}^R \frac{\partial \bar{u}_i}{\partial x_j} - \varepsilon + \frac{\partial}{\partial x_j}\left[\left(v + \frac{v_t}{\sigma_k}\right)\frac{\partial k}{\partial x_j}\right] \tag{2.13}$$

Where, υ_t is the turbulent eddy viscosity and σ_k is a closure coefficient. One of the main approximations is the Boussinesq approximation related to the Reynolds stress tensor:

$$\tau_{ij}^R = 2\nu_t S_{ij} - \frac{2}{3} k \delta_{ij} \tag{2.14}$$

$$S_{ij} = \frac{1}{2}\left(\frac{\partial u_i}{\partial x_j} + \frac{\partial u_j}{\partial x_i}\right) \tag{2.15}$$

where δ_{ij} is the Kronecker delta and S_{ij} is the strain tensor. Turbulent eddy viscosity is calculated as

$$\upsilon_t = C_\mu \frac{k^2}{\epsilon} \tag{2.16}$$

Considering all 6 equations up to this point (1 continuity, 3 momentums, 1 concentration and k equation), there are 7 unknown variables (3 velocity components, 1 pressure, 1 concentration, k and ϵ).

One more equation is needed to achieve a closed system of equations. So ϵ equation is introduced as

$$\frac{\partial \epsilon}{\partial t} + \overline{u}_j \frac{\partial \epsilon}{\partial x_j} = C_{\epsilon 1} \frac{\epsilon}{k} \tau_{ij} \frac{\partial \overline{u}_i}{\partial x_i} - C_{\epsilon 2} \frac{\epsilon^2}{k} + \frac{\partial}{\partial x_j}\left[\left(\nu + \frac{\nu_t}{\sigma_\epsilon}\right)\frac{\partial \epsilon}{\partial x_j}\right] \tag{2.17}$$

Table 2.3 Coefficients of $k - \epsilon$ model

$C_{\epsilon 1}$	$C_{\epsilon 2}$	C_μ	σ_k	σ_ϵ
1.44	1.92	0.09	1	1.3

(2) Large Eddy Simulation (LES)

In the LES method, eddies are separated by their size according to the local grid spacing. Large eddies are calculated directly by solving the Navier-Stokes equations, while small eddies are computed with a sub-grid model, which is based on the Boussinesq hypothesis. Essentially, a spatial filter is applied that decomposes velocities into two parts: the resolved parts ($\widetilde{U}$, which captures eddies larger than the filter width) and residual parts (u', small eddies modeled in sub-grid) (WILCOX, 1994). The filter width is related to the cell volume, and it is a limit to simulate the smallest eddy.

$$u(x,t) = \widetilde{U}(x,t) + u'(x,t) = \widetilde{u_i} + u_i' \qquad (2.18)$$

$$\widetilde{u_i}(x,t) = \iiint G(x-\xi;\Delta)u_i(\xi,t)d^3\xi \qquad (2.19)$$

where G is the spatial filter used as:

$$G(x-\xi;\Delta) = \begin{cases} 1/\Delta^3, |x_i - \xi_i| < \Delta x_i/2 \\ 0, otherwise \end{cases} \qquad (2.20)$$

and $\Delta = (\Delta x \Delta y \Delta z)^{1/3}$ is the filter size.

Then, the filtered Navier-Stokes equations for LES methods after applying the spatial filter are written as:

$$\frac{\partial \widetilde{u_i}}{\partial x_i} = 0 \qquad (2.21)$$

$$\rho \frac{\partial \widetilde{u_i}}{\partial t} + \rho \frac{\partial\left(\widetilde{u_i u_j}\right)}{\partial x_j} = -\frac{\partial p}{\partial x_i} + \frac{\partial}{\partial x_j}\left[\mu\left(\frac{\partial \widetilde{u_i}}{\partial x_j} + \frac{\partial \widetilde{u_j}}{\partial x_i}\right)\right] \qquad (2.22)$$

The interactions between large scale filtered eddies $\widetilde{u_i}$ and the Sub Grid Scale (SGS) modeled eddies u' lead to the nonlinear term $\widetilde{u_i u_j}$ written as

$$\widetilde{u_i u_j} = \widetilde{u_i}\widetilde{u_j} + \widetilde{u_i u_j'} + \widetilde{u_i' u_j} + \widetilde{u_i' u_j'} = \widetilde{u_i}\widetilde{u_j} - \tau_{ij}^{SGS} \qquad (2.23)$$

After substitution, the filtered NS equation can be expressed as:

$$\rho \frac{\partial \widetilde{u_i}}{\partial t} + \rho \widetilde{u_j} \frac{\partial \widetilde{u_i}}{\partial x_j} = -\frac{\partial \tilde{p}}{\partial x_i} + \frac{\partial \widetilde{\tau_{ij}}}{\partial x_j} - \rho \frac{\partial \tau_{ij}^{SGS}}{\partial x_j} \tag{2.24}$$

2.3.3 OpenFOAM

OpenFOAM (Open Field Operation and Manipulation) is used for numerical simulations in this study. OpenFOAM is an open-source software tool installed on the Ubuntu Linux operating system (recently a Windows version has also been released). It is a free software program with a wide range of turbulence models and solvers. The source code of the solvers and turbulence models are accessible for modification. OpenFOAM is written in C++ programming language, and it is object oriented (WELLER ET AL., 1998). Learning the functions inside the OpenFOAM environment is required for modification of the source code.

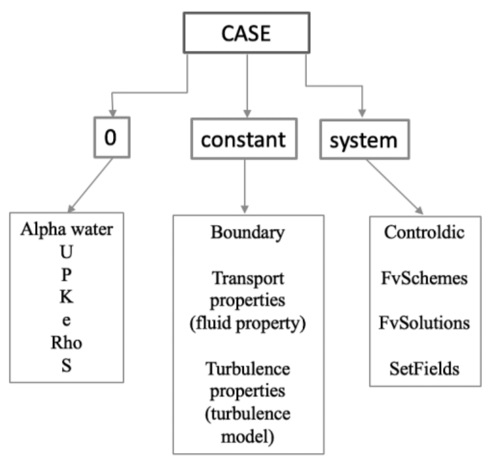

Figure 2.5 Description of the file structure of OpenFOAM

In an OpenFOAM case, normally there are three folders, and each folder has its own file structure (Figure 2.5). The solver used in the present study is a standard solver called twoLiquidMixingFoam, which solves problems for the mixing of two incompressible fluids.

2A Appendix.

2A.1 Velocity distribution in flat bends

Velocity distribution of the flow in bends has been extensively studied, and contour maps of the averaged velocity vectors are often used in evaluating flow pattern variations. Some examples of relevant experimental results are summarized as follows as references of the present study.

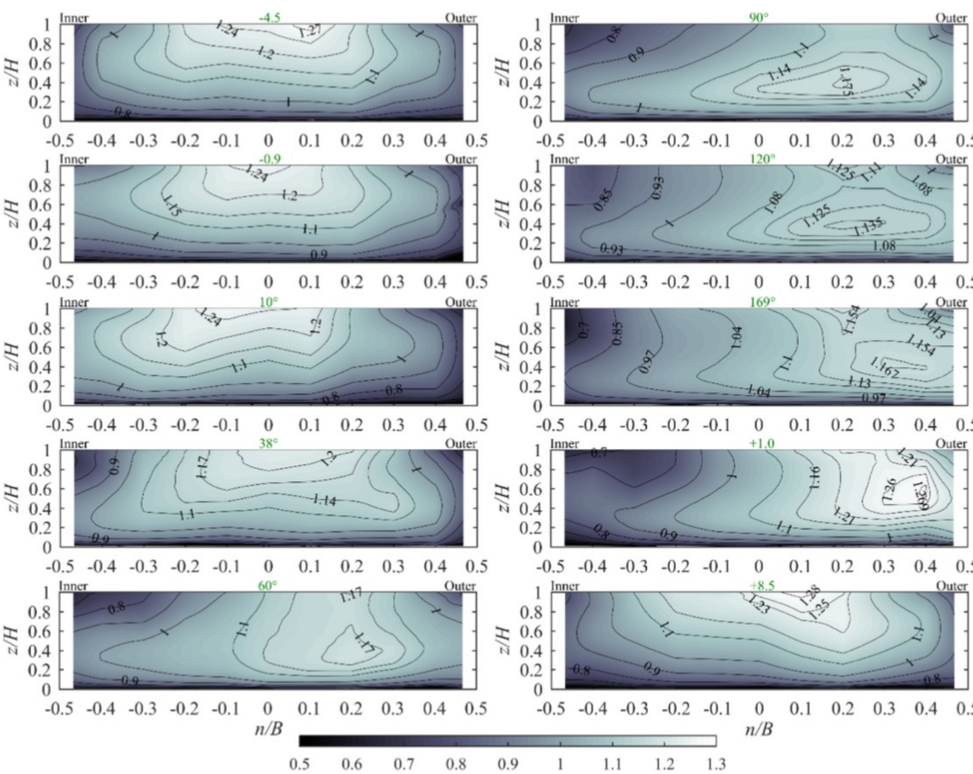

Figure 2A.1. Stream-wise velocity distribution at ten cross-sections (−4.5, −0.9, 10°, 38°, 60°, 90°, 120°, 169°, +1.0, +8.5). (From Bai, R., Zhu, D., Chen, H., & Li, D. (2019). Laboratory study of secondary flow in an open channel bend by using PIV. Water, 11(4), 659.)

The Figure 2A.1 shows contour maps of the vector representations of the averaged streamwise velocity, at ten cross-sections. The aspect ratio in this study was 5. It is obvious that the flow deflects to the inner bank at 10-degree cross-section. After a transition cross-section (38-degree), the high momentum fluid slowly transfers to the outer bank (60-degree, 90-degree, 120-degree and 169-degree), then the flow eventually reconstructs symmetry after exiting the bend in the straight outflow section (+8.5 slide).

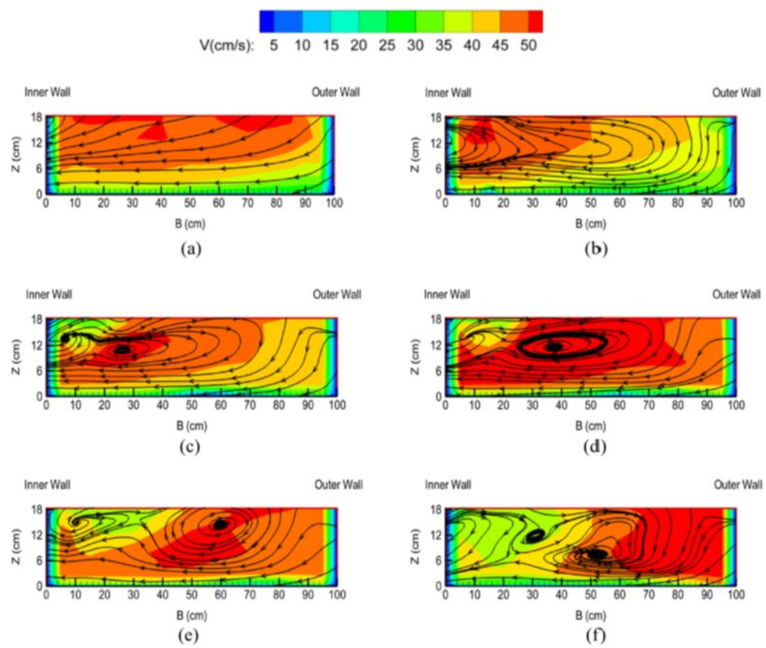

Figure 2A.2 Streamlines and Contours of Longitudinal Velocity in Different Cross Sections in a 180 Degree Sharp Bend at: (a) 0, (b) 40, (c) 80, (d) 90, (e) 130, and (f) 180 Degree Cross Sections (From Vaghefi, M., Akbari, M., & Fiouz, A. R. (2016). An experimental study of mean and turbulent flow in a 180 degree sharp open channel bend: Secondary flow and bed shear stress. KSCE Journal of Civil Engineering, 20(4), 1582-1593.)

The figure2A.2 presents the streamlines and the contour of longitudinal velocity in 0, 40, 80-, 90-, 130- and 180-degree cross sections. In this study, the aspect ratio is B/H=1/0.2=5. As can be seen in the figure, there was no circulation at the entrance, however, the fluids were conveyed oriented towards the inner wall. As longitudinal acceleration increases, velocity is not distributed symmetrically at the width of the section with high velocity area inclining towards the inner wall. The evidence of the secondary circulation can be found from the 40-degree cross section onward. The velocity contours show a clear transfer of the high velocities from the inner bank to the outer bank (90-degree to 130-degree).

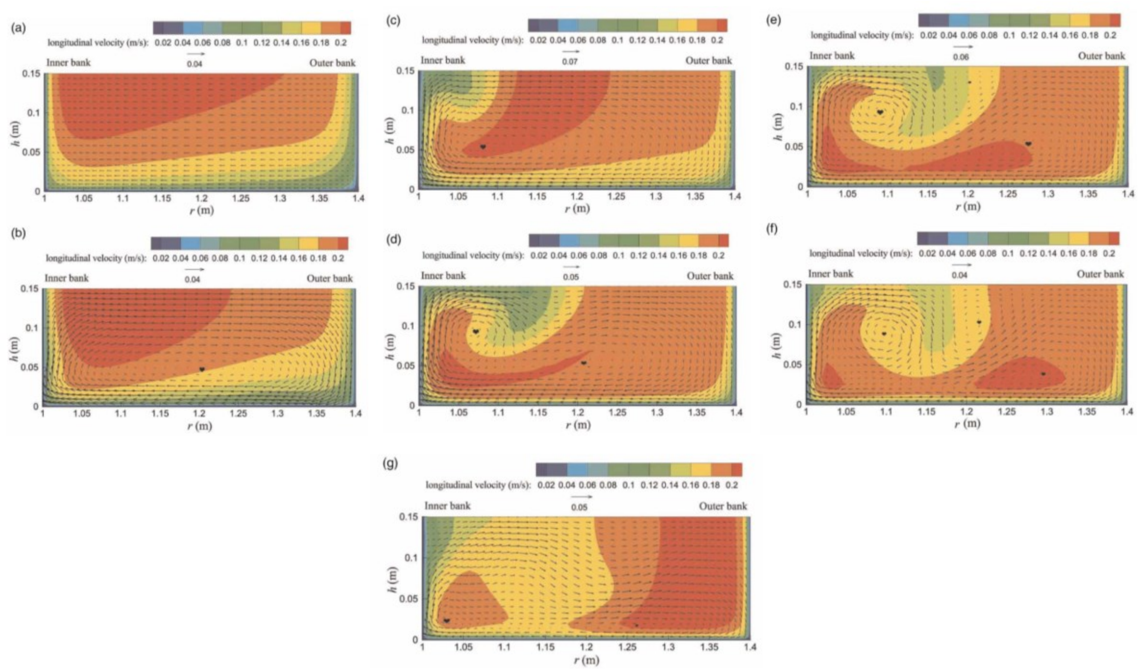

Figure 2A.3 Calculated streamlines of secondary flow and contours of longitudinal velocity at sections: (a) 0°, (b) 30°, (c) 60°, (d) 90°, (e) 120°, (f) 150° and (g) 180° (r: radial coordinate). (From Bai, Y., Song, X., & Gao, S. (2014). Efficient investigation on fully developed flow in a mildly curved 180 open-channel. Journal of Hydroinformatics, 16(6), 1250-1264.)

The figure 2A.3 shows the numerical results of the circulation pattern and streamwise velocity contour maps along the bend. The width to depth ratio is B/H=0.4/0.15=2.67. At the start of the bend, the zone of maximum streamwise velocity is found near the inner bank and water surface. As the secondary flow developed, the high momentum fluid was transported toward the outer bank, specifically, the 'maximum' velocity zone shrinks in the transverse direction with the core slowly moving towards the outer bank

2A.2 velocity distribution with low aspect ratio

Given a width-depth ratio of 2, secondary currents of Prandtl's second kind which are generated by the non-homogeneity and anisotropy of turbulence can be expected. It has been reported that secondary currents in real channel flows will easily be distorted with single or combined effects from the side-wall, the free-surface, and the bed roughness in actual channel flows (NEZU AND NAKAGAWA, 1993). In case of the anisotropy at the boundaries, for example, one of the fundamental features of an ideal secondary flow is that bed shear stress increases towards the secondary current downflow regions and decreases along secondary current upflow direction (Figure 2A.4) (PERKINS, 1970; TOWNSEND, 1976). For a rectangular cross-section with the aspect ratio of 2, a two-counter-rotating-cell pattern with each occupying one half of the section is expected. When the experiment was firstly conceived, it was realized that a higher aspect ratio (at least 5) would be more practical for natural streams, however, such an aspect ratio value would not be possible in a small flume as ours, especially if we were also going to inject a jet. A larger aspect ratio (5 for example) would have required a very shallow flow (<4 cm), which would bring about a lot of problems in jet discharging and nozzle installation. Nonetheless, we could have tried using a flow depth less than 10 cm for better analysis.

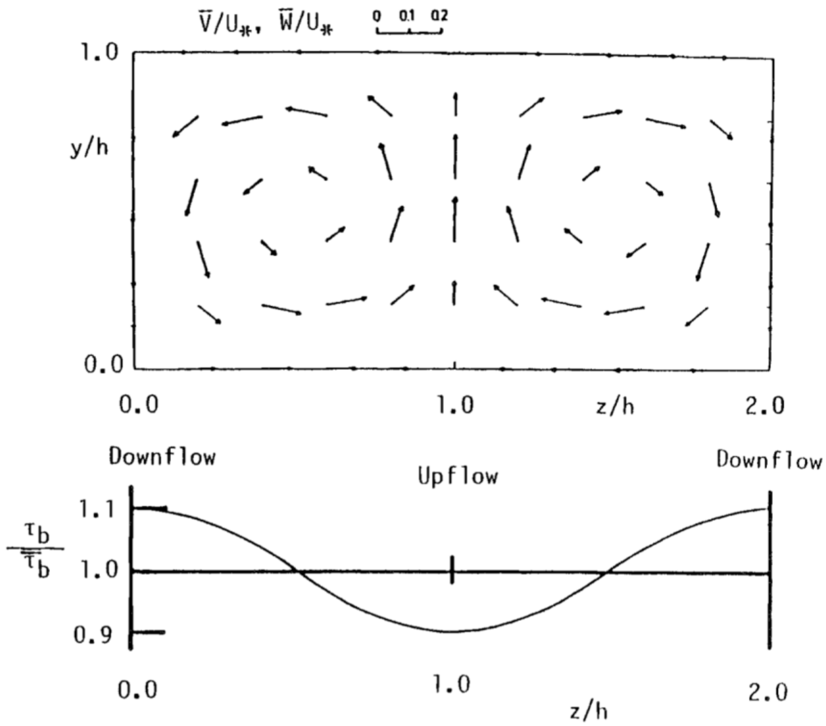

Figure 2A.4. Ideal cellular secondary currents and the corresponding bed shear stress. (*From Nezu and Nakagawa, 1993 Nezu, I., & Nakagawa, H.(2017). Turbulence in open-channel flows. Routledge.*)

Unfortunately, measurements across the cross-section in the straight channel upstream of the bend have not been collected, so whether the flow had developed any secondary currents cannot be determined. With this small aspect ratio, it is very rational to assume that Prandtl's secondary flow of the second kind arise in the straight section since boundary-caused turbulence anisotropy is dominant in this case. Given this, the reason for failing to observe the two full-depth counter-rotating cells pattern with downflow in the center of the section was that if secondary currents of Prandtl's second kind had developed in the straight entrance flow, they had dissipated by the 37-degree cross section (Figure 4.2a) with the flow proceeding in the bend. As can be seen in Figure 4.2a (which shows secondary vectors in flow without jet at 37-degree section), a reasonable pattern of secondary circulations was observed as expected in bend flow (main channel cell of Prandtl's first kind, and outer bank cell of Prandtl's second kind).

Figures 2A.5 show the streamlines of the flow in previous studies that also utilized a very small aspect ratio in their set up. Similarly, two full-depth counter-rotating cells with downflow in the center were not detected in the bend section. The channel section used has dimensions of 40.3×40.3 cm, and the flow depth is 15cm, so the value of the aspect ratio is 2.68.

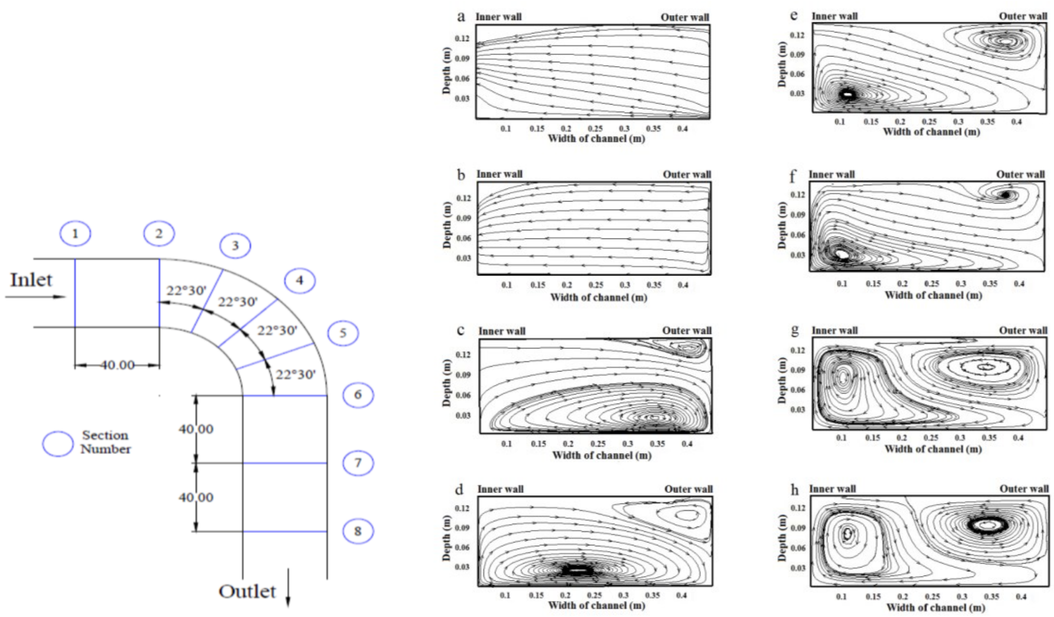

Figure 2A.5 position of cross-sections (Left) and secondary flow at different cross-sections (Right): a- Section 1; b- Section 2; c- Section 3; d- Section 4; e- Section 5; f- Section 6; g- Section 7; h- Section 8. (From Gholami, A., Akbar Akhtari, A., Minatour, Y., Bonakdari, H., & Javadi, A. A. (2014). Experimental and numerical study on velocity fields and water surface profile in a strongly-curved 90 open channel bend. Engineering Applications of Computational Fluid Mechanics, 8(3), 447-46.)

The second case showing the streamlines and the velocity distributions were from (Abhari et al., 2010). For their case, the channel was of rectangular cross section 0.6 m width, 0.7 m height with 1.8 m radius of bend to centerline, and the flow depth is 0.2m. the aspect ratio is 3.

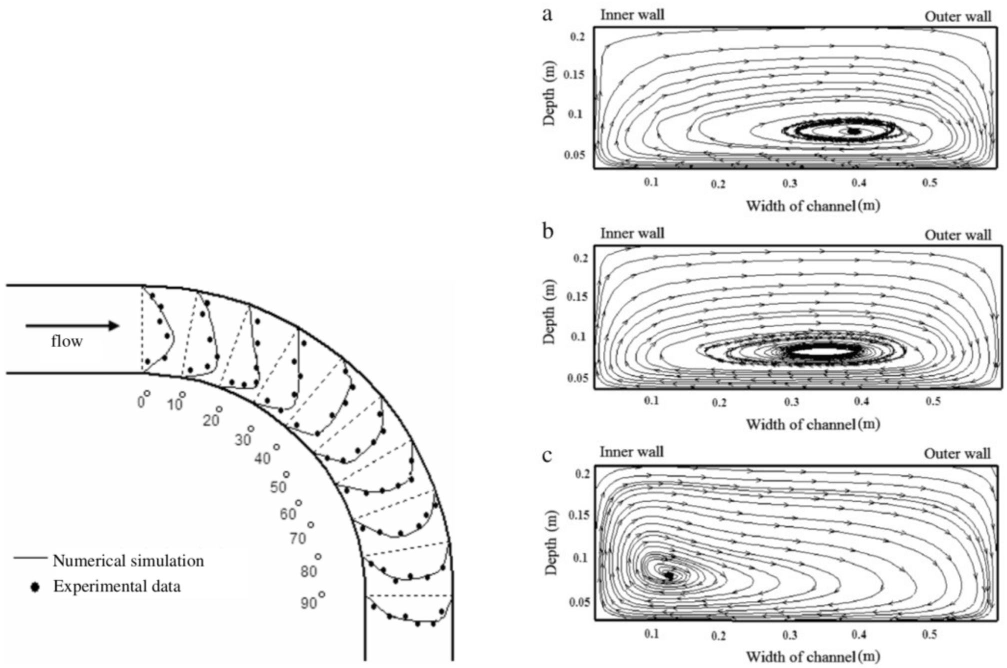

Figure 2A.6 Variations of velocity along the channel bend (Left) and streamlines at different vertical sections (Right): (a) 30°, (b) 60°, (c) 90° (From Abhari, M. N., Ghodsian, M., Vaghefi, M., & Panahpur, N. (2010). Experimental and numerical simulation of flow in a 90 bend. Flow Measurement and Instrumentation, 21(3), 292-298.)

Chapter 3 Experimental Studies on the Influence of Negatively Buoyant Jets on Flow Distribution in a 135-Degree Open Channel Bend

Published in the Water 2022, 14, 1898., https://doi.org/10.3390/w14121898

Xueming Wang, Colin D. Rennie and Abdolmajid Mohammadian

Abstract: The present paper aims to investigate the evolution of velocity fields as well as secondary flows in an open channel bend under the influence of negatively buoyant jets. A 135-degree open channel bend was used for experiments, and the jet nozzle was located along the outer bank in the straight section upstream of the bend. Efforts were made to specify the flow structures with high precision measurements of three-dimensional velocities by means of a three-dimensional PIV (Particle Image Velocimetry) technology. The experimental results show that the jets comparatively affect the flow structure at the beginning and exit of the flow in a bend. Although the jets had little effect on the maximum streamwise velocity, complex secondary flow patterns and properties were found to be influenced due to the occurrence of the negatively buoyant jets in the bend.

Keywords: bend flow; PIV; velocity distribution; secondary flow; negatively buoyant jets

3.1 Introduction

One of the characteristic features caused by the streamline curvature in the open channels is the existence of cross-stream circulation (ROZOVSKII,1957; ENGELUND AND SKOVGAARD,1973, STRUIKSMA ET AL., 1985), and Blanckaert and de Vriend (2004). It has been found that there are two types of cross-stream motions. One is the classic helical motion located in the center of a channel. This kind of circulation results from the centrifugal force and covers a large part of the cross-sectional area (the main vortex). The other one is a relatively weak circulation with opposite rotation that typically forms near the outer bank of the bend (the outer bank vortex); see Blanckaert and de Vriend (2003). Studies on the flow structures of river bends have confirmed that these secondary circulations play an important role in scalar dispersion, river evolution and performance of hydraulic structures such as bridge piers and abutments, Blanckaert and de Vriend (2004). However, in river engineering, formation and momentum transport of secondary flow structures are not yet fully understood, and further discussion is required.

Extensive studies have been conducted on the secondary flow in channel bends since the first report of this cross-sectional motion (Thomson,1876; Shukry, 1950; Naot and Rodi, 1982; Odgaard and Bergs,1988; Rhoads and Welford,1991; Whiting and Dietrich, 1993; Kawai and Julien, 1996; Gholami et al., 2014). Most of the attention has been paid to the strength of the secondary flow and the interactions between the secondary flow and the main flow. Blanckaert and Graf (2001) conducted experiments on a bend flume with detailed information on the three-dimensional velocity, the six turbulence stresses components, as well as the turbulent kinetic energy, especially for the outer bank wall region. They confirmed that the downstream velocity at the outer bank was higher than that of the straight channel, and the core of the maximum velocity was located in the area between the main circulation cell and the outer bank cell. Due to the combination effect of the outer bank cell and the reduction of turbulence near the outer bank, the bank perimeter and the bottom were protected from erosion. Then, Blanckaert and Graf (2001) developed a nonlinear model to consider the interaction between the secondary flow and the downstream velocity by using a 120-degree laboratory bend with a mobile bed. With the analysis of momentum transport properties, Blanckeart and Graf concluded that the momentum transport, which gave rise to the secondary flow, dominated the velocity distribution of the downstream flow. Termini and Piraino (2001) discussed the relation between the evolution of the cross-sectional flow motion and the depth-to-width ratio, and they concluded that the outer bank cell would only exist with 'small' depth-to-width ratio flows. They also reported that due to the outer bank circulation, the shear stress at the outer side of the bend could maintain low values. Vaghefi et al. (2016) investigated the secondary flow and bed shear stress in a 180-degree sharp open channel bend, and they found that the maximum strength of the secondary flow occurred at the second half of the bend, but no outer bank cell information was given. Wei et al. (2016) investigated the curvature-induced secondary flow regarding different curvature ratio, Froude number and roughness coefficient conditions. Wei et al. confirmed the observations from Blanckaert (2009) that the increase in the secondary flow magnitude caused by the curvature ratio would reach a maximum value in strongly curved channels. They attributed the loss of magnitude growth to the nonlinear interaction between the primary and secondary flow.

In urban life, when there are rivers or estuaries nearby, discharging into rivers is an accessible and economical way to dispose of domestic wastewater effluent. Different discharging properties generate a great diversity of diffusion behavior, and the receiving water body can also readily influence the physical mixing processes; see Blanckaert (2009).

Studies of dense jets are mostly vertical or inclined where the jets are discharged into stagnant ambient, e.g., Kikkert et al. (2007), Oliver et al. (2013), and Zhang et al. (2016). Only a few studies in the literature have focused on dense jets in a flowing ambient. It has been reported that even a weak flow can increase the initial dilution significantly; see Choi et al. (2016). The initial mixing and the subsequent spreading of dense jets depend on the jet behavior. In the presence of currents, the problem becomes substantially more complicated. Understanding mixing of an effluent jet in an open channel bend is of particular interest, as the secondary circulation induced by the bend could enhance transverse dilution; see Schreiner et al. (2018). The objective of this research is to investigate secondary flow structures in a channel bend under the influence of fully developed horizontally turbulent jets experimentally, especially considering the density change of the jets. By means of particle image velocimetry (PIV) technology, information on the averaged three-dimensional velocity field can be obtained. Moreover, the data gained can be further used to comment on related environmental problems in river management.

3.2 Experimental Setup and Procedures

3.2.1 Laboratory Flume and Flow Properties

In this study, experiments were conducted to explore flow structures in a 135-degree bend flume with horizontal dense jets discharged into the straight section on the outer wall upstream of the bend. Three different density values were considered to investigate the influence of mixing behavior by dense jets on flow structures in the bend. A sketch of the experimental set-up, as well as the coordinate system, is given in Figure 3.1.

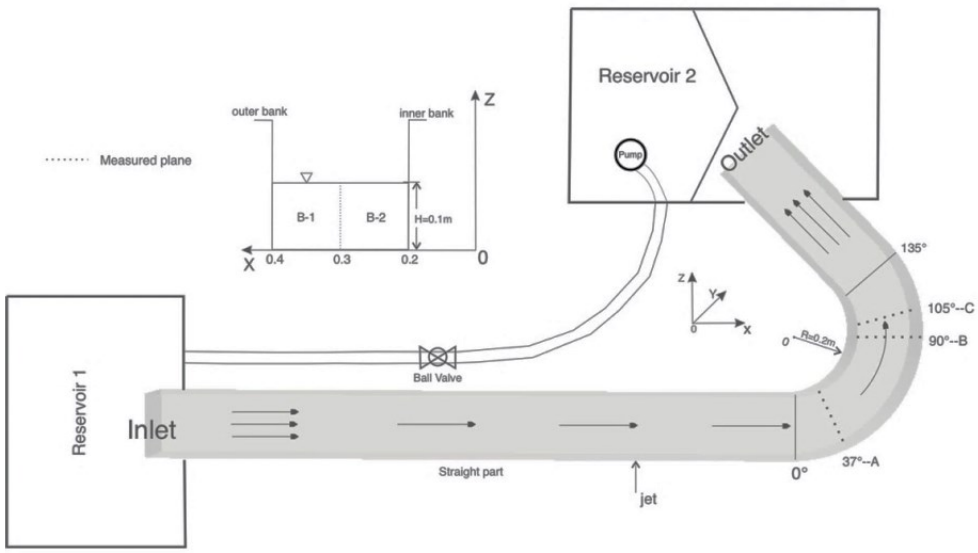

Figure 3.1 Sketch of the bend flume and the coordinate system with the flow condition in the flume.

The flume was made of 1.27cm inch thick clear acrylic, which ensured a good view of the flow both from the bottom and the sidewalls. The straight part of the flume in the inlet section was 2.2m in length, and at the outlet side, the straight reach was approximately 0.55m long. The width and depth of the flume were both uniformly 0.2m, and the centerline curvature radius (Rc) of this bend was 0.3m. The current flume was classified as a strongly curved open channel bend due to Rc/b (b is channel width) = 1.5. At the entrance and the exit of the channel, two stainless steel reservoirs were set separately for water supply in the flume. A pump was placed in Reservoir #2 (Figure 3.1) to convey water to Reservoir #1 via a plastic pipe with an inner diameter of 12.7cm. The flow rate in the flume was controlled by a ball valve near Reservoir #1, and a sharp crested weir was placed at the flume exit to adjust the water level in the channel. To measure the discharge with the flume, Reservoir #2 was divided into two components, between which a 90-degree V-notch weir was installed.

The jet nozzle was located at the straight upstream section of the bend entry section, about 55 cm away from the beginning of the bend, and it was set at the height of 4.5cm to avoid boundary effects when the effluent was discharged. The length of the horizontal section of the nozzle was adequately long to ensure that the jet was well developed. In order to obtain a horizontal jet perpendicular to the main flow, a nozzle with an inner diameter of 0.95cm was installed onto the outer bank of the bend wall at the above-mentioned location. Saline water was used as effluent in this study, and fresh tap water was used as the ambient water. The density of effluents was calculated according to the equation of state proposed by Millero and Poisson (1981). The equation was given as:

$$\rho = \rho_t + AS + BS^{\frac{3}{2}} + CS \tag{3.1}$$

Where A $= 8.24493 \times 10^{-1} - 4.0899 \times 10^{-3}T + 7.6438 \times 10^{-5}T^2 - 8.2467 \times 10^{-7}T^3 + 5.3875 \times 10^{-9}T^4$, B $= -5.72466 \times 10^{-3} + 1.0227 \times 10^{-4}T - 1.6546 \times 10^{-6}T^2$ and C= 4.8314×10^{-4}, and the and ρ_t is the density of water that varies with the temperature as follows:

$$\rho_t = 999.842594 + 6.793952 \times 10^{-2}T - 9.095290 \times 10^{-3}T^2 + 1.001685 \times 10^{-4}T^3 - 1.120083 \times 10^{-6}T^4 + 6.536336 \times 10^{-9}T^5 \tag{3.2}$$

In the current study, salinity was set to 3.5, 10 and 16.5 to achieve the desired density difference. As the density of ambient water is lighter than that of the effluents, negative buoyant jets were formed. A constant discharge rate was acquired by setting a constant head reservoir at an elevation of 85 cm above the flume bottom.

To better evaluate the cross-stream motion in the bend, a local coordinate system was used to define the measured planes as shown in Figure 3.1. Specifically, the origin was at the centerline of each bend section, and the stream-wise, span-wise, and vertical directions are denoted by s, n, and z correspondingly. Hence, the three time-averaged velocity components are u_s, u_n and u_z, indicating the velocities in the streamwise (longitudinal), span-wise (transverse) and vertical directions, respectively.

Hydraulic parameters were measured and collected in the straight channel at 0.55m upstream of the bend entrance (Table 3.1). Each experimental measurement was taken until the flow was steady and uniform. The depth of the flow was 10cm, with an averaged cross-sectional velocity of about 0.1m/s. The water in the flume was replaced after every second measurement to ensure the ambient bend flow maintained low salinity.

Table 3.1 Hydraulic characteristics of main flow in bend

B (cm)	H (cm)	R_c (cm)	Q (m^3/s)	G (ms^{-2})	U (m/s)	Re	Fr
20	10	20	2	9.8	0.1	22024	0.22

B is the flume width, H is the flow depth, Rc is the centerline curvature radius, Q is the main flow discharge. g is the gravitational acceleration; the Reynolds number is calculated by Re = UR/v; the Froude number is defined by Fr = U/(gH)1/2.

3.2.2 Measurements and procedure

Measurements of the velocity distribution were conducted using a Stereo-PIV system from LaVison, including the DaVis (Version 8.4) software for data acquisition and post processing. It is worth noting that measurements obtained with Stereo-PIV contained three velocity components ($u1$, $u2$ and $u3$) over the two-dimensional (n-z) planes (two-dimensional three-components). All the measured surfaces were located in the bend section. Due to the current setup, 8 surfaces were measured, which yielded 4 cross-sectional planes (37°, 90°, 105° and 125°). Image planes were located in the n-z plane to collect the velocity distribution in three dimensions at the same time.

The laser beam was fixed on a moveable cart under the flume and shot from below to avoid any possible reflection on the sidewall of the flume during the data recording session. The laser emission indicator was held with a three-prong extension clamp, then the clamp was fixed on the cast iron support ring stand. To meet the requirements of laser safety regulations, a canopy was built and placed on top of the flume to prevent laser light from propagating from the water's surface. In addition, nine blocking boards covered by black, light absorbing material were arranged along the inner side of the flume to restrain the light scattering from the flume wall. Two cameras were placed horizontally at the outer bank side, towards the inner bank, at the same elevation as that of the calibration plate center (Figure 3.2c). The angle between the two cameras was set by trying to minimize the calibration evaluation value; hence, the angle was different for each measured plane.

A three-dimensional calibration target (two-level calibration plate from LaVision named #106-10), with white dots on both front and back sides, was chosen for scaling and calibrating. The calibration plate had dimensions of 10 cm x 10 cm, thus each measured image plane occupied one half of the flume width, and two image planes were required to capture a channel section. In the present test, both sides of the calibration plate were used during the calibration (Figure 3.2b). The result of the calibration was then used in the mapping process, and a high-quality calibration generated an accurately mapped field of view. To diminish the influence of the deformation root from curvature during the mapping, a value used to evaluate calibration results was controlled at around 0.1. As for the focusing problem caused by the oblique view of cameras, Scheimpflug adapters were used to ensure the field of view was uniformly focused. In addition, stereo self-calibration was engaged in order to minimize errors in the mapped image (check PRASAD AK, JENSEN K, 1995 for more references).

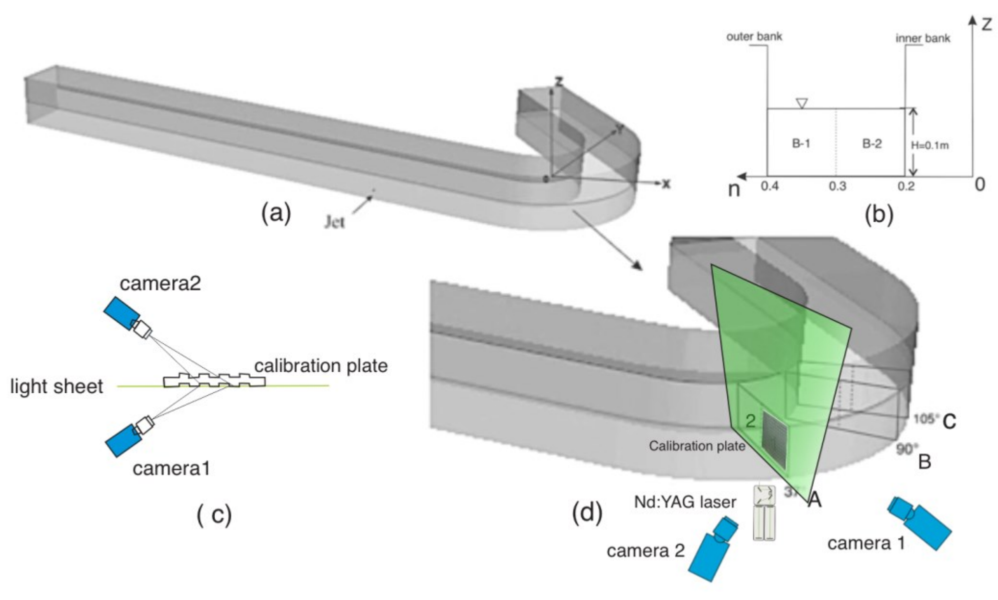

Figure 3.2. PIV setup with a laser and a camera: (a) a sketch of the bend with the coordinate system (b) n-z plane; (c)camera layout (d) Configuration for the PIV experiments

The illuminating components of the PIV system were two Nd-Yag pulsed laser beams (100 mJ per pulse at a wavelength of 532 nm), and the thickness of the optic sheet can be adjusted within a range from 3 mm to 5 mm. The flow was seeded with glass particles with a mean diameter of 20 μm and a density of 1.1×103kg/m3. The required particle concentration is usually defined by the number of particles per pixel. The particle images were captured by two dual-frame sCMOS cameras with a frame rate of up to 50 Hz. The resolution of the cameras was 1028 × 2560 pixels with pixel size of 6.5 × 6.5mm2. The frequency of laser firing and the image capturing by the cameras were synchronized by a timing unit. In this study, sample pictures were taken with a corresponding time interval (3.7ms) calculated depending on the flow velocity. Each measurement yielded a series of 1000 double-frame image pairs to be analyzed. The experimental method was verified by measuring velocity distribution in the straight section, where the flow structure was less complex. In the post-processing session, the sample image pairs were firstly manipulated by an image processing method so that quality improved pictures could be obtained for vector calculation interpreted using a multi-pass stereo cross-correlation algorithm. The size of the interrogation window decreased based on the number of pixels; the size of 64×64 pixels, 48×48 pixels and 32×32 pixels were used for analysis. There was an overlap of 50% in the horizontal direction for 64×64 pixels, 25% circular overlap for 48×48 pixels, and 0% for 32×32 pixels. In addition, median filters were applied for image correcting and data restraining based on calculating flow averages and standard deviation.

A total of 8 surfaces were measured in this study, and measurements were made under steady, uniform flow conditions, as summarized in Table 3.2. To obtain a better calibration result for each section, the laser indicator and the cameras were circumspectly positioned with the same set-up as mentioned above. The velocity fields of four cross-sectional planes were generated, and extra measurements were also operated for repeatability validation. It should be noted that there were data fluctuations at the edge of each captured image plane, which resulted from the inevitable high intensity from the light source at the boundary. Thus, an uncertainty evaluation was performed to ensure data accuracy.

Table 3.2 Table of experiments

Slice #	Sjet	Smain	Ujet(m/s)	Umain(m/s)	ρjet(kg/m3)	△ρ	cross-sectional plane (degree)
A	3.5	0	0.2	0.1	1000	3	37
	10	0	0.2	0.1	1005	8	37
	16.5	0	0.2	0.1	1010	13	37
	-	0	-	0.1	-	-	37
B	3.5	0	0.2	0.1	1000	3	90
	10	0	0.2	0.1	1005	8	90
	16.5	0	0.2	0.1	1010	13	90
	-	0	-	0.1	-		90
C	3.5	0	0.2	0.1	1000	3	105
	10	0	0.2	0.1	1005	8	105
	16.5	0	0.2	0.1	1010	13	105
	-	0	-	0.1	-	-	105
D	3.5	0	0.2	0.1	1000	3	125
	10	0	0.2	0.1	1005	8	125
	16.5	0	0.2	0.1	1010	13	125
	-	0	-	0.1	-	-	125

3.2.3 Analytical methods

The measured data from the current PIV set-up yielded both the instantaneous three-dimensional velocity components and the averaged flow field at each measured section. The sampling frequency of the current PIV measurements was nearly 30 Hz. According to previous experimental studies, it can be conceived that such a frequency is below the frequency of the periodic motion and small-scale turbulence (Graftieaux and Michard, 2001). Although the current sample size is insufficient to show a correlation from the snapshots, it is capable of calculating the averaged velocity field. Therefore, an ensemble of averaged techniques was employed in extracting the averaged velocity and secondary circulation cells in the field of interest. The mean velocities (u_s, u_n, u_z) and fluctuating velocity components (u_s', u_n', u_z') were derived from the instantaneous velocities through the measured data. In this paper, mean flow and secondary flow quantities are evaluated with the averaged velocity.

The calculation of the vorticity is based on a MATLAB open-source code provided by Sebastian Endrikat (2022). The code detects the vortex in the z-axis through the x and y components of the velocity field and presents the location (x-y plane), size and strength of every vortex identified.

3.3 Results and Analysis

3.3.1 Mean flow patterns and properties

Among all measured planes, the ones with lower uncertainty values (gathered di-rectly from the DaVis) were selected for further investigation. The averaged streamwise velocity distributions without the dense jets over the four measured cross-sections (37°, 90°, 105° and 125°) are presented in Figure 3. All the contour profiles are smoothed using an interpolation method from MATLAB named Biharmonic (v4). Due to the current setup, two measured surfaces resulted for each cross-sectional plane. However, the streamwise velocity is the out-of-plane component; therefore, the streamwise velocity contour of all the cases at the outer bank side and inner bank side were computed separately for better analysis. Furthermore, it is acknowledged that the data acquired at the image edges using PIV technology were less accurate. Therefore, a 1 cm wide rectangular shadow was marked on the stitch line of the two images at one cross-sectional plane and named an unreliable data zone.

To better understand the mechanisms leading to velocity redistribution, the measured velocity field were normalized by the overall mean streamwise velocity U =Q/(BH) in the upstream straight channel. In non-dimensional coordinates, the inner wall and the outer wall are n/B=0.5 and -n/B=-0.5 respectively and the water surface is at z/H=1.

The averaged streamwise velocity distributions without the dense jets over the four measured cross-sections (37◦, 90◦, 105◦ and 125◦) are presented in Figure 3.3, and the normalized streamwise velocity components of the flow with the incurrence of the jets, us/U (U = 0.1 m/s), are given in Figure 3.4. The highest value of us/U is around 1.4, implying that the velocity in the bend was redistributed and can go above the mean velocity in the straight channel. It can easily be noticed that the velocity magnitude at the outer bank side is increasing as the flow is approaching the bend exit (left side in Figure 3.3a–d). As expected, high momentum fluid was gradually transported from the inner side at the entrance to the outer bank near the exit; see Dietrich and Whiting (1989). As the flow proceeds through the bend, the contour interval of the streamwise velocity in the outer bank half becomes larger, which means that the velocity gradient is flattened as the flow exits the bend.

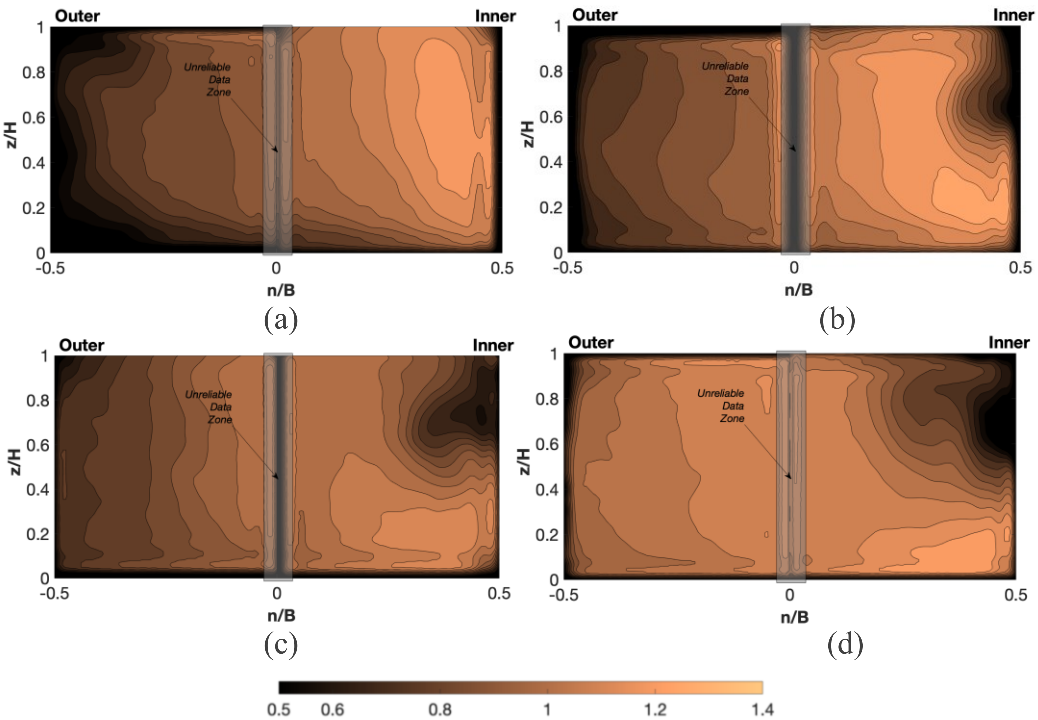

Figure 3.3 Normalized stream-wise velocity (u_s) of the measured cross-sections without the jets (a)37-degree (b)90-degree (c)105-degree (d)125-degree.

It can also be observed that, with the occurrence of negatively buoyant jets (Figure 3.4), the patterns of streamwise velocity distribution at the outer bank near the left bottom corner were slightly affected, and the region of the low velocity area expands towards the centerline as salinity increases. However, this phenomenon only presented at the beginning of the bend. In contrast, at the inner bank side, the influence on the velocity pattern caused by the negatively buoyant jets was mostly observed at the exit of the bend (e.g.,105-degree and 125-degree, Figure3.4c and 3.4d), as opposed to the bend entrance. As shown in Figure 3.4d (1- 3), there were low velocity regions near the inner bank at the upper half of the channel that were expected as the separation zones of bend flows, and the size of the low velocity core area are enlarged (deeper and wider) with increase in salinity. This can indicate that the dense jets in the straight channel followed the main flow before entering the bend and were transported to the inner bank as the flow moved forward through the bend via secondary flow motion. It is worth noticing that the separation zone is not present at the bend entrance; it progressively develops in the bend. As shown in Figures 3.4a (2) and 3.4a (3), no separation zone was discovered, meaning that the formation of the separation zone can be postponed with higher salinity jets. Moreover, in the developed separation zones, the cores of these zones are dragged against the free surface as salinity increases (Figure3.4a, 3.4b and 3.4c) for all the measured planes.

Further investigation of the qualitative analysis of the velocity profiles was described using the nondimensional maximum streamwise velocity (u_{smax}/U). Figures 3.5a exhibit the maximum streamwise velocity. As can be seen, for all cases, the maximum streamwise velocity slightly increases when the flow proceeds form 37-degree to 90-degree, reaching the lowest value (among all the measured planes) at the 125-degree cross-sectional plane. The maximum streamwise velocity of the case without the jet shows the most similar trend as that of the jets with the largest salinity. It can be deduced that the maximum velocity magnitude in the bend is mostly dominated by the streamwise velocity, and the presence of the saline jets increase the maximum streamwise velocities in the bend.

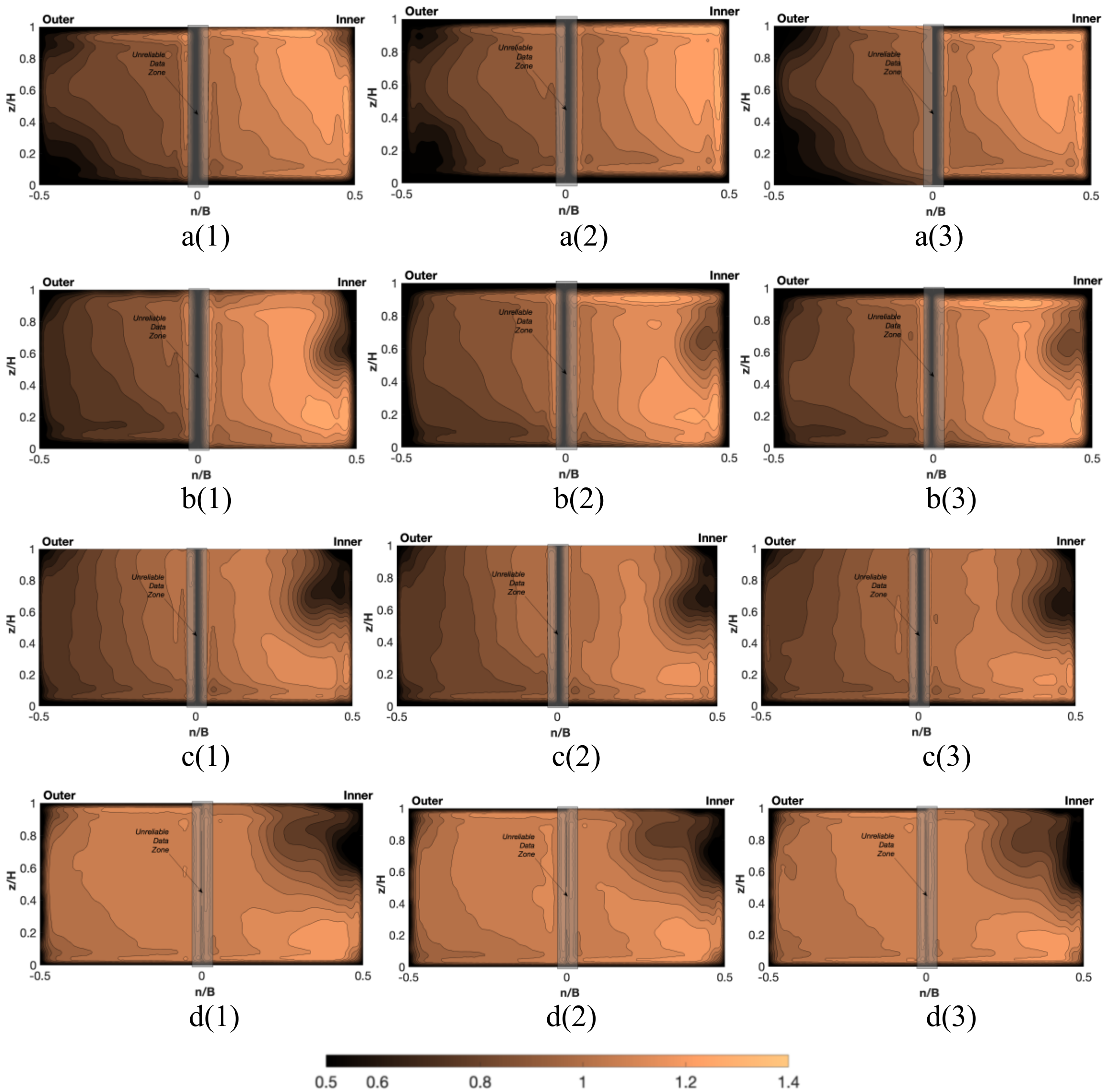

Figure 3.4. Normalized stream-wise velocity (u_s) distribution at the measured cross-sections (a)37-degree (b)90-degree (c)105-degree (d)125-degree. The numbers 1, 2 and 3 denote different jet conditions (1)- S=3.5; (2)-S=10; (3)-S=16.5.

The evolution of the maximum transverse and vertical velocity, however, presents partial similarities for different salinity conditions. As demonstrated in Figures 3.5b and 3.5c, the overall patterns of the evolution for both the maximum transverse velocity and vertical velocity are relatively consistent. Due to the presence of the negatively buoyant jets, the maximum transverse and vertical velocity were reduced by the jets at the beginning of the bend. When the flows are close to the bend exit, the maximum transverse and vertical velocity exceed the maximum values of the ones without jets. Figure 3.5d and 3.5e shows the location of the maximum streamwise velocity in the vertical direction and the spanwise direction respectively within a measured plane. As can be seen, the negatively buoyant jets had little impact on the location of the maximum streamwise as flow proceeded the bend, more precisely, the jets carried more influences on the maximum streamwise velocity in the vertical direction than that in the transverse direction. However, the jets raised the elevation where the maximum streamwise velocity was, especially at the beginning and the exit region of the bend.

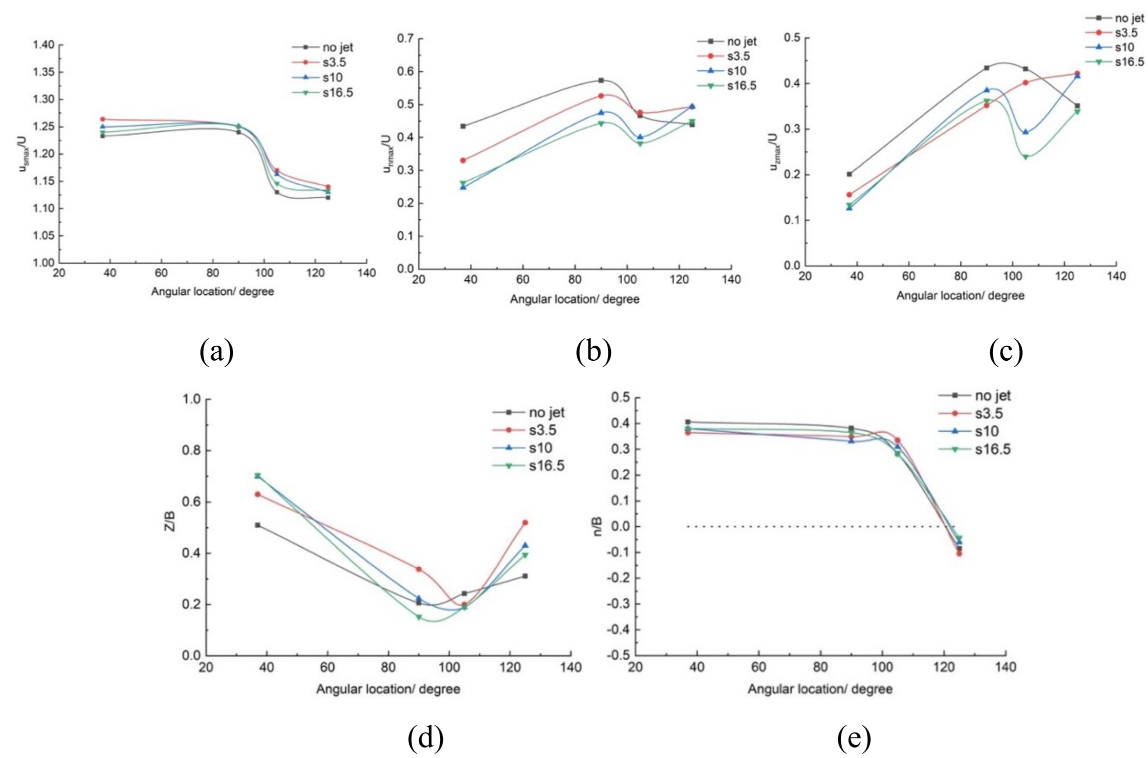

Figure 3.5 Dimensionless maximum velocities proceed at the bend with different jet conditions (a) Streamwise velocity (b) Transverse velocity (c) Vertical velocity (d) Evolution of the maximum streamwise velocity in the vertical direction (e) Evolution of the maximum streamwise velocity in the transverse direction.

The distribution of the normalized depth-averaged value of streamwise velocity component, $u_{s\text{-}depth}/U$, is given in Figure 3.6. Here, the core of the maximum depth-averaged streamwise velocity slowly moves to the outer bank, which also proves the transfer of high momentum fluids caused by the secondary flow. Interestingly, the saline jet appears to have little influence on the distribution of streamwise velocity.

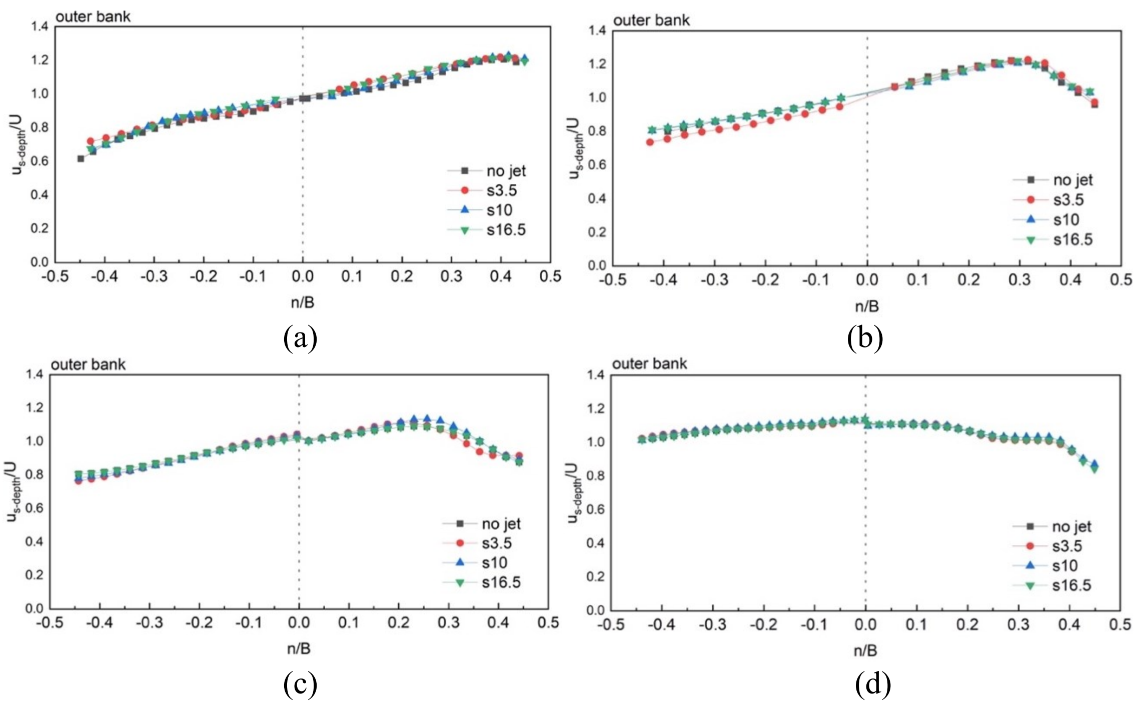

Figure 3.6 Dimensionless depth-averaged streamwise velocity across each sectional plane, with different jet conditions: (a) 37-degree plane (b) 90-degree plane (c) 105-degree plane (d) 125-degree plane

3.3.2 Cross-sectional flow properties

Figure 3.7 shows the distributions of the normalized transverse velocity; in the current setup, each cross-sectional plane was combined using two measurements taken at the outer bank side and the inner bank side, separately. As shown in Figure 3.7, the highest transverse velocities were observed in the deepest part of each cross-section at the channel bottom boundary. As expected, the fluids flow towards the inner bank at the bottom and towards the outer bank at the water surface, which forms a transverse flow also known as helical flow. As previously shown in the distribution of the streamwise velocity, the dense jets influence the transverse flow at the lower outer corner of the bend entrance. At the 37-degree plane (Figure 3.7a(2)-(4)), the transition area between the inward velocity and the outward velocity region in the lower part of the outer bank side of the cross-sectional plane is enlarged by the jets. As salinity increases, the core of the high transverse velocity region expands in the vertical direction, pushing the fluids that go towards the outer bank in the upper part of the cross-section to the water surface.

This phenomenon can also be observed at the rest of the measured planes (Figure 3.7b, 3.7c and 3.7d). Figure 3.7b(1) shows a velocity increase close to the water's surface, and this high velocity region gradually moves to the outer bank as the flow continues in the bend (Figure 3.7c(1) and 3.7d(1)). With the occurrence of jets, the transport of the high velocity region to the outer bank of the bend is accelerated.

In the left upper corners of each cross section, there is fluid moving in the opposite direction as the ambient flow. According to the location of the regions, they are called the outer bank circulation zone and inner bank separation zone respectively. It is very interesting that the size of the inner bank zone decreases as salinity increases at each cross-section, while the outer bank zone first decreases then increases with the increasing of salinity (Figure 3.7 a, b, c, and d).

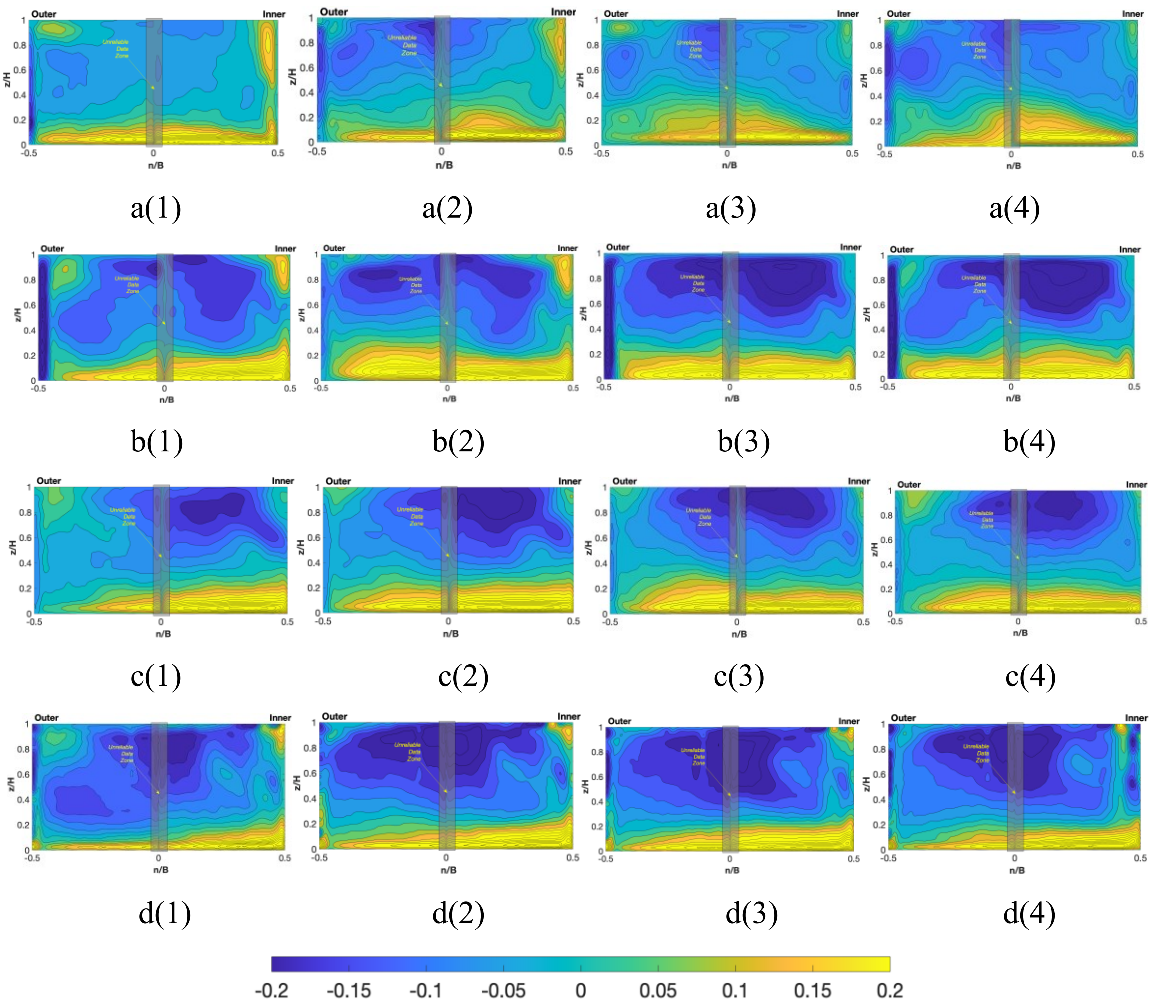

Figure 3.7 Dimensionless transverse velocity distribution at (a)37-degree (b)90-degree (c)105-degree (d)125-degree. The numbers 1, 2, 3 and 4 denote different jet conditions (1)-no jet; (2)-S=3.5; (3)-S=10; (4)-S=16.5.

Figure 3.8 demonstrates all the dimensionless vertical velocity distributions of all the measured planes. It has been proven by many researchers that the fluids in the bend follow an upward path near the inner bank and go downward at the outer bank. This pattern is also well captured by the current measurements. Moreover, the size of the inner side upward flow region in the beginning of the bend is larger than that of the subsequent downstream cross-sections (Figures 3.8a and 3.8b). Specifically, the tops of these upward flow regions are found to be slightly stretched and bent towards the centerline, which implies the existence of the separation zone (Figures 3.8b, 3.8c and 3.8d).

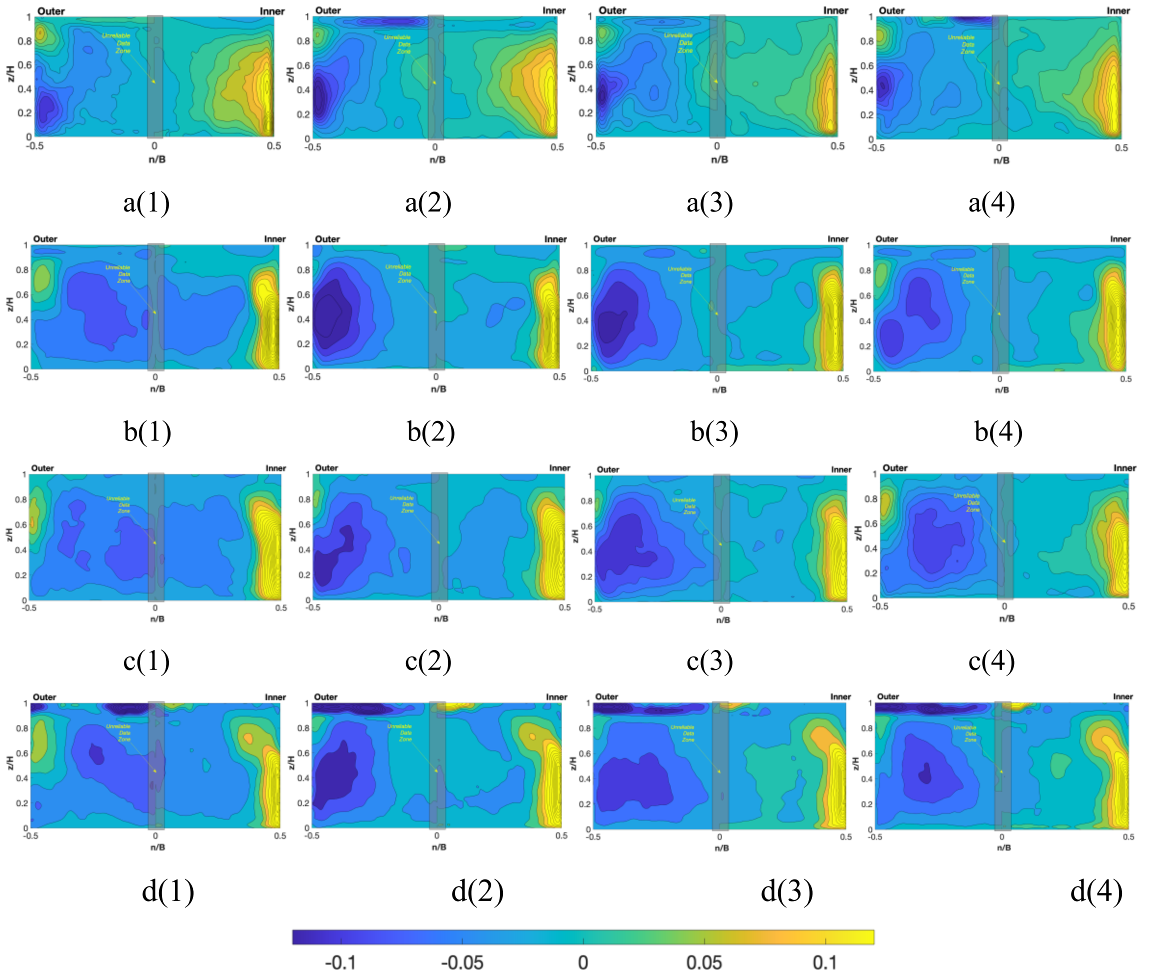

Figure 3.8 Dimensionless vertical velocity distribution at (a)37-degree (b)90-degree (c)105-degree (d)125-degree. The numbers 1, 2, 3 and 4 denote different jet conditions (1)-no jet; (2)-S=3.5; (3)-S=10; (4)-S=16.5.

A large downward velocity region at the lower outer bank is noticed in Figure 3.8a(1), but it disappears as the flow continues in the bend (Figure 3.8b(1), 3.8c(1) and 3.8d(1)). When there are negatively buoyant jets present, this region persists throughout the bend. This agrees well with the variation of the maximum vertical velocity (Figure 3.5c), i.e., at the beginning of the bend, the maximum velocity with dense jets is larger than that of the one without jets. Furthermore, as shown in Figure 3.8a, the core of this downward velocity region is slightly lifted as the salinity increases. The same as the influence on streamwise velocity caused by the jets in the outer bank, this phenomenon is only observed at 37-degrees. For the rest of the measured cross-sections, the core of the high downward velocity region was attenuated with increasing salinity (Figures 3.8b(2), 3.8b(3) and 3.8b(4)). This attenuation was found to roughly continue through the bend at 105-degrees and 125- degrees. As presented in Figure 3.8, at the outer bank, immediately below the water surface, an opposite upward velocity region was also found. The same as the trend of the transverse velocity, a gradual decrease of the size of this specific region was observed, followed by an increase with the rising of jet salinity.

3.3.3 Secondary flow

For most of the measured cases, typical vortices of bend flows, such as the outer bank cell and the main center cell are visible in the experiments, and the separation zone at the inner bank is captured at certain degrees. Specifically, they are the large primary secondary flow also known as the center region cell located in the lower center of the channel and a counter-rotating small cell that normally can be found at the outer bank below the water's surface. Such results have been observed in previous studies (ROZOVSKII,1957; BLANCKAERT AND DE VRIEND, 2004; OLIVER ET AL.,2013). The primary center-region cell has been known to be the result of the local imbalance between the centrifugal force and the cross-stream pressure gradient, and turbulence has little contribution to generating the center region cell. Unlike the center region cell, turbulence plays an important role in the formation of the outer bank cell, but it is not the exclusive reason. Vortex skewing, which results from centrifugal force, is also conducive to the outer bank cell (BLANCKAERT AND DE VRIEND, 2004). At cross-sections of 90°, 105°, and 125°, the core of the center region cell in each plane shifts to the inner bank compared to the 37°, and it stays at the inner bank until it exits the bend. This result is also found to be consistent with existing research results (BLANCKAERT AND GRAF, 2001; ABHARI ET AL., 2010; BAI ET AL., 2019).

To better understand the influence of negatively buoyant jets, the sizes and vorticities of the secondary flow are calculated using an online open-source code called IDvortex (ENDRIKAT, 2022) developed in MATLAB. Figure 3.9 shows both the outer bank cell and the center region cell variation with the presence of the jets. The evolution of the center region cell is consistent for cases in which the salinity values were 3.5 and 10, e.g., the size of the center region cell experienced a decreasing trend, following with an increase and another decrease as flow proceeded in the bend. However, as for the densest jet case, at the beginning of the bend, the size of the center region cell would continue increasing, and the same trend can be obtained for the no jet case (Figure 3.9a). According to the plots, the maximum difference between the cases with and without the jet was found at the 37-degree which located at the beginning of the bend. Moreover, the difference of the center region cell size between the first and the last cross-sectional plane measured in the bend decreases as the salinity increases. On the contrary, the variation of the outer bank cell size with the salinity had an opposite trend. Meanwhile, it is obvious that the size of the outer bank cell was de-creased with the presence of the negatively buoyant jets. However, it is important to note that, when the flow approached the exit of the bend, the size of the outer bank cell with the jets maintained a descending trend rather than a rising tendency (Figure 3.9b). Analogously, the strength of the outer bank cell with the occurrence of the jets was lower than the one without the jets, while the evolution for both the size and the intensity of the center region cell with the jets shows more variation (Figure 3.9a and 3.9c). The reason behind the variation might be the different driving mechanisms for the generation of these two types of cells. The center region cell is regarded to result from centrifugal force rather than turbulence; hence, the jet-induced turbulence cannot be applied directly to it. The effects on the center region cell could be attributed to the transport of the jet-induced momentum, and the mixing behavior itself also influences the momentum distribution in the bend. Consequently, this process deforms the downstream velocity profile, which changes the centrifugal force. As for the outer bank cell, although few examinations have been revealed for the underlying mechanisms, the hypothesis that the outer-bank cell is formed by the combined exertion of the centrifugal force and turbulence has been widely accepted (BLANCKAERT AND GRAF, 2001). Therefore, the presence of turbulent jets can act directly on the turbulence in the bend flow. However, the reduction of the size and strength of the outer bank cell indicates that the jets incurred additional turbulence stress, which favors the dissipation of the outer bank vorticity.

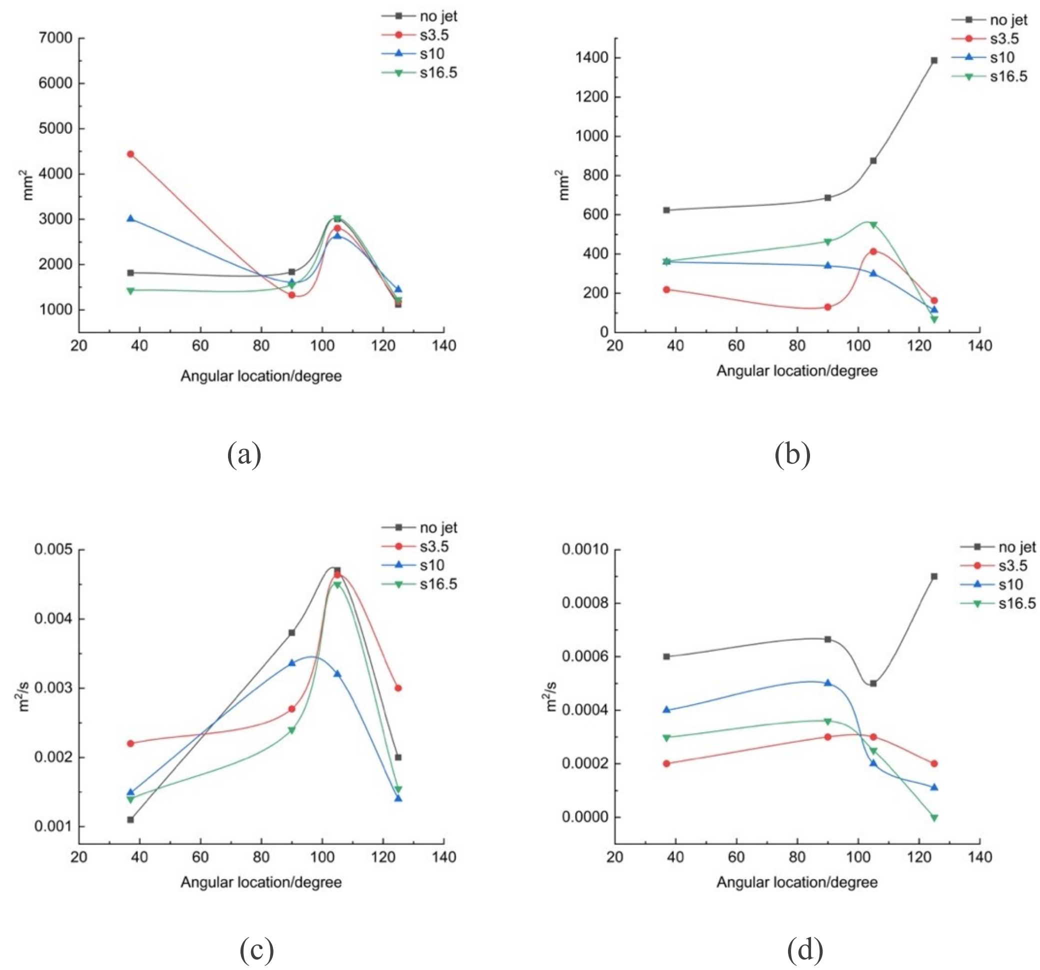

Figure 3.9 Secondary flow properties evolution with respect to jet salinity in the bend (a) center region cell size (b) outer bank cell size (c) center region cell vorticity (d) outer bank cell vorticity

3.4 Conclusions

The present study examined mixing of a negatively buoyant effluent jet in a 135-degree open channel bend. High-quality three-dimensional velocities were measured throughout four channel cross-sections using a stereo-PIV system. The experiments were designed to investigate the influences on the 3D flow field caused by the negatively buoyant jet in the bend flow. Jets with three different salinities were investigated, as well as a case without a jet. The observations focused on the streamwise and cross-stream velocity distribution, the maximum velocity, and the secondary flow properties. The main conclusions may be summarized as follows:

- Multiple flow patterns were captured in different bend cross-sections, i.e., the curvature-induced helical flow, the outer bank counter-rotating cell, and the inner bank separation zone.
- The negatively buoyant jets have little impact on the maximum streamwise velocities and the depth-averaged streamwise velocities; however, the maximum transverse and vertical velocity of the flow varies with salinity.
- The influence of the jets on the center region cell vorticity were mostly at the beginning and exit of the bend, where the mixing process started and developed, respectively. It can be attributed to the sudden change of flow complexity near the entry and exit of the bend. The failure to obtain a continuous variation on the secondary flow with respect to the increase of salinity is due to the distinctive transport and mixing behavior of the dense jets in a bend.
- The jet-induced turbulence stress favors the dissipation of the outer bank vorticity, although at different cross-sections this attenuation varies

3.A Appendix

3A.1 flow configuration in the straight reach

A common criterion for considering open-channel flow to be fully turbulent (Chin 2006) and the criterion used in this paper is $\frac{u_* k_{s,\,\mathrm{bed}}}{\nu} > 70$, where ν = kinematic viscosity; $k_{s,\,\mathrm{bed}}$ =representative height of the bed material; and u_*= shear velocity (for our case, this value was 25). As for boundary layer development, according to Kirkgöz and Ardiçhoğlu (1997), they performed experiments aimed at identifying Lδ (boundary layer development length) for turbulent, subcritical, and uniform flow in a smooth channel (1.5 ⩽ B=H ⩽ 12.0). For predicting Lδ they proposed $\frac{L_\delta}{H} = 76 + 0.0001\frac{\mathrm{R}}{\mathrm{F}}$. For the present study, smooth boundary layer development takes at least 76 flow depths for a uniform flow. The straight inlet section was 2 m long, therefore, it is possible and perhaps even likely that the flow was not fully developed before reaching the bend. However, this issue had been discussed when setting up the experiment. The reason we decided to use a deeper flow because we need to add a jet in the flow. Nonetheless, from Figure 4.2a the lowest streamwise velocity was near the bed at the 37deg cross-section, there is a reasonable vertical gradient of velocity, and the flow field appears to be dominated by the influence of the bend. As such, even if not fully developed at the entrance, the study design reasonably enables evaluation of the mixing of an effluent jet in a bend flow.

3A.2 vortex identification with MATLAB

This code has been developed based on the paper cited below. The proper orthogonal decomposition (POD) is used to separate turbulent fluctuations and an unsteady swirling motion, so that each contribution to the total energy can be evaluated. It contains two vortex identification functions, Γ_1 and Γ_2, which identify the locations of the center and boundary of the vortex based on the velocity field respectively. Then, by locating the boundary of the cell, the size and the strength of the circulation can be calculated. The structure of the velocity field, and not its amplitude, is what these functions use to characterize the center and edge of the large-scale vortex. In addition, both Γ_1 and Γ_2, are robust enough to process huge data sets consisting of several thousands of velocity vectors while eliminating the small-scale turbulent intermittency.

The procedure to use the code can be divided into three steps. First, import data from the PIV measurements and extract the velocity vectors that are needed in the vortex calculation. Second, perform coordinate transformation and data interpolation based on the grid that can be operated in the calculation of the identification functions. Third, plot the velocity field with the found vortex center. The following figure shows the documents needed for running the vortex identifying code.

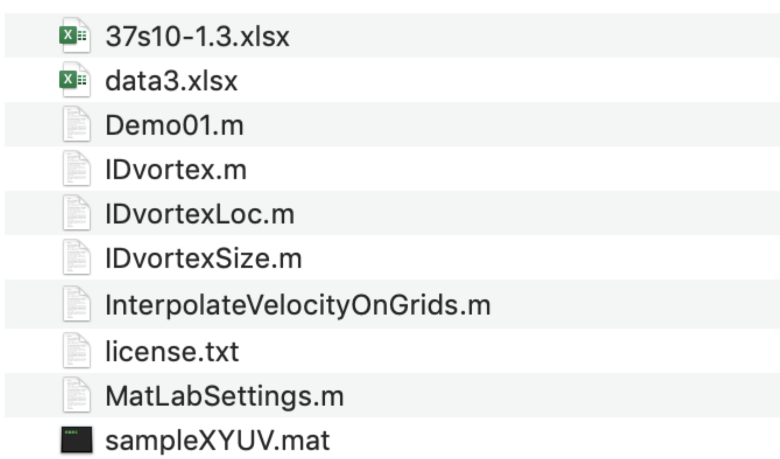

Figure 3A.1 configuration of the IDvortex code.

3A.3 Velocity concentration at the inner bank

In the present study it was observed that maximum velocity was near the inner bank at the bend entrance. This is often observed in sharp bends (E.G., KASHYAP ET AL. 2012). Figures 3A.2 and 3A.3 showed examples of previous experimental results demonstrating flow concentration on the inside bend as it entered the bend.

As for the first case presented in Figure 3A.2, the channel was of rectangular cross section 0.6 m width, 0.7 m height with 1.8 m radius of bend to centerline, and the flow depth is 0.2m. The aspect ratio was 3 (ABHARI ET AL, 2010).

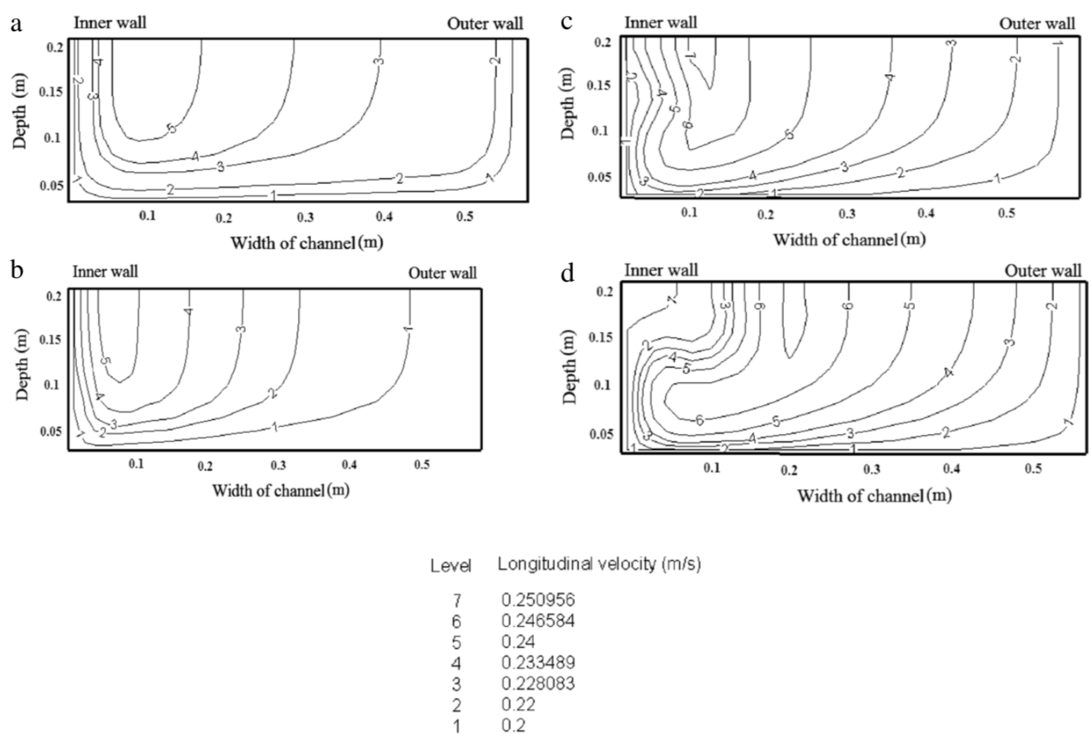

Figure 3A.2. Contours of longitudinal velocity at different sections: (a) 0°, (b) 30°, (c) 60° and (d) 90° (FROM ABHARI, M. NAJI, ET AL. "EXPERIMENTAL AND NUMERICAL SIMULATION OF FLOW IN A 90 BEND." FLOW MEASUREMENT AND INSTRUMENTATION21.3 (2010): 292-298.)

The numerical models (as shown in Figure 3A.3) were validated with experimental data that were collected using a channel with a rectangular cross-section and a width-to-depth ratio of B/H=2.9. The flume was fabricated from Lucite, hence, channel bed and side walls can be considered smooth.

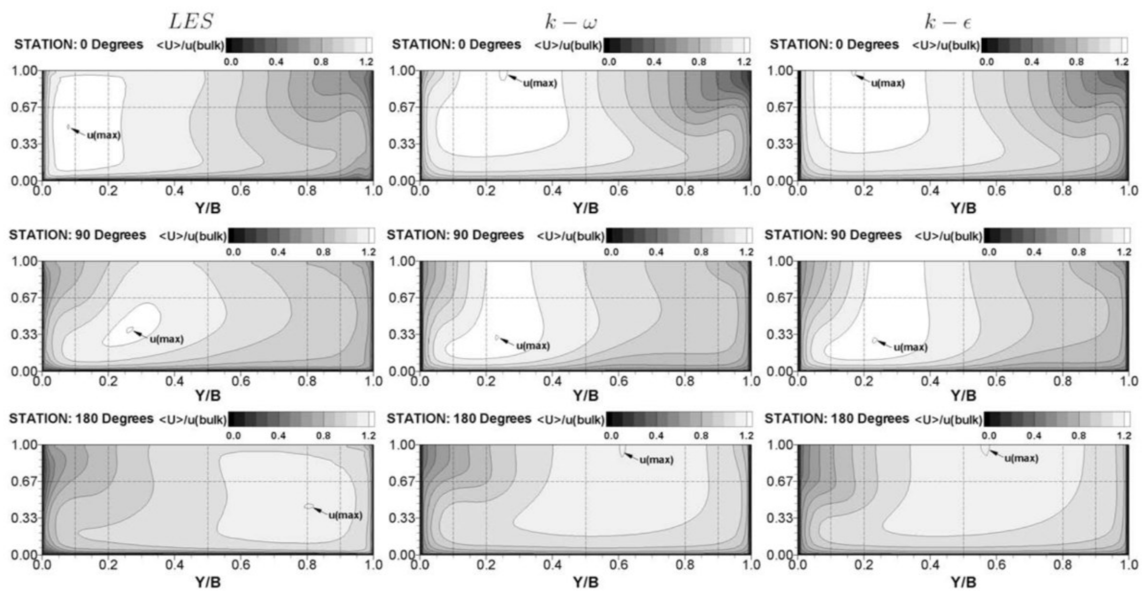

Figure 3A.3 Contours of the primary flow (left column – LES, middle column –k-ω, right column – k-ϵ) at the entrance (0°, top row), halfway through (90°, middle) and at the exit (180°, bottom row) of the bend. (From Stoesser, Thorsten, Nils Ruether, and Nils Reidar Boe Olsen. "Calculation of primary and secondary flow and boundary shear stresses in a meandering channel." Advances in Water Resources 33.2 (2010): 158-170.)

In a word, it is a common phenomenon that max velocity can be found concentrated at the inside of the bend entrance in sharp bends.

3A.4 Data uncertainty analysis.

Peak-locking is a serious bias error source in particle image velocimetry (PIV), and peak-locking will occur when the size of the diffraction-limited particle images on the sensor become too small, resulting in under-sampled particle images. Other forms of peak-locking originate from poor correlation-peak interpolation or inadequate PIV methods. As for the current case, the field of view is 100 mm*100 mm, and the images are subdivided into rectangular interrogation windows of size 26·20 pixels (width height) in the image. However, it should be acknowledged that the likelihood of the presence of peak-locking was not evaluated in the present measurements. Nevertheless, it has been reported that the mean velocity profile not that sensitive to the peak locking effect. Besides, it has been noticed that it is important to make sure that the displacements associated with the turbulent fluctuations are greater than 1 pixel in magnitude if peak locking cannot be entirely suppressed (Christensen, 2004). In our case, the turbulent fluctuations were obviously greater than 1 pixel. Therefore, the absence of the peak-locking checking might have moderate influence on the experimental results.

As for the PIV error analysis, an uncertainty of the all three velocity components had been calculated, which was based on a statistical analysis of the contributes of each pixel to the cross-correlation peak shape. The uncertainty data of the displacement vector were generated and stored with the vector (Figure 3A.4).

Thought the unreliable data has not been removed directly from the plots, indeed, we did not use data from those regions in the data analysis. Specifically, regions located at the edge of each measurement were not considered since high level of distortion and reflection could be found there. For example, according to the uncertainty calculation, in Figure 3A.4 (a), high level of uncertainty can be found close to (-40, 40) (based on the coordinates in the measurement), which was the water surface. The high intensity reflection of the laser light caused the high uncertainty at the corresponding area. Therefore, data collected from 1-2cm below the flow surface and 1cm from the wall were considered as unreliable, which would not be used in the subsequent data analysis. Moreover, we have also marked out the regions when combining two measured planes into a single cross-sectional plane, but this is because while moving the calibration plate, there must be some inaccuracies in lining up the two planes.

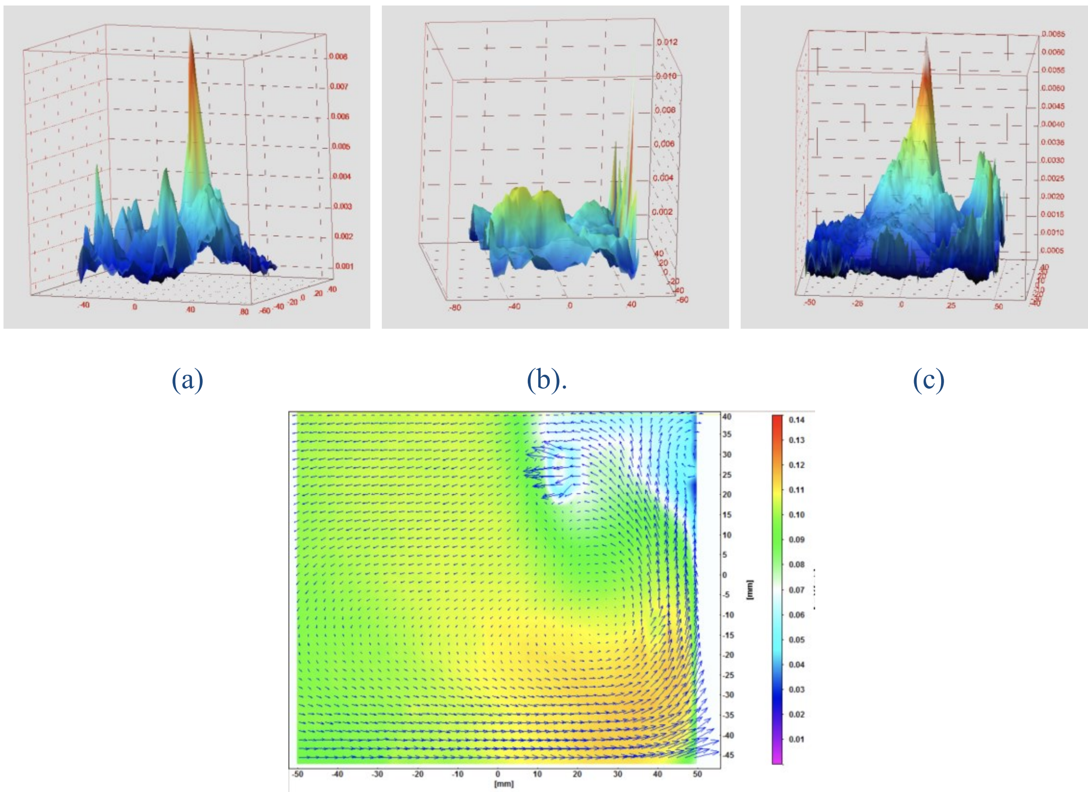

(a) (b). (c)

(d)

Figure 3A.4 Sample pictures of uncertainty analysis result (a) 37-degree at the outer bank side with (no jet condition); (b) 37-degree at the inner bank side with (no jet condition); (c) 105-degree at the inner bank side with (no jet condition); (d) velocity distribution at 105-degree inner side measurement plane exported from DaVis (m/s). (the unit of the velocity difference in the uncertainty calculation is m/s ; the x and y axis represents the coordinates of the mapped measurement planes, x is the direction via width of the measured plane and y is the direction via depth, the z axis in figure (a) (b)and (c) indicates the uncertainty value of the corresponding vector field; the origin of the coordinates locates at the center of the measured plane)

As for the plots presenting, figures were plotted upstream because this was how the measurements were collected in the experiment, particularly, we were taking the pictures from the downstream direction. Therefore, all the section plots are shown facing upstream in the entire analysis process.

Chapter 4 Investigation of the secondary flow structures in channel bends with negatively buoyant jets

Abstract: Flow structures in open channel bends with cross-stream circulation, such as the primary central cell and counter-rotating outer bank cell, are important for momentum transfer, mixing, and river evolution. In the present study, experiments were conducted for certain densities of negatively buoyant jets to be discharged in a 135-degrees laboratory channel bend. Detailed experimental data were used in interpreting the large center-region cell as well as small structures in the open-channel bend. Moreover, a term-by-term analysis of the downstream vorticity equation was executed to investigate the various mechanisms underlying these cross-stream flow motions considering the influence of the negatively buoyant jets. It was found that salinity increasing hindered the effect of the centrifugal force in developing the center region cell. Turbulence stress are both the source term and the dissipative term at the outer bank cell. The cross-stream turbulent stress anisotropy distribution shows that the damping effect of the water surface is attenuated by increasing the salinity of the jet. However, at side boundary this damping effect is strengthened due to the influence of the dense jet.

Keywords: Secondary flows, Vorticity, Turbulence, Laboratory studies

4.1 Introduction

Curvature induced cross-stream circulation motions are characteristic features in curved open channel flows, which have been extensively investigated for decades. Earlier researchers assumed that the development of main flow was independent from the secondary flow, so that the influence of bends was simply treated as a perturbation by setting a parameter derived from the geometry properties of a bend (Einstein & Harder, 1954; Rozovskii, 1957; Yen and Lee, 1995; De Vriend, 1973; Engelund, 1974). With this concept, predictions could only be applied in fully developed mildly curved channels. The failure of this approach in predicting strongly curved flows reveals that the main flow would interact with the secondary flow during the redistribution process (Demuren and Rodi,1986). Except for the single large circulation (also known as the center-region cell) which is caused by the imbalance of the centrifugal force and the local pressure gradient, a smaller counter-rotating cell (called outer-bank cell) has also been observed in a number of experiments (Chang, 1971; Mosonyi & Gotz, 1973; Blackaert and Graf, 2001; Kashyap et al., 2012; Bai, 2019) and field studies (Bathurst et al., 1979).

Many theoretical and experimental studies over the past decades have been conducted to understand the underlying hydrodynamics of the cross-stream circulations, including the outer bank cell (OBC). Mosonyi & GÖtz (1973) found that the presence of the OBC related to the width-to-depth ratio (B/h), and they noticed that the cell would completely disappear with B/h over 20. Bathurst (1979) conducted experiments to evaluate the effect of the secondary circulation in river bends on the boundary shear stress. The results showed that a counter-rotating cell close to the outer bank was observed when the bank was steep and could affect the position and relative magnitude of the shear stress peaks. De Vriend (1981a) concluded that the OBC could neither only result from the centrifugal force, nor the turbulence alone. In other words, the OBC is generated from a combined effect of the centrifugal force and the hydrodynamic instability (RUSSELL AND VENNELL, 2019; LI AND ZHANG, 2022）.

Blanckaert and Graf (2001) confirmed the finding from de Vriend by evaluating different terms in the momentum equation, and they indicated that a buffer layer that prevented the outer bank from erosion was generated by the outer bank cell. By accounting for the influences of secondary flow on the downstream velocity, Blanckaert and de Vriend then reported (2004) how different mechanisms varied the secondary circulation in channel bends through the streamwise vorticity equation. For better understanding of the turbulence closure in curved channels, Blanckaert and De Vriend (2005) also analyzed the cross-stream circulation via a term-by-term assessment of the transport equation of kinetic energy and they conclude that the streamline curvature primarily generated a transversal stratification in the turbulent structure which related to a curvature-flux-Richardson number Rf. later, Blanckaert et al. (2012) investigated the flow near the outer-bank, they confirmed that the OBC mainly resulted from the reversed near-surface gradients of the streamwise velocity. By that time, consensus emerged as to the primary driving mechanisms for the center circulation cell was the imbalanced stress gradient caused by the centrifugal force and the cross-stream turbulence anisotropy highly influenced the outer-bank circulation, which has since been supported by many experimental and numerical studies (TERMINI AND PIRAINO, 2011; OTTEVANGER ET AL., 2012; CONSTANTINESCU ET AL., 2011; NJENGA ET AL.,2013; VAGHEFI ET AL, 2016). Therefore, it can be concluded that the physics of the secondary circulations are relatively well understood. The exploration into the behaviors of these circulations with the impacts caused by the variation of the flow conditions, such as the change of water depth, bank slope and flow velocity etc., however, needs further development (Blanckaert et al., 2012; Wei et al.,2016; Farhadi et al.,2018; Yan et al., 2020).

The increasing importance on the use of natural rivers for water supply, waterway navigability, waste disposal, energy production etc. has made effluent dispersion a practical problem in river management. Prediction of pollutant spreading in meandering channels is a challenging problem for engineers (Schreiner et al. 2018). Density difference between the effluent and the ambient flow further complicates the concentration distribution in the flow field. Therefore, the interactions between the ambient flow and the negatively buoyant jet are worth studying. The objective of the present study is to investigate the dependence of the secondary circulations and their generating mechanism on the density of the effluence in a bend. Three different densities of negatively buoyant jets, which typically represent the pollutant in natural rivers (Al-Salem,1987; Lai and Lee, 2012; Nadeem, 2013 and 2014), are considered in laboratory experiments. According to Roberts (1987), the ambient velocity has little impact when the coefficient $u_j/u_a F_r$ is smaller than 1 (u_j is the velocity of the jet, u_a is the ambient flow velocity, and Fr is the jet discharge densimetric Froude number, which can be defined as $Fr = u_j/\sqrt{g_o' D}$), and $g_o' = (\Delta\rho_o/\rho_a)g$, $\Delta\rho_o$ is the change of the the density, ρ_a is the density of the receivieng water). In the present study, the values of $u_j/u_a F_r$ are 19.5, 12 and 9.4 for cases with salinity of 3.5, 10 and 16.5 correspondingly. The detailed three-dimensional high-resolution velocity results throughout four cross-sections help in obtaining insights into the dynamics underlying the double-cell pattern circulation under the influence of effluent dispersion at different locations in the bend. The velocity data are time-resolved, thus in addition to the three mean velocity components, turbulence stress can also be derived from the experimental observations. Based on these results, a term-by-term analysis of the vorticity equation will be given.

4.2 Experimental setup

The detailed experimental set-up, the equipment installation, data collection and treatment procedures have been demonstrated in a separate paper (Wang et al., 2022). Therefore, only aspects of particular relevance to the present analysis will be illustrated here.

Experimental measurements were conducted in a 135-degrees laboratory bend flume connected by a 2m long straight reach as an entrance and a 0.5m long downstream straight reach. The radius of curvature at the centerline is constantly 0.2m to the inner bank of the bend. The flume was characterized by rectangular cross-sections with smooth walls and channel bed, and the width of the channel is uniformly 0.2m. At the inlet and outlet of the flume, there are two reservoirs. An adjustable volume ball valve was used to generate a particular flow in the bend, and a downstream tail gate was manipulated to regulate flow depth. The view and dimensions of the setup are presented in Fig.4.1. Four cross-sectional planes were investigated in the present study, at the 37-degree, 90-degree, 105-degree and 125-degree sections, wherein the 0-degree section was at the bend entrance. The top and cross-sectional views of the geometry of the bend and the measured cross-sections are also provided in Fig. 4.1. The flume geometry will produce non-axisymmetric flow in the bend (i.e., flow can be non-uniform with streamwise derivates unequal to zero), which is typical of natural river bends. It was not possible to measure such streamwise derivatives due to data collection along separated transects; nonetheless, as will be discussed further below, they are relatively minor and therefore not crucial for analyzing the mechanisms underlying the two types of cross-stream circulation cells (BLANCKAERT AND VRIEND, 2004).

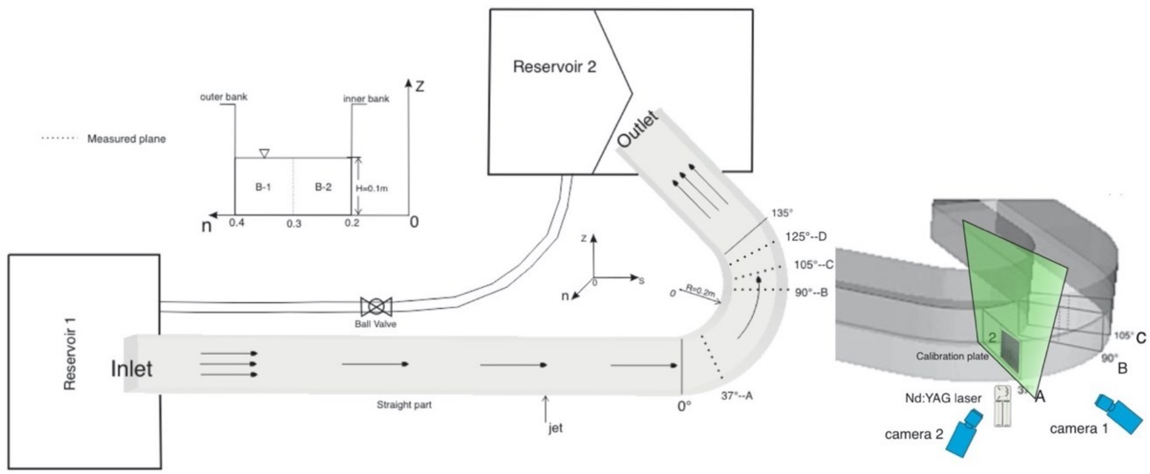

Figure 4.1 Sketch of the bend flume and the coordinate system with the flow condition in the flume.

The 3D flow velocity fields of all the four cross-sections were measured using a Particle Image Velocimetry (PIV) system with a sampling frequency of 30 Hz. Specifically, a stereo-PIV technique was applied in the present study, thus instantaneous three component velocities were measured throughout a 2D interrogation plane. Each measured plane was subdivided into 44 (width) by 22 (depth) interrogation windows in average for the present cases. It was expected that flow structures at each cross section would be completely resolved within this measuring grid. The laser was fixed on a movable cart under the flume, and two cameras were set on the same elevation of the flume with a certain angle in between. The camera angles used for each plane were determined by trial and error until an acceptable calibration value was obtained. A 10 cm by 10 cm calibration target was utilized, thus each measurement yielded a 10 cm by 10 cm surface, which was half the size of a flume cross-section. To obtain a full plane of one cross-section, the calibration plate was first placed at the outer side then moved to the inner side. After two sets of measurements, the entire cross section was covered for an investigated plane. The post-processing was completed by using the software DaVis, with which both the mean-velocity components and the instantaneous components can be derived. The measuring sections and the stereo-PIV configuration are shown in Fig. 1 on the right.

The hydraulic conditions of the measured runs are presented in Table 1. According to value of the curvature ratio (bend radius/channel width, Rc/B=1.5, Rc is the radius of the centerline curvature, B is the width of the channel), the current study concerns a strongly curved open channel (Kashyap et al., 2013). The water depth was kept constant at 10cm; therefore, the flume is much narrower than typical natural river bends since the aspect ratio (channel width/flow depth, B/H=2, H is the water depth) is 2. The water depth in this study is considered as a deep channel to avoid the boundary effect caused by discharging the negatively buoyant jets. It also can be treated as a representative of the deeper part of natural river bends with wide point bar. Moreover, small width-to-depth ratio flow tends to generate stronger OBC and bed shear stress (Termini and Piraino, 2010; Kashyap et al., 2012). For all the runs, the flow velocity in the main channel (U_m) was set to 0.1m/s. From the measured data of the three instantaneous velocity components, the derived mean velocity components can be denoted as v_s, v_n and v_z, representing the velocity in the streamwise, transversal and vertical direction respectively, and the fluctuating velocity components will be v_s', v_n' and v_z'.

Table 4.1 Hydraulic characteristics of main flow in bend

B (m)	H (m)	R (m)	Q (L/s)	g (ms^{-2})	U_m (m/s)	Re	Fr
0.2	0.1	0.3	2	9.8	0.1	22024	0.22

B is the flume width, H is the flow depth, *R* is the centerline curvature radius to the centerline, Q is the mean flow discharge. g is the gravitational acceleration; the Reynolds number is calculated by $Re = U_m H/\nu$; the Froude number is defined by $Fr = U_m/(gH)^{1/2}$.

The source of the negatively buoyant jets used in this paper was a dilute solution of 100% lab sodium chloride, and they were discharged perpendicular to the main flow within the upstream straight section at a distance of 55 cm away from the bend entry. The nozzle was submerged horizontally at an elevation of 4.5 cm above the flume bed, and the nozzle diameter was 0.95 cm. To maintain a constant jet flow rate, the jet was conveyed by a plastic tube from a constant-head tank and controlled by a small ball valve. Hence, a jet-in-crossflow condition was considered herein. The jet discharging velocity was kept at 0.2m/s for all cases, only the density of the jet changed between experimental runs. Experiments with three different jet densities (salinity of 3.5, 10 and 16.5) were performed and then evaluated to interpret the influence of the jets on the secondary flow.

4.3 Theoretical considerations

The theoretical framework for this analysis of the cross-stream circulation is based on the mean vorticity equation, which is one of the most conceptual approaches in the investigation of secondary flows (NIKORA AND ROY, 2012). Einstein and Li (1958) first proposed a method to evaluate the secondary flow in straight channels by involving the mean vorticity equation. The vorticity equations are derived from the Navier-Stokes equations and can directly specify information about the production and dissipation of the secondary currents. Therefore, the use of vorticity equation makes it possible to examine the conditions under which the dynamics of the cross-stream motions can be clearly explained.

The vorticity equations adopted in the present paper are based on a curvilinear coordinate system that has already been extensively used, especially for research related to curved channels. That is, the three velocity components (s, n and z) represent the streamwise, transverse and the vertical directions respectively. The transformation of the governing equations from a Cartesian to a cylindrical coordinate system can be found in Batchelor (1970). The vorticity equation is obtained by taking the curl of the transverse momentum equation in the corresponding direction. The streamwise component of the vorticity vector (ω_s) is defined as:

$$\omega_s = \frac{\partial v_z}{\partial n} - \frac{\partial v_n}{\partial z} \tag{4.1}$$

The cross-stream motions which are dominated by the transverse and vertical momentum can be represented by the streamwise vorticity. Blanckaert and De Vriend (2004) gave the streamwise vorticity equation as:

$$\frac{\partial \omega_s}{\partial t} = -\left(\frac{1}{1+n/R} v_s \frac{\partial \omega_s}{\partial s} + v_n \frac{\partial \omega_s}{\partial n} + v_z \frac{\partial \omega_s}{\partial z}\right). + \frac{1}{1+n/R} \omega_s \frac{\partial v_s}{\partial s}$$
$$+ \left[\omega_n \frac{\partial v_s}{\partial n} + \omega_z \frac{\partial v_s}{\partial z} + \frac{1}{1+n/R} \frac{v_n \omega_s}{R} - \frac{1}{1+n/R} \frac{v_s \omega_n}{R}\right]$$
$$- \frac{1}{1+n/R} \frac{\partial}{\partial z}\left(\frac{\overline{v_s'^2}}{R}\right) + \frac{\partial^2}{\partial z \partial n}\left(\overline{v_n'^2} - \overline{v_z'^2}\right) + \frac{1}{1+n/R} \frac{1}{R}\left(\frac{\partial \overline{v_n'^2}}{\partial_z}\right)$$
$$+ \left\{\frac{1}{1+n/R} \frac{\partial^2}{\partial z^2} - \frac{\partial}{\partial n}\left(\frac{1}{1+n/R} \frac{\partial}{\partial n}\right)\right\} [(1+n/R)\, \overline{v_n' v_z'})$$
$$+ \frac{\partial}{\partial z}\left(\frac{1}{1+n/R} \frac{\partial \overline{v_s' v_n'}}{\partial s}\right) - \frac{\partial}{\partial n}\left(\frac{1}{1+n/R} \frac{\partial \overline{v_s' v_z'}}{\partial s}\right)$$
$$+\nu\left(\nabla^2 \omega_s + \frac{2}{(1+n/R)^2} \frac{1}{R} \frac{\partial \omega_n}{\partial s} - \frac{1}{(1+n/R)^2} \frac{1}{R^2} \omega_s\right) \tag{4.2}$$

Where the n- and z-components of the vorticity are expressed as follows:

$$\omega_n = \frac{\partial v_s}{\partial z} - \frac{1}{1+n/R} \frac{\partial v_z}{\partial s} \tag{4.3}$$

$$\omega_z = \frac{1}{1+n/R} \frac{\partial v_n}{\partial s} - \frac{\partial v_s}{\partial n} - \frac{1}{1+n/R} \frac{v_s}{\partial s} \tag{4.4}$$

The mechanisms of vorticity generation in the equation as interpreted by Blanckaert and De Vriend (2004) are reiterated here:

(1) The terms $v_n \partial \omega_s / \partial n + v_z \partial \omega_s / \partial z$ in the first line represent advection of streamwise vorticity due to cross-stream motion (v_n , v_z); in other words, the streamwise vorticity is redistributed by the advective secondary transport process.

(2) The last term ($\omega_s \partial v_s / \partial s$) in the first line describes amplification of the streamwise vorticity by vortex stretching.

(3) The second line terms within the square brackets demonstrate the redistribution of the existing mean vorticity ($\omega_s, \omega_n, \omega_z$) caused by skewing or vortex stretching. This is an inviscid process, and such vorticity (also known as Prandtl's first kind of secondary flow) will be dissipated by the turbulence and viscosity effect (BRADSHAW, 1987). By substituting equation (4.1) and (4.3 and 4.4), these terms can also be written as:

$$-\frac{1}{1+n/R}\frac{\partial}{\partial_z}\frac{{v_s}^2}{R}+\frac{1}{1+n/R}\frac{v_n\omega_s}{R}+\left[\frac{1}{1+n/R}\frac{\partial v_n}{\partial_s}\frac{\partial v_s}{\partial_z}-\frac{\partial v_z}{\partial_s}\frac{\partial}{\partial_n}\left(\frac{1}{1+n/R}v_s\right)\right] \quad (4.5)$$

In which, the interaction between the downstream velocity and the vorticity is taken into account by the ∂/∂_s related terms in the square brackets of equation (4.5). It can be found that the centrifugal force ($-{v_s}^2/R$) plays an important role in forming the skew-induced vorticity. The last term in the second line is also a centrifugal associated term but related to the turbulence.

(4) Terms in the third and fourth lines are about turbulence stress components in the lateral direction. Different from the diffusion of skew-induced vorticity due to turbulence, this Prandtl's second kind of secondary flow can actually be generated by the turbulent stress in certain regions.

(5) The fifth line of equation (4.2), and the ∂/∂_s term in the first line, represent the influence of non-uniformity of flow in the downstream direction along the channel. These terms cannot be evaluated in the present case because data were collected at individual sections, but these terms are relatively small.

(6) The last line specifies dissipation by the molecular viscosity, which is considered to be inconsequential in turbulent open channel problems.

In the following, the center-region cell and the outer bank in experimental channel bend cases with and without a negatively buoyant effluent jet are presented. The generation mechanisms underlying these cells are then analyzed by evaluating individual terms in the streamwise vorticity equation.

4.4 Results

4.4.1 Patterns of mean flow quantities without jets

Three cross-sections (37º, 90º, and 105º) that reflect the beginning, the middle part, and the end of the bend correspondingly, were chosen for in-depth analysis. The vectorial distribution of the measured mean transverse velocity fields (v_n, v_z) and the mean streamwise velocity (v_s) over the selected cross-sections without the negatively buoyant jets are shown in Figure 2 (For cases with the jets, see paper WANG ET AL., 2022). Note that each presented velocity was normalized by the mean flow velocity U_m. As can be seen, the secondary flow exhibits a bicellular pattern, and the two cells have the opposite sense of rotation (Figure 4.2). As for the velocity distribution, the core of high velocity flow was concentrated at the inner bank at the beginning of the bend, and then slowly shifted to the outer bank side due to the momentum transport (BLANCKAERT AND GRAF, 2004). Specifically, the high velocity core (the yellow zone) gradually spreads out from the inner bank to the centerline and moves close to the bottom when it approaches the bend exit. In the area between the outer bank cell and the center region cell, also known as the buffer layer, an attenuation can be found with the streamwise velocity. It has been reported that this layer provides a protective effect for the outer bank from the erosion process (Blanckaert and Graf, 2004). This finding conformed to Rovovikii's conclusion (1957) that erosion most susceptibly occurs in the concave bank near the bend exit (Bai, 2019). In the meantime, the center region cell develops, and the cell center slightly deviates upward towards the inner boundary with the circulation vectors increasing through the bend. These results are consistent with previous experiments results, e.g., de Vriend (1981), Gholami et al. (2014), Farhadi et al. (2018), Bai et al. (2019).

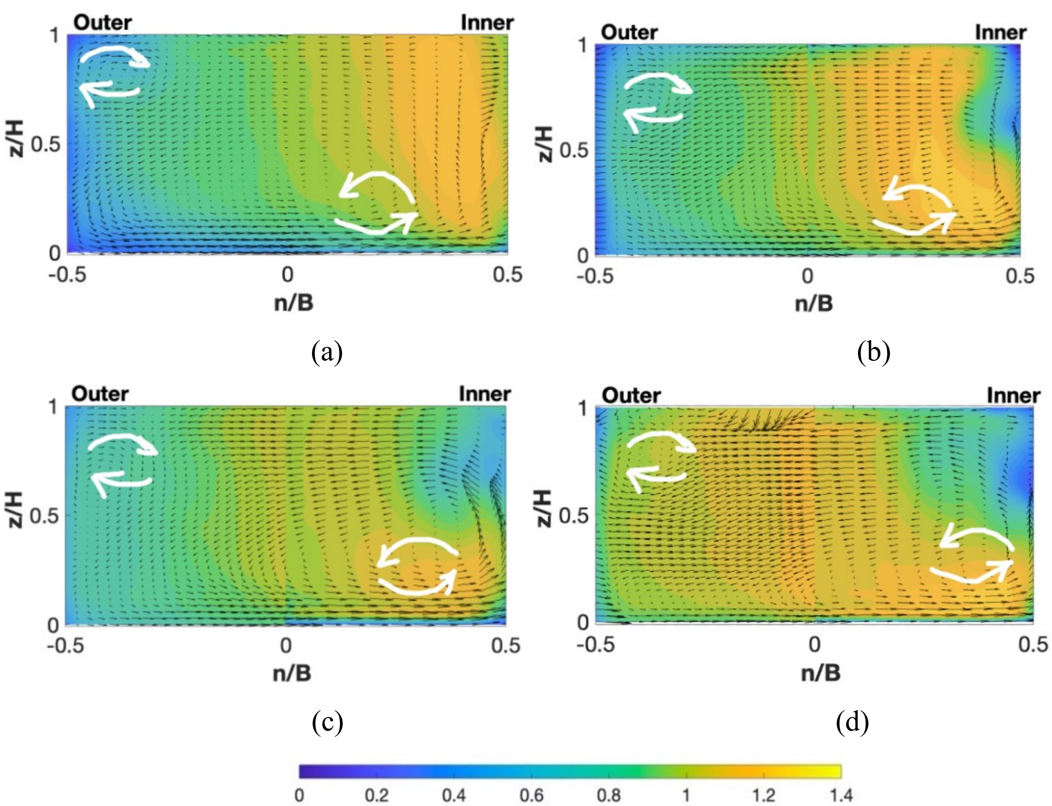

Figure 4.2 Vectors of the normalized velocity components in the cross-stream direction and the contour of the normalized streamwise velocity, (a) 37º, (b) 90º, (c) 105º, (d)125 º. The white circular arrows indicate the approximate location of the outer bank cell and the center region cell respectively.

Figure 4.3 shows the normalized vectors of the cross-stream velocity components and streamwise vorticity $\omega_s H/U$ (Eq. (4.1), U is the velocity of the mail flow and H is the water depth) in four cross-sections of the bend without the negatively buoyant jet. All the gradient calculations were made with MATLAB. On the outer half of the bend, the streamwise vorticities are positive in the center-region cell area and negative in the outer-bank cell, indicating that the two circulations rotate in opposite directions. The red line in Figure 4.3 denotes the contour line at which the vorticity is 0 ($\omega_s = 0$). The maximum vorticity can be found approximately at the 'eye' of the outer bank cell, and it decreases as it spreads towards the $\omega_s = 0$ contour line. This was also observed by Blanckaert and De Vriend (2004) and Farhadi et al. (2018). As secondary flow develops through the bend, it can be found that the vorticity at the OBC is attenuating and the core of the high vorticity area is shrinking (cf. van Balen et al. 2010, Kashyap et al. 2012); however, vorticity reaches its smallest maximum (in absolute value) at 105-degree, then it increases when the flow approaches the bend exit. This unexpected observed increase in OBC vorticity near the bend exit may have been experimental error; measurements of the OBC at additional sections may have helped confirm this error.

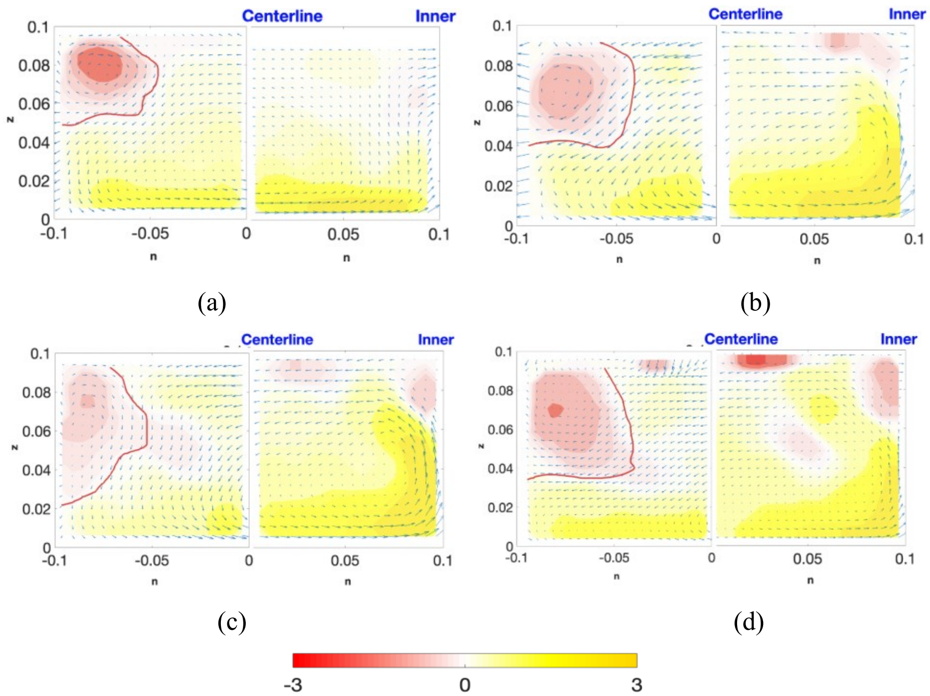

Figure 4.3 Normalized streamwise vorticity of a cross-section at different angular location without the jets. (a) 37º, (b) 90º, (c) 105º, (d) 125º.

Figure 4.3 also illustrates the distributions of the normalized streamwise vorticity in the inner bank half as the flow proceeds through the bend (the right part of each figure). It is obvious that a large area of the investigated cross-sectional plane in the bend is characterized by the center-region cell (see paper WANG ET AL., 2022). In the present study, for all the measured cross-sections, the vorticity is increasing from the water surface towards the bed, and it reaches the maximum value ($\omega_s H/U \approx 3$) near the bed. It can also be seen that the core of the high streamwise vorticity is located at the inner corner near the flume bed, and the size of the encircled high vorticity core increases when the flow is approaching the bend apex and then starts decreasing near the bend exit. Similar results have been reported by van Balen et al., (2010) and Kashyap et al., (2012). At the inner boundary under the water surface, zones of reversed vorticity can be observed. It can be induced that the reversal vorticity results from flow separation, which is a characteristic at the convex bank of a bend (BLANCKAERT, 2015). As the flow proceeds, this separation zone develops and expands.

4.4.2 Secondary flow with negatively buoyant jets

The properties of the streamwise vorticity with the occurrence of the negatively buoyant jets are illustrated in Figure 4.4, and the observed vorticity is provided in Table 2 for both the center region cell and the OBC circulations. As can be seen, the jets reduce both the size and the high vorticity cores of the OBC at 37-degrees cross-sectional planes. More specifically, at the beginning of the bend, the high vorticity core of the OBC increases with the increase of the jet salinity (Figure 4.4a). Similarly, when the flow passes the maximum curvature of the bend, the most saline jet enlarges the size of the OBC region (Figure 4.4b). Moreover, the interaction between the jets and the secondary flow enhanced the strength of the OBC. A closer comparison of the salinity 10 and salinity 16.5 cases at the 37-degree section reveals that higher salinity influences less on the core of high vorticity in the main flow but increases the intensity at the OBC region. Nonetheless, at the 105-degree section, as salinity of the jet increases the size and strength of the vorticity of the main cell is attenuated, including the high vorticity area near the bottom boundary.

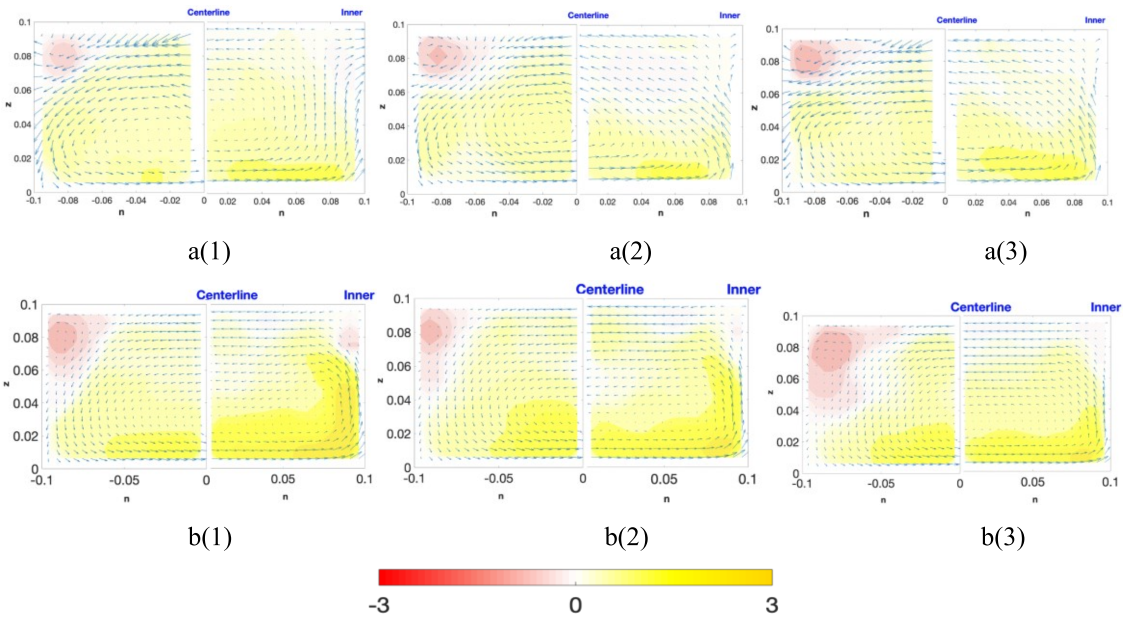

Figure 4.4 Normalized streamwise vorticity under the influence of negatively buoyant jets (1) s=3.5, (2) s=10, (3) s=16.5, a and b are at 37 and 105 degrees.

Table 4.2 Normalized mean magnitude of streamwise circulation with salinity

Vorticity	*37-degree*				*105-degree*			
	no jet	*s3.5*	*s10*	*s16.5*	*no jet*	*s3.5*	*s10*	*s16.5*
Center region cell	0.0011	0.0022	0.0014	0.0014	0.0047	0.0046	0.0031	0.0045
Outer bank cell	-0.0006	-0.0002	-0.0004	-0.0003	-0.0005	-0.0003	-0.0002	-0.0003

Figure 4.5 shows the normalized turbulent kinetic energy distribution in different cross-sections of the bend. It should be noted that the normalization was made with the shear velocity, which was estimated with the cross-section of 37-degree by using logarithmic velocity profile method. As expected, higher kinetic energy tended to form near channel walls due to shearing. Higher kinetic energy was also found in the upper outer bank region of each measured plane. The more saline jets concentrated and strengthened this higher kinetic energy at the OBC region. Also, with increase of the jet salinity, the

maximum main flow kinetic energy tended to retreat to the inner bank of the bend. This process can be more clearly seen at the 105-degree section. On the other hand, at the 37-degree section an augmentation of the kinetic energy closer to the bottom at the outer bank was detected with increasing salinity.

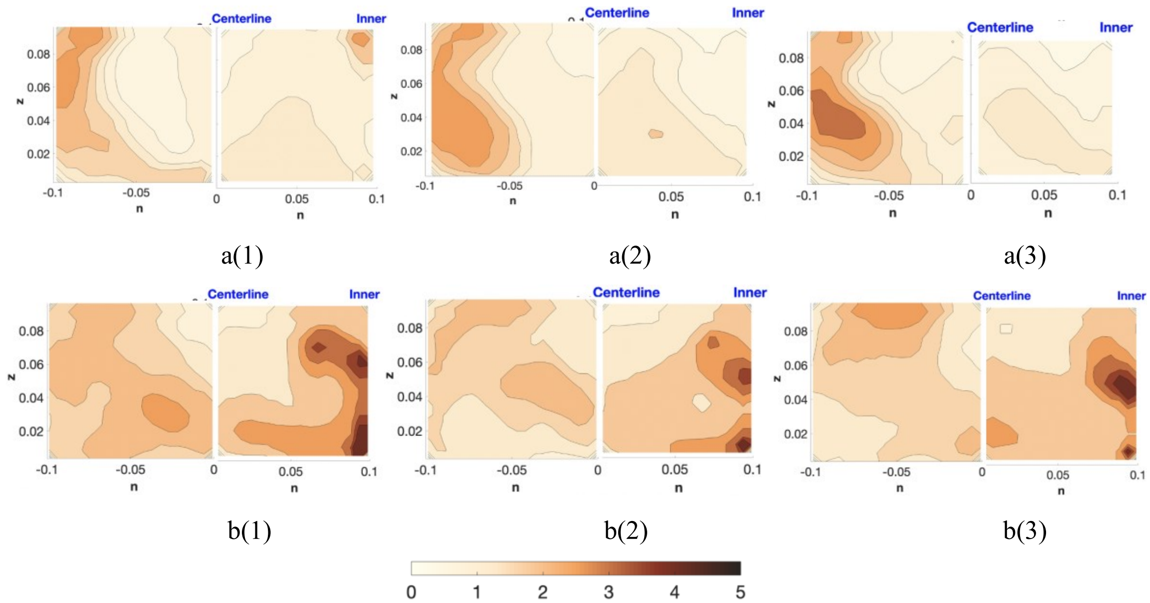

Figure 4.5 Normalized turbulent kinetic energy under the influence of negatively buoyant jets (1) s=3.5, (2) s=10, (3) s=16.5, a and b are at 37 and 105 degrees.

Along the flume, high cross-stream Reynolds stresses $-\overline{v_n' v_z'}$ were observed in the vicinity of the bed at the inner side in most cases, especially at the exit of the bend (Fig. 4.6). These patterns are similar in all cases irrespective of salinity. It also can be observed that the cross-stream Reynolds stress at 105-degree has higher magnitude compared to the stress at 37-degree. In the meantime, as salinity increases, the transverse component of the shear stress with a negative value in the center cell is moving to the inner bank side. In addition to the maximum Reynolds stress in the vicinity of the inner bank boundary at the bottom, a core of high cross-stream Reynolds stresses at the OBC region is also visible.

The signs of the shear stress in the center region and the OBC region are consistent, despite being associated with counter-rotating circulations. Furthermore, even though the center region cell covers a large part of one cross-section with much higher vortex strength, the shear stress magnitude of the eye of the center region cell is only slightly higher than that of in the outer bank region (consistent with Blanckaert and de Vriend, 2004).

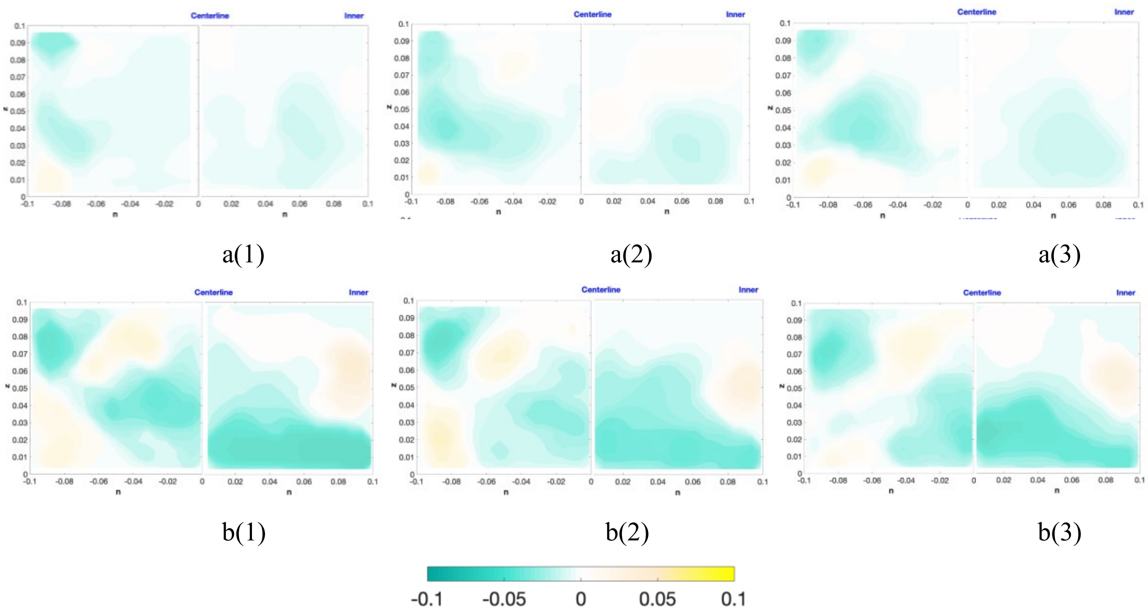

Figure 4.6 Normalized longitudinal Reynolds stress $-\overline{v_n' v_z'}/u_*^2$ under the influence of negatively buoyant jets (1) s=3.5, (2) s=10, (3) s=16.5, a and b are at 37 and 105 degrees.

The distributions of another important turbulence property $\overline{v_n'^2} - \overline{v_z'^2}$, which demonstrates the impacts of the flow boundaries, are shown in Figure 4.7. Near the water surface and the bottom, velocity fluctuations in the vertical direction are well constrained by the geometry. Consequently, there are positive values ($\overline{v_n'^2} > \overline{v_z'^2}$, and thus $\overline{v_n'^2} - \overline{v_z'^2} > 0$) within these regions. On the contrary, when it is close to the bend wall, the velocity fluctuations are confined by the side boundary, resulting in negative values ($\overline{v_n'^2} < \overline{v_z'^2}$, and thus $\overline{v_n'^2} - \overline{v_z'^2} < 0$) near the inner and outer bank of the channel. As the salinity increases, in the positive value region the transverse momentum transport increases near the water surface. This seems to be correlated with the downward movement of the main cell center with increasing jet salinity (see Figure 4.4). Meanwhile, the interface between positive and negative values ($\overline{v_n'^2} - \overline{v_z'^2} = 0$) from the upper outer bank is shown as a black dashed line in Figure 4.7. The angle of this line increases through the bend and decreases with jet salinity.

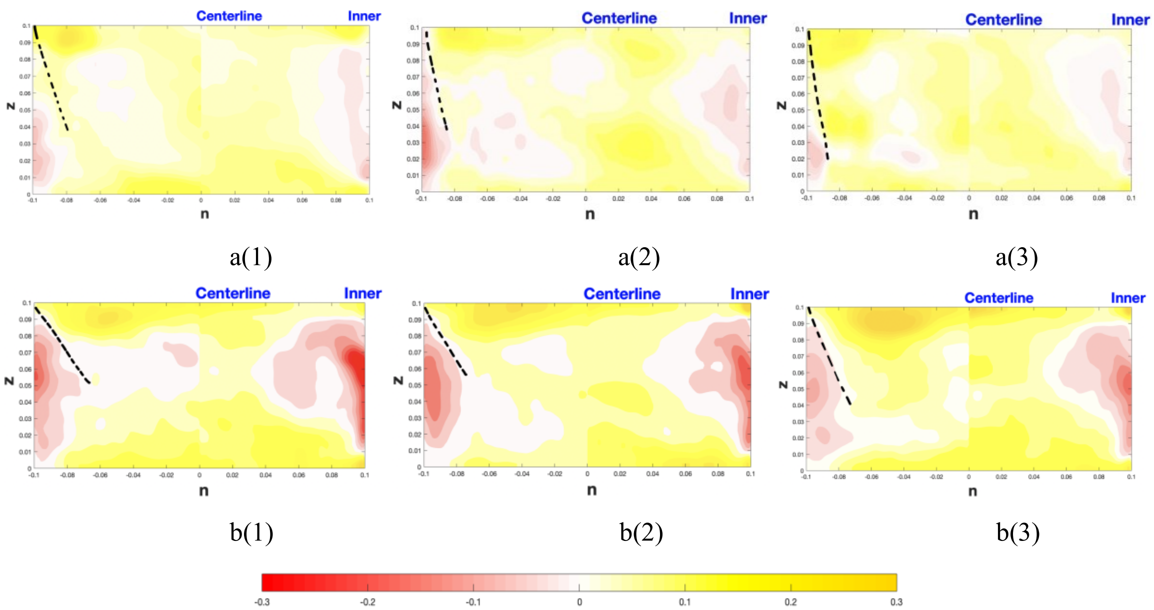

Figure 4.7 Normalized turbulent normal stress difference ($\overline{v_n'^2} - \overline{v_z'^2}$)$/u_*^2$, under the influence of negatively buoyant jets (1) s=3.5, (2) s=10, (3) s=16.5, a and b are at 37 and 105 degrees.

4.4.3 Mechanisms of the secondary flow with negatively buoyant jets

Of the four measured cross-sections, two cross-sections (37 and 105-degree) were selected for further investigations of the mechanisms underlying the circulations. Experimental data were used to calculate each term in the vorticity equation (Eq. 2). Figure 4.8 shows the normalized centrifugal term ($-\frac{1}{1+n/R}\frac{\partial}{\partial z}\left(\frac{v_s^2}{R}\right)/\frac{U^2}{H^2}$), which is often defined as the main source of the cross-stream circulation in the vorticity equation. In Figure 4.8, patches with negative values are captured in each case at the upper corner of the outer bank. The negative value of this term also proves the centrifugal force can be referred as the source of the outer bank cell which is with an opposite sense of rotation to the center-region cell. According to the direction of rotation of the two cells and the observed vorticity, each term with a negative value (same as the centrifugal term) was considered as favoring the formation of the OBC. As salinity increases, the mentioned negative value area increases in most cases, and it is more perceptible at the 105-degree cross-section (Fig. 4.8b(1-3)). With the enlarged area caused by centrifugal force under the influence of jets' salinity increase, the vortex strength of the OBC also increased. It can be deduced that higher salinity strengthens the centrifugal effect at the outer bank region. It is worth noting that there are regions with high positive values below the outer bank cells, and at the 37-degree section these positive cores concentrate as salinity increases (right half of Figure 4.8), possibly due to centrifugal effect of a more concentrated jet at the beginning of the bend. Meanwhile, the regions with positive values of the centrifugal term in the inner half shrink. This process was most discernable at the 105-degree plane, in accord with the variation of the center region cell with the jets (Table 4.2). That is, the source for the center region vorticity caused by the centrifugal force decreases as salinity increases.

Normalized values of the advective transport term ($-\left[v_n\frac{\partial \omega_s}{\partial n}+v_z\frac{\partial \omega_s}{\partial z}\right]/\frac{U^2}{H^2}$) are given in Figure 4.9. This term redistributes downstream vorticity, as opposed to generating or dissipating the vorticity. It is apparent that the advective transport term has the same order of magnitude as that of the centrifugal term. As mentioned above, the existence of positive values at the OBC region would lead to a reduction of the OBC, while negative values in the center cell region would decrease the center cell vorticity. Particularly, at 105-degree, the negative values within the lower part of the water column at the outer banks concentrate as salinity increases. Besides, the positive values at the inner bank side decrease with the increase of salinity. As a consequence, with the advective term compensating for the centrifugal term, it can be argued that the increase of jet's salinity caused the center region cell to decrease, which agrees well with the observed vorticity. Moreover, based on the observations of the turbulent kinetic energy, the maximum positive values of the advective transport terms are found to match well with the maximum turbulent kinetic energy.

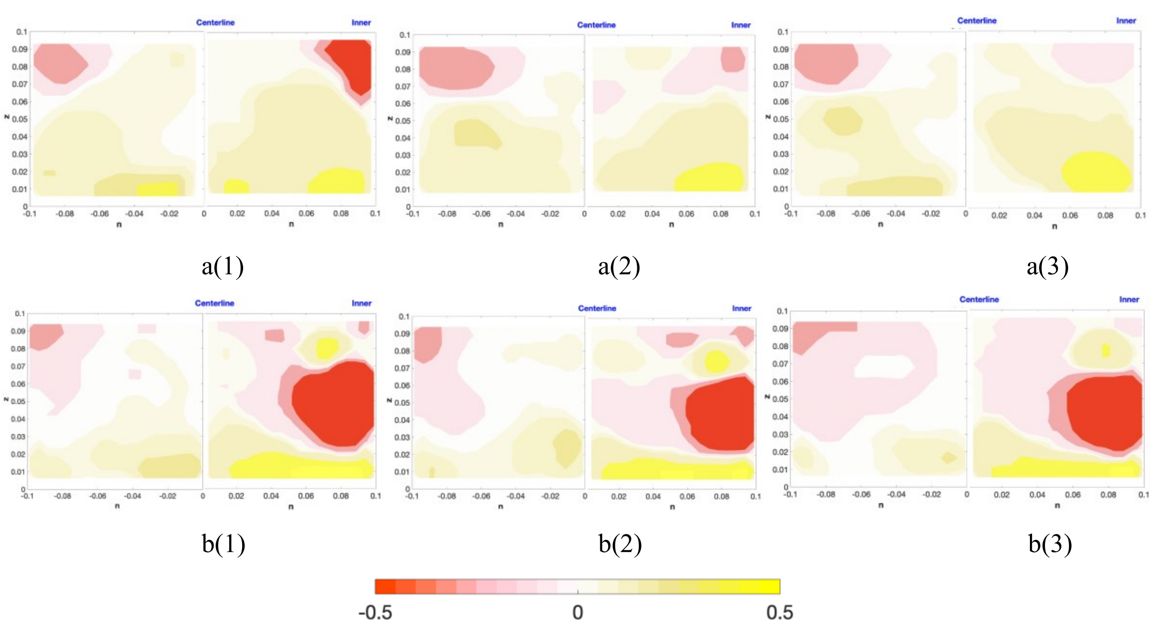

Figure 4.8 Normalized centrifugal force term of the vorticity equation with the influence of negatively buoyant jets (1) s=3.5, (2) s=10, (3) s=16.5, a and b are 37 and 105 degrees respectively.

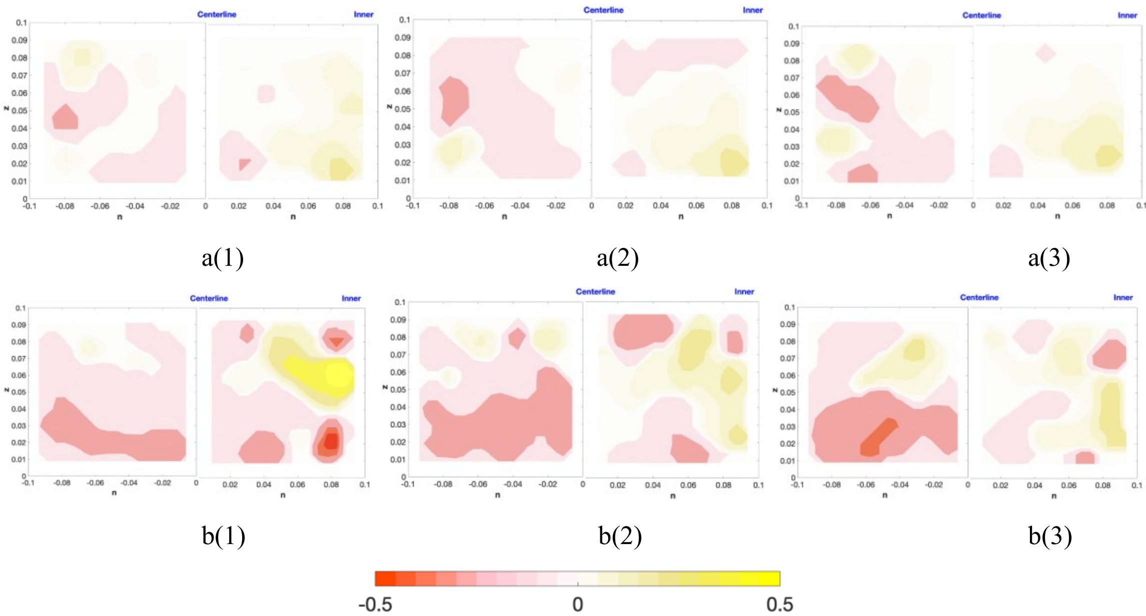

Figure 4.9 Normalized advective transport term of the vorticity equation with the influence of negatively buoyant jets (1) s=3.5, (2) s=10, (3) s=16.5, a and b are 37 and 105 degrees respectively.

Normalized values of the anisotropy term ($\left[\frac{\partial^2}{\partial z\,\partial n}\left(\overline{v_n'^2}-\overline{v_z'^2}\right)+\frac{1}{1+n/R}\frac{1}{R}\frac{\partial \overline{v'}_n^2}{\partial z}\right]/\frac{U^2}{H^2}$) profiles are provided in Figure 4.10. At the bend entrance, higher magnitudes of negative values of the anisotropy term are observed around the OBC where the two counterrotating cells are separated, thus it helps the expansion of the OBC. The maximum positive values of the anisotropy term are spotted in the vicinity of the center cell region where the high kinetic energy was observed. It also reveals that the turbulence enhances the secondary circulation at the center cell region. As the flow proceeded (Figure 4.10b(1-3)), the maximum negative values were also observed in the center cell region. Figure 11 shows the normalized cross-stream turbulent shear stress term ($\left\{\frac{1}{1+n/R}\frac{\partial^2}{\partial z^2}-\frac{\partial}{\partial n}\left(\frac{1}{1+n/R}\frac{\partial}{\partial n}\right)\right\}\left[(1+n/R)\overline{v_n'v_z'}\right]/\frac{U^2}{H^2}$), and it can be easily detected that the magnitudes are lower at 37-degrees than at 105-degrees. Comparison of the distributions between the cross-stream Reynolds stress component (Figure 4.6) and the cross-stream shear stress term show that they agree with each other. However, the observed shear stress term changes sign while the cross-stream Reynolds stress is more continuously negative. As can be seen, the positive values at the outer bank cell region are found to be nearly balanced by nearby negative values. Meanwhile, magnitudes of positive values in the center cell region were elevated as salinity increased, particularly at the 37-degree section. Nonetheless, overall, no clear correlation can be observed between the patterns of the anisotropy term and the turbulent shear stress term with the salinity.

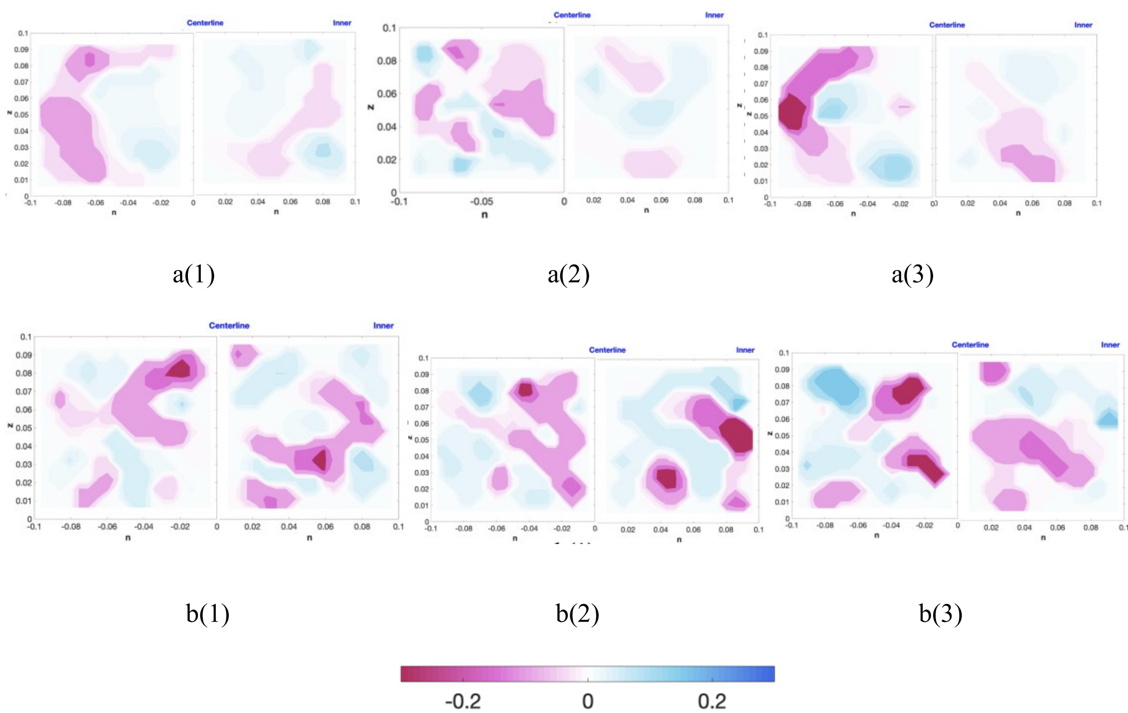

Figure 4.10 Normalized anisotropy term of the vorticity equation with the influence of negatively buoyant jets (1) s=3.5, (2) s=10, (3) s=16.5, a and b are 37 and 105 degrees respectively.

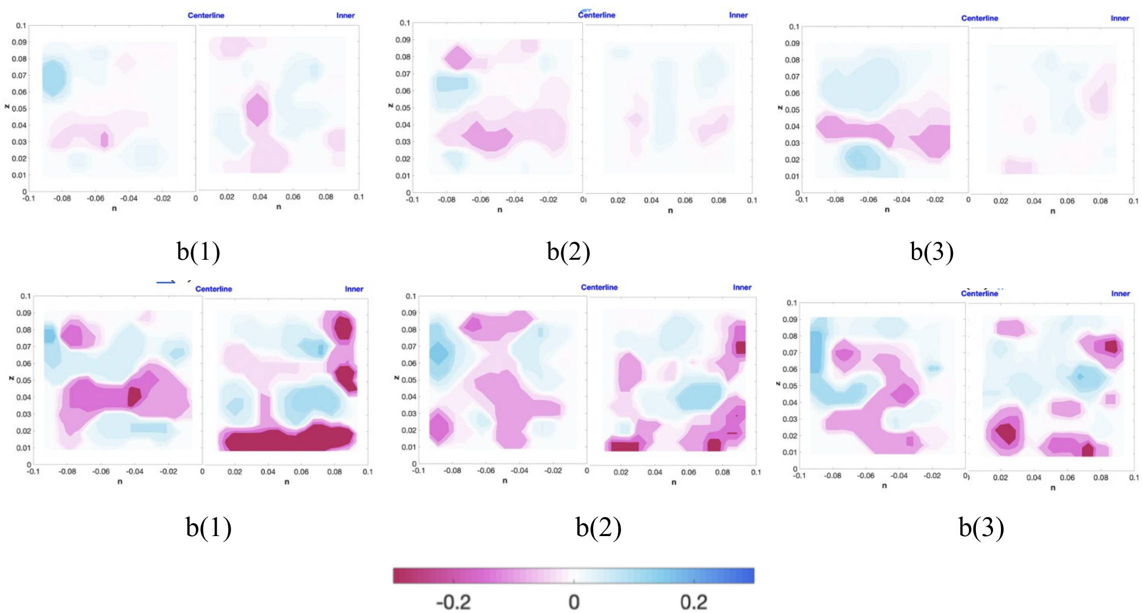

Figure 4.11 Normalized cross-stream turbulent shear stress term of the vorticity equation with the influence of negatively buoyant jets (1) s=3.5, (2) s=10, (3) s=16.5, a and b are 37 and 105 degrees respectively.

4.5 Discussion

The present paper is based on an experimental study on a 135-degree strongly curved bend flume. The experiments provided data for the analysis of different mechanisms underlying the vorticity variation with a negatively buoyant jet discharged. In all measured planes, a weaker near bank cell with an opposite sense of rotation to the center region circulation was observed. As previously reported in investigations of strongly curved turbulent (Booij,2003; Chen, 2012), velocity deformations were observed due to streamline curvature. The distribution of streamwise velocity was in good agreement with a number of flume experiments (e.g., Gholami, 2014; Moncho-Esteve, 2018; Abduo, 2021). The location and the size of the outer bank cell agreed with experiments presented by Bai (2019). With the negatively buoyant jets discharged in the bend, flow structures varied due to the mixing of dense jet with the flow. As the salinity increased, the observed OBCs increased (in size), while the center region cell shrank. A term-by-term investigation of the downstream vorticity equations was used to investigate the influence of the jets resulting from different mechanisms. The values of each term that have the same sign as the observed vorticity are considered as favoring the circulation cells, and vice versa. The centrifugal force attributed term (in agreement with the results of Blanckaert and de Vriend (2004) was found to favor the vorticity generation in the center region for all the measured cross-sections. Despite the sign of the centrifugal term, centrifugal force also favors the formation of the outer bank cells. Moreover, as salinity increased, the outer bank cell increased while the center-region cell decreased. There was a change of sign of the centrifugal term at the inner bank side, which resulted from the deformation of the streamwise velocity profile and the momentum transport. Therefore, it led to negative feedback to the center region cell. The advective transport effect plays an important role in balancing the vorticity of the flow (in agreement with Blanckaert and de Vriend (2004)). It was found that this term had a similar pattern as the distribution of the turbulent kinetic energy, which was also consistent with several studies (BLANCKAERT AND GRAF, 2004; HU ET AL, 2019). However, one can hardly observe a correlation between the cross-stream turbulence anisotropy term and the cross-stream shear stress term in the vorticity equation as salinity increases, although the negative and positive values of these terms demonstrated the location where turbulent stress opposes and favors the generation of the center region respectively. In the current experiments, the turbulent shear stress term was in disagreement with findings of Blanckaert and de Vriend (2004) at 105-degree at the bottom in the inner bank. In cases with salinity of 3.5 and 10 at 37-degree cross-section, the cross-stream turbulent shear stress significantly dissipated the vorticity at the outer bank cell region. The role of both the cross-stream anisotropy terms and the turbulent shear stress terms are complex, and thereby further research is needed to investigate the role of the turbulent shear stress under different conditions at different parts of the bend.

4.6 Conclusion

In this study, experiments were conducted in a laboratory flume to investigate the generation and dissipation of the vorticity by considering the effective terms of the vorticity equation. The results of the investigated influence with the occurrence of negatively buoyant jets provided useful hints about the flow structure variation in natural rivers. In addition, the present study contributes to the understanding of the mixing behavior effluents in water bodies. The observations focused on negatively buoyant jets of three different salinity values. Aside from the commonly observed circulation of secondary flow in the center region, a weaker counter-rotating cell was also observed in the outer bank region for all the investigated cross-sectional planes. The results showed that the centrifugal force contributes to the generation of the center region cells and the generation of both the center region cells and outer bank cells. The discharged jets interrupted the development of the center region cell while increasing the size of the outer bank cell. Kinetic energy transfer is dominated by the advective transfer caused by the secondary flow despite the existence of jet mixing. The cross-stream turbulent stress anisotropy distribution shows that the damping effect of the water surface is attenuated by increasing the salinity of the jet. However, at side boundary this damping effect is strengthened due to the influence of the dense jet. According to the results, the cross-stream anisotropy and the turbulent shear stress terms oppose the center region cells, but their feedback to the salinity change does not illustrate a clear trend. When it comes to the outer bank cell, the values of these two terms cannot indicate how the cross-stream turbulent stress generates or dissipates the downstream vorticity. Hence, future research can concentrate on interaction between the secondary flow and the cross-stream turbulent stress, in order to understand to what extent, the salinity influences the interactions.

Chapter 5 Influence of Negatively Buoyant Jets on a Strongly Curved Open-Channel Flow Using RANS Models with Experimental Data

Published at Water 2022, 14, 347. https://doi.org/10.3390/ w14030347

Xueming Wang , Abdolmajid Mohammadian and Colin D. Rennie

Abstract: Experimental and numerical studies of flow structures in a strongly curved 135-degree laboratory flume were carried out to investigate the influence of negatively buoyant jets using the finite volume method. The performance results of three different turbulence models were investigated by comparing the numerical results with the experimental measurements. The present study demonstrates that fully 3D numerical models are capable of simulating the primary flow pattern in a strongly curved channel with the presence of a negatively buoyant jet. The comparison also shows [that the k-omega SST model can satisfactorily predict some of the smaller flow features in bend flow, such as the inner bank circulation cell and the overall form of the vorticity distributions. It was found that the flow distribution and the strength of secondary flow vary with different salinity conditions. The main contribution of this study is the identification of a numerical method that can be further applied to pollutant transport for real river problems.

Keywords: Strongly curved channel; RANS; OpenFOAM; turbulence model; numerical simulation; negatively buoyant jets.

5.1 Introduction

The investigation of flow structures in open channel bends is of great importance in hydraulic and environmental engineering sciences. Subjects related to super-elevation and bank erosion/shifting, bed scouring and sediment transport, migration of meanders and shear stress redistribution, as well as heat and salinity transfer have been proven to be attributed to river curvature (CHANG, 1971). A special feature of a curved open channel is the existence of secondary flow, resulting from the combination of lateral pressure gradients and centrifugal forces, i.e., the inclined free surface yielded transverse pressure gradient cannot balance the centrifugal force, which causes the water molecules at the bottom to move towards the inner bend and particles at the water surface to move towards the outer bend (KASHYAP ET AL., 2012). The magnitude of the cross-stream motion, which is particularly responsible for velocity redistribution and boundary shear strength, can be as much as 10-40% of the bulk streamwise velocity (YE AND MCCORQUODALE, 1998). Although the helical flow pattern has been reported for over a century, relatively few studies have assessed how secondary flows in strongly curved bends influence mixing of effluents (CHOI ET AL., 2005). To address this problem there is a need to employ fully three-dimensional models instead of to conventional depth-averaged models (CHOI ET AL., 2005; SONG ET AL., 2012), as well as high-resolution measurements of all velocity components.

Earlier theoretical investigations on secondary flow structure have been made mostly based on the physical properties defined by the channel geometry, such as curvature ratio (bend radius/channel width, R/B), aspect ratio (channel width/flow depth, B/H), and flow depth / bend radius (H/R=H/B*B/R) (ROZOVSKII, 1961; LEPPOLD ET AL., 1960). Later, Blanckaert and Ottevanger (2011,2012), em-ployed a parameter $Cf^{-1}H/B$ to interpret flow redistribution governing processes and flow structures in bends, and they broadened the applicability range for both mildly and strongly curved channels. Moreover, many efforts have been made to take into account the influences of topography and geomorphology on curved channel flow, for instance, bathymetry or point bar and deflection angle, while aiming to enhance the under-standing in order to approximate natural rivers (KASHYAP ET AL., 2012; ENGELUND & SKOVGAARD, 1973; IKEDA ET AL., 1987;JAMIESON AND RENNIE, 2010; ZENG ET AL., 2008; KALKWIJK AND DE VRIEND,1980; METCALF & EDDY,1979&1991). However, although much work has been conducted on the details of the formation and structures of secondary flow as-sociated with channel geometry (CHENG AND FAROKHI, 1992; DE VRIEND, 1980), even considering man-made infrastructure, very little attention has been paid to the effects of the variation of flow fluid properties on secondary flow.

Recently, the demands of optimizing the use of natural water bodies and mitigating environmental impacts have been emphasized, so that water pollution problems can be effectively controlled. Domestic and industrial effluents, also known as turbulent buoyant jets, are commonly discharged into rivers, estuaries and oceans to provide for disposal in urban areas (DUAN ET AL., 2005). During a diffusion process, flowing fluid can easily condition the effluents, and additional complexities of the flows include the complicated interaction between effluents and the secondary flow caused by the curvature of the streamlines. It has been found that turbulence plays an important role in open channel bends.

With turbulent buoyant jets, the original flow structures and turbulence in the bends will be continually disturbed by the jets in crossflow. After accumulating a certain quantity of fluids with different densities, the water properties in the bend are changed. This poses some problems compared to the bends without jets; hence, flow and turbulence characteristics need to be thoroughly examined in order to acquire reliable predictions on three-dimensional (3D) flow fields for both scientific research and practical purposes.

Flow dynamics in channel bends can be studied experimentally and numerically. Considerable effort has been put into measuring and evaluating the secondary flow in laboratory bends (CHANG, 1971; YE AND MCCORQUODALE, 1998; ODGAARD & BERGS,1988; BOOIJ, 2003; BLANCKAERT AND DE VRIEND, 2004; BLANCKAERT, 2009; BLANCKAERT AND GRAF, 2004) .The rapid development of computer science has strengthened a series of mathematical models for hydrodynamics to better elucidate and predict the details of 3D flows in bends since the 1980s. Most of the pioneering work was carried out on closed ducts (PATANKAR AND SPALDING, 1972; PATANKAR ET AL., 1975). De Vriend (1981) developed a mathematical model for the prediction of the helical flow pattern in a shallow flow conduit with respect to the Dean number. He determined that the influence of the side-wall region cannot be neglected as soon as secondary flow convection was fully developed, but instead of using any turbulence model, laminar flow condition was employed in the analysis. Leschziner & Rodi (1979) developed a k-ε turbulence model to interpret flow structure in a strongly curved open channel and they also extended their research to closed conduits; however, due to computer storage economization, pressure values were stored two-dimensionally and streamwise diffusion was neglected. Demuren and Rodi (1986) modified the model pro-posed by Leschziner & Rodi (1979), so that the refined k-ε model could account for streamline curvatures, bed morphology and turbulent transport. Nevertheless, according to Demuren and Rodi (1986) continuity errors could happen as a result of the application of "rigid lid" approximation, which prevailed in early simulations. The standard k-ε model was insufficient to solve problems within complex flows due to the isotropic eddy viscosity assumption, hence, many attempts were made to resolve the defect, either by calculating the turbulence stress from more complex stress models or by posing a substitute for the isotropic viscosity in the standard model (RUTHER AND OLSEN, 2005). Later, Ye and McCorquodale (1998) introduced a k-ε model to overcome the anisotropic influences caused by streamline curvature, free surface, and solid walls by obtaining the turbulent viscosity from algebraic stress models (ASM) or Reynolds stress models (RSM) models. But given a shallow flow, the bed morphology was treated as a solid wall damping effect. Subsequently, Ruther and Olsen (2005), Khosronejad et al. (2007) and Zeng et al. (2008) applied fully 3D Reynolds averaged numerical simulation (RANS) model in strongly curved channels with both flat bed and moveable beds, which broadened the capability of RANS models on the scouring and deposition process of open channel bends. Zeng et al. (2008) found larger discrepancies in modelled versus measured velocity in the transverse direction compared to the streamwise direction, especially for the mobile bed case. Several researchers have since developed large eddy simulation (LES) models of open channel bend flows (SHAHEED ET AL.,2021; VAN BALEN ET AL., 2009 AND 2010; CONSTANTINESCU ET AL., 2013), but the computational demand of LES models often precludes their use in real full-scale scenarios.

The motivation for the present work is to provide experimental data and numerical simulations on the distribution of the 3D flow velocity and turbulence in a strongly curved laboratory flume by means of a non-intrusive method. Negatively buoyant jets with different densities were continually discharged into the flow at the outer sidewall as a crossflow, and the velocity field was measured with a particle image velocimetry (PIV) system. The data were then used as a reference for model validation of three RANS models, the standard k-ε model, the non-linear k-ε model and the k-ω shear stress transport (SST) model. Experiments in this study aim to demonstrate the natural situation of effluent discharge activities. The flume employed in this study is an asymmetric 135-degree bend with a rectangular cross-sectional shape and a uniform flat channel bed. Although the reduction of topographical conditions yields more discrepancies than in natural rivers, the present study can still serve the understanding of river engineering. More specifically, four issues need to be addressed in this study. Firstly, to determine whether the occurrence of a buoyant jet will influence the secondary flow structure in a bend. Secondly, to evaluate the performance of various RANS models on the simulation of a strongly curved channel bend along with dilution problem. Thirdly, to inspect in-fluence of the density difference on flow structure. Fourthly, to investigate the turbulence structures of the flow. Data sets obtained from the validated numerical model are used for this analysis, to enable a more comprehensive view of the interaction of the effluent jet with the strongly curved open channel bend flow.

5.2 Methodology

5.2.1 Experimental setup and domain

Measurements in this study were taken in a laboratory single bend flume, which consists of a straight entrance section with a length of 2 m and a 135-degree bend followed by a straight exit section of 0.5 m. The width of the entire flume is uniformly B=0.2m, and the centerline length is 3.2m. The bed of the flume was set horizontally, and both the bottom and the vertical sidewalls are hydraulically smooth. The radius of curvature at the centerline of the bend is R=0.3m. Therefore, the aspect ratio of the flume under study is R/B=1.5, which makes it a strongly curved open channel. Water depths of all the experiments were H=0.1m, and the bulk velocity of the flow was 0.1m/s. The flows in all the experiments were sub-critical flows as the Fr = 0. 22 (Froude number) <1, and they were also fully turbulent as the Reynolds number of each test was 22400.

Table 5.1 Hydraulic conditions for the main flow

Q(l/S)	V(m/s)	H(m)	R(m)	B(m)	Re	Fr	R/B	B/H
2	0.1	0.1	0.3	0.2	22400	0.22	1.5	2

Salt-water with various salinities of 3.5, 10 and 16.5 was used for the negatively buoyant jets discharged into the channel. The nozzle was on the outer bank wall of the straight inlet section. The center of the round nozzle was 5cm above the flume bed and the distance between nozzle center and the bend entrance was 0.55m. Each effluent jet was discharged perpendicular to the wall, horizontally as a crossflow into the main flow. The initial velocity of each jet was kept constant using a constant head tank at a value of 0.2m/s.

A schematic diagram of the experimental setup is shown in Figure 5.1. The stream-wise, wall-normal and spanwise directions are denoted by x, y and z, respectively; the corresponding three components of the fluctuating velocities are u, v, and w.

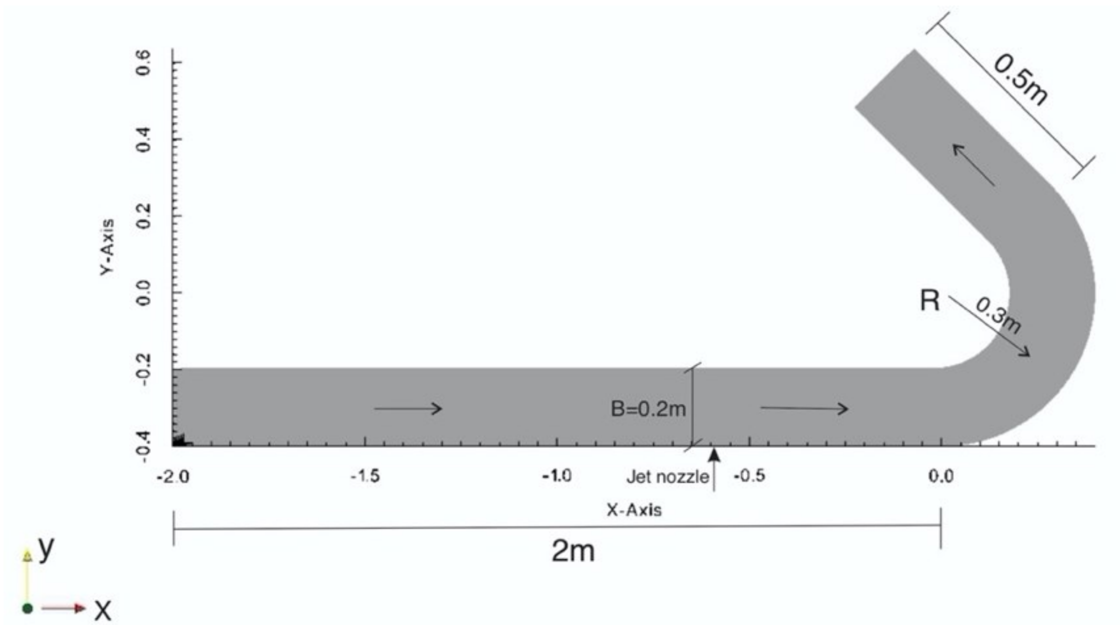

Figure 5.1 Flow geometry of the experiment

5.2.2 Experimental Methods

Velocity measurements were taken for all experiments using the particle image velocimetry (PIV) method. PIV is an optical measurement technique by which the velocity field and related flow properties of an entire interrogation plane can be measured simultaneously. A typical PIV apparatus consists of a camera (normally a digital camera with high quality CCD chips), an illumination source (a laser output device) and a synchronizer (a timing unit) to operate as an external trigger for the control of the camera and the laser. In addition, the fluids under investigation should be seeded before measuring. In the present study, stereoscopic PIV (stereo-PIV) measurements were executed to mitigate the influence of distortion caused by the bend, and to obtain a measurement of the out-of-plane velocity at each measured section. Each measurement was made with a sampling frequency of 30 Hz, for an examination period of 40 seconds.

Measurements were performed at 4 different cross sections in the flume: 37, 90, 105, and 125 degrees. Data generated for one cross-sectional plane were composed by two measurements, and each PIV measurements covers half of the section. The maximum relative uncertainty of the measurements was evaluated by post-processing software along with the PIV system. The relative uncertainty values were found to be 10% in the streamwise direction, 20% for the cross-sectional velocities, and 30% in the vertical direction. However, due to the material and the geometry of the flume, strong reflection was observed at the solid boundaries. The complete image of each measurement is subdivided by the interrogation windows, then each interrogation window is evaluated by cross-correlation to generate a local vector. Details of the cross-correlation of the PIV data processing can be found in the manual FlowMaster Chapter 3.2 (Page 18). The averaged resolution of each measured plane was 44 interrogation windows with the width and 22 interrogation windows with the depth. In the current setting, the PIV measurements yielded low correlations and high uncertainties in a flow layer of approximately 0.5 to1 cm near solid boundaries.

5.2.3 Numerical methods and turbulence models

5.2.3.1 Numerical models

The geometry in the numerical simulations was the same size as the physical domain in the experiments (Figure 5.2). In the present study, the incompressible Navier-Stokes equations were solved by using the finite volume method for the liquid coupled with the volume of fluid method for the salinity distribution. All the simulations were performed with open-source code OpenFOAM via the multi-fluid turbulence solver called twoLiquidMixingFoam. The twoLiquidMixingFoam software was developed to solve problems regarding the mixing of two incompressible fluids, and it has been utilized and substantiated in many studies (Zhang, 2015; Yan and Mohammadian, 2017). The implementation of the turbulence models was managed by employing different schemes for each term in the governing equations. A Eulerian scheme was used to discretize the temporal term. The gradient terms were controlled by the Gauss linear scheme, while a Corrected Gauss linear scheme was used to discretize the Laplacian term. Gauss vanLeer, Gauss linear and bounded Gauss upwind schemes were assigned to the divergence terms. To interpolate values from one set of points to another, a linear scheme was used in discretization.

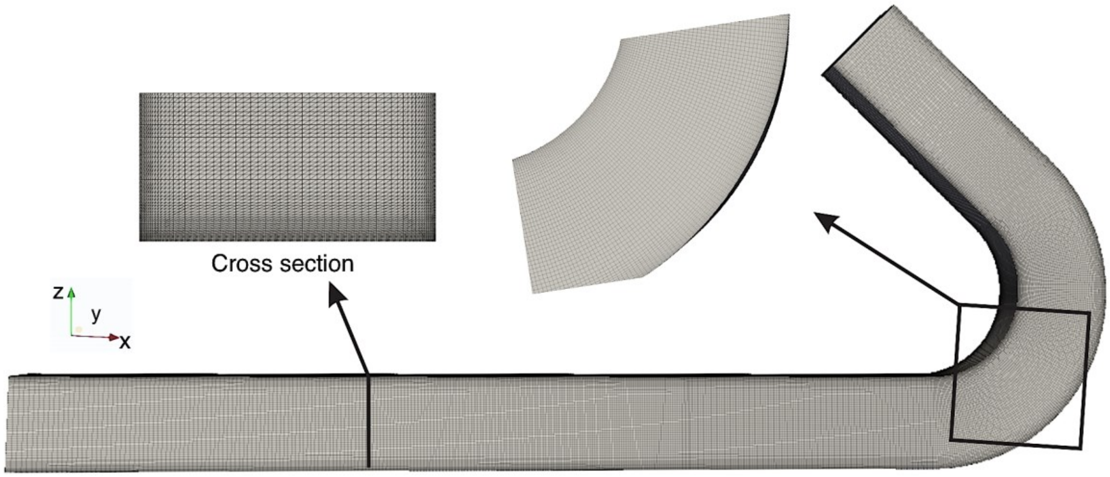

Figure 5.2 Structured mesh for numerical simulations, also showing a detailed view of the mesh and the cross-sectional view.

5.2.3.2 The standard k-ε model

The three-dimensional flow field is interpreted by solving the continuity equation and the Reynolds Averaged Navier–Stokes equations, which can be written as:

$$\nabla \cdot U = 0 \tag{5.1}$$

$$\frac{\partial \rho U}{\partial t} + \nabla \cdot (\rho U U) = -\nabla \cdot \left(p_{rgh}\right) - gh\nabla\rho + \nabla(PT) \tag{5.2}$$

where t is time, U indicates velocity, and ρ is the fluid density, g is the gravity, p_{rgh} is the hydrostatic pressure for the pressure calculations.

With the Boussinesq assumption, the turbulence stress can be expressed as:

$$\overline{u_i u_j} = \nu_t \left(\frac{\partial U_i}{\partial x_j} + \frac{\partial U_j}{\partial x_i}\right) - \frac{2}{3} k \delta_{ij} \tag{5.3}$$

The realizable k-ε model is used in the present simulation for the RANS model; the turbulent kinetic energy k and its dissipation rate ϵ are obtained from the following equations:

$$\frac{D}{D_t}(\rho k) = \nabla \cdot (\rho D_k \nabla k) + \rho G - \frac{2}{3}\rho(\nabla \cdot u)k - \rho\epsilon + S_k \tag{5.4}$$

$$\frac{D}{D_t}(\rho\epsilon) = \nabla \cdot (\rho D_\epsilon \nabla\epsilon) + C_1\rho|S|\epsilon - C_2\rho\frac{\epsilon^2}{k + (\nu\epsilon)^{0.5}} + S_\epsilon \tag{5.5}$$

$$\nu_t = C_\mu \frac{k^2}{\epsilon} \tag{5.6}$$

$$C_\mu = \frac{1}{A_0 + A_1 \frac{kU^*}{\epsilon}} \tag{5.7}$$

The default model coefficients are $C_\mu = 0.09; C_1 = 1.44; C_2 = 1.92; C_{3,RDT} = 0.0; \sigma_k = 1.0; \sigma_\epsilon = 1.3.$

5.2.3.3 The non-linear k-ε model (Shih Quadratic k-ε)

The turbulence kinetic energy equation is given by:

$$\frac{D}{Dt}(k) = \nabla \cdot (D_k \nabla k) + G - \epsilon \tag{5.8}$$

and the dissipation rate by:

$$\frac{D}{Dt}(\epsilon) = \nabla \cdot (D_\epsilon \nabla\epsilon) + C_1 G\frac{\epsilon}{k} - C_2\frac{\epsilon^2}{k} \#(5.9)$$

the turbulence generation G is given by:

$$G = [\nu_t(\nabla \boldsymbol{u} + (\nabla \boldsymbol{u})^T) - \tau_{nl}]: \nabla \boldsymbol{u} \tag{5.10}$$

Where τ_{nl} is the non-linear stress.

5.2.3.4 The k-ω SST (Shear Stress Transport) model

The complete formulation of the k-ω SST model used in the current paper is given as:

$$\frac{\partial(\rho k)}{\partial t} + \frac{\partial(\rho U_i k)}{\partial x_i} = \min(G, c_1 \beta^* k\omega) - \beta^* \rho k \omega + \frac{\partial}{\partial x_i}\left[(\mu + \alpha_{ki}\mu_t)\frac{\partial k}{\partial x_i}\right] \tag{5.11}$$

$$\frac{\partial(\rho\omega)}{\partial t} + \frac{\partial(\rho U_i \omega)}{\partial x_i} = \frac{\alpha \tilde{P}_k}{\mu_t} - \beta\rho\omega^2 + \frac{\partial}{\partial x_i}\left[(\mu + \alpha_{\omega i}\mu_t)\frac{\partial \omega}{\partial x_i}\right] + 2(1 - F_1)\rho\sigma_{w2}\frac{1}{\omega}\frac{\partial k}{\partial x_i}\frac{\partial \omega}{\partial x_i} \tag{5.12}$$

Where the blending function F1 is defined by:

$$F_1 = \tanh\left\{\left\{min\left[max\left(\frac{\sqrt{k}}{\beta^* \omega y}, \frac{500v}{y^2\omega}\right), \frac{4\rho\sigma_{\omega 2}k}{CD_{k\omega}y^2}\right]\right\}^4\right\} \tag{5.14}$$

with $CD_{kw} = max\left(2\rho\alpha_{\omega 2}\frac{1}{\omega}\frac{\partial k}{\partial x_i}\frac{\partial \omega}{\partial x_i}, 10^{-10}\right)$ and y is the distance to the nearest wall.

F1 is equal to zero away from the surface (k-ε model) and switches over to one inside the boundary layer (k-ω model).

The turbulent eddy viscosity is defined as follows:

$$v_t = \frac{a_1 k}{max(a_1\omega, SF_2)} \tag{5.15}$$

Where $S = \sqrt{2S_{ij}S_{ij}}$ is the invariant measure of the strain rate and F2 is a second blending function defined by:

$$F_2 = \tanh\left[\left[max\left(\frac{2\sqrt{k}}{\beta^*\omega y}, \frac{500v}{y^2\omega}\right)\right]^2\right] \quad (5.16)$$

A production limiter is used in the SST model to prevent the build-up of turbulence in stagnation regions:

$$S_{ij} = \frac{1}{2}\left(\frac{\partial u_j}{\partial x_i} + \frac{\partial u_i}{\partial x_j}\right) \quad (5.16)$$

$$G = \mu_t S^2 \quad (5.17)$$

All constants are computed by a blend of the corresponding constants of the k-ε and the k-ω model via α =α1F +α2(1−F) etc. The constants for this model are: β*=0.09, α1=5/9, β1=3/40, αk1=0.85, σω1=0.5, α2=0.44, β2=0.0828, σk2=1, σω2=0.856.

5.2.4 Boundary conditions and model setup

A stress-free rigid lid condition was adopted to produce the effect of the free surface in the present study. Simulations with rigid lid assumption have been accepted with reasonable accuracy for the RANS models if the Froude number is smaller than 0.5 and the gradient of the water's surface can be neglected (Kashyap et al., 2012; Zeng et al.,2008; Yang, 2015). Due to the computational capacity and the limitations of OpenFOAM, the mesh grids near the solid boundary cannot be fine enough to reach the resolvable grid size for viscous sub-layer calculation. Therefore, the wall-function approach was imposed to represent the viscous sub-layer, the buffer layer and the logarithm layer on each wall boundary in the RANS simulations. Before the comparison, a mesh sensitivity analysis was conducted by using different meshes with increasing resolution in the grids, until it can provide steady results with enough accuracy.

Table 5.2 Parameters of the simulated cases

Run	Salinity	Simulation type	Density difference
No-1	No jet	k-ε	-
S3.5-1	S3.5	k-ε	3
S10-1	S10	k-ε	8
S16.5-1	S16.5	k-ε	13
No-2	No jet	Non-linear k-ε	-
S3.5-2	S3.5	Non-linear k-ε	3
S10-2	S10	Non-linear k-ε	8
S16.5-2	S16.5	Non-linear k-ε	13
No-3	No jet	k-ω SST	-
S3.5-3	S3.5	k-ω SST	3
S10-3	S10	k-ω SST	8
S16.5-3	S16.5	k-ω SST	13

The labelling of the simulation runs (first column of Table 5.2) is as follows. The first character denotes the density difference: S35 means the low salinity case, S10 means the medium case, S165 means high salinity case and No stands for the no jet case. The number indicates the type of simulation applied: 1 represents the k-ε model, 2 represents the Non-linear k-ε models and 3 represents the k-ω SST model.

5.3 Results and analysis

5.3.1 Model evaluation

The performance of each numerical model was evaluated by calculating the overall difference between experimental and numerical results. Results showed that the averaged RMSEs (root mean square errors) of the simulated total velocity magnitudes were 0.029

m/s, 0.028 m/s and 0.027 m/s for the k-ε mode, the non-linear k-ε model and the k-ω SST model respectively, indicating that the 3D numerical models can provide reasonable results for the flow field within the bend.

5.3.2 Velocity distribution

To achieve better analysis, velocity profiles over the flow depth are shown for quantitative investigations with results of the k-ω SST model, k-εmodel and non-linear k-ε model; specifically, transverse, vertical and streamwise velocity profiles at certain cross sections in the flow are highlighted. In the current setup of the stereo-PIV, the included angle of the two cameras inevitably changed due to the moving of the laser and the cameras during measuring different cross sections. Therefore, the resolution of the images taken from different cross sections varied slightly, which generated different mapped meshes of target flow surfaces. By avoiding the high uncertainty areas near the solid boundary, the transverse locations of the profiles are approximately 0.10B, 0.2B, 0.3B, 0.4B, 0.6B, 0.7B, 0.8B and 0.9B. Then, the time-averaged stream-wise velocities, u, and transverse velocities, v, of the experiments and numerical simulations results are shown, non-dimensionalized by the bulk velocity of the mean flow in the straight inflow channel, U.

Figure 5.4 compares the streamwise velocity distribution with experimental data under different jet salinities at the 90-degree section. As can be seen, the streamwise velocity profiles from the k-ω SST model agrees with the experimental results with reasonable accuracy, especially for the no-jet and low-salinity conditions (Figure 5.3 (a) and (b)). For the highest salinity case, the streamwise velocities seem to be underestimated in relation to the lower part at the outer bank side (Figure 5.3 (d)) and the upper part at the inner bank. Due to the generally formed secondary current as the flow proceeded, the velocity deformed in all three directions x, y, z, i.e., velocities did not behave according to a logarithmic distribution with depth in the bend section. Except for the center region secondary flow, there is another weak circulation cell existing at the outer bank region close to the water surface. This can be found in Figure 5.3, with the experimental results showing that the velocity profiles deformed in the mentioned region. Discrepancies are observed for the numerical simulations for all the cases in the outer bank region.

As can be seen from Figure 5.4, the agreement of the transverse velocity profiles for the medium case is quite good, but for the lower salinity case, the numerical results are of lower quality. The transverse velocities seem to be overestimated by the numerical computations at both the bottom regions and the water's surface. However, as salinity increases, the agreement of the velocity profiles for the higher salinity cases gets better at the water's surface of the inner bank, especially for the S=10 case. The disagreement might be due to applying the rigid-lid assumption to the free surface, and it could also indicate that the mixing of negatively buoyant jets attenuates the spatial development of the flow structure at the inner side. Another explanation for the discrepancy can be attributed to the measurement technology in that a high intensity of reflection causes noise at the investigated boundaries.

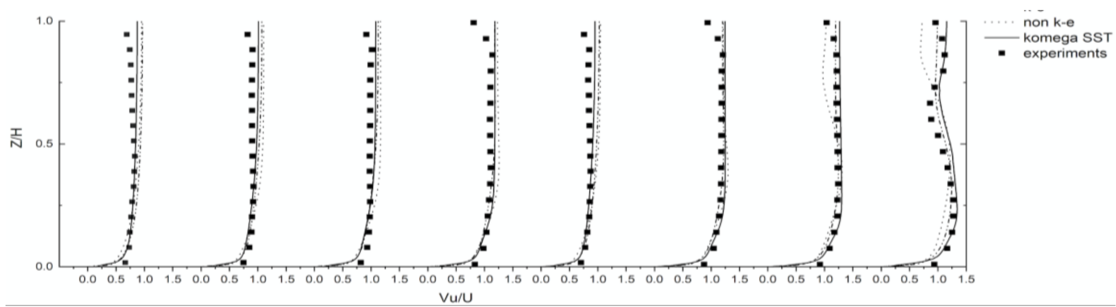

(a)

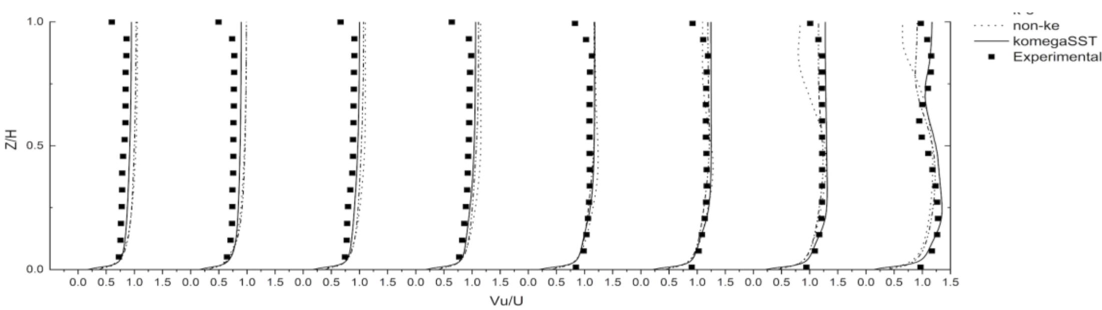

(b)

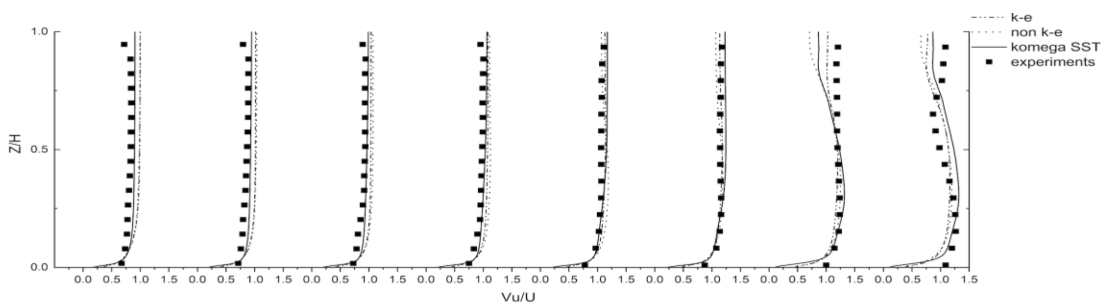

(c)

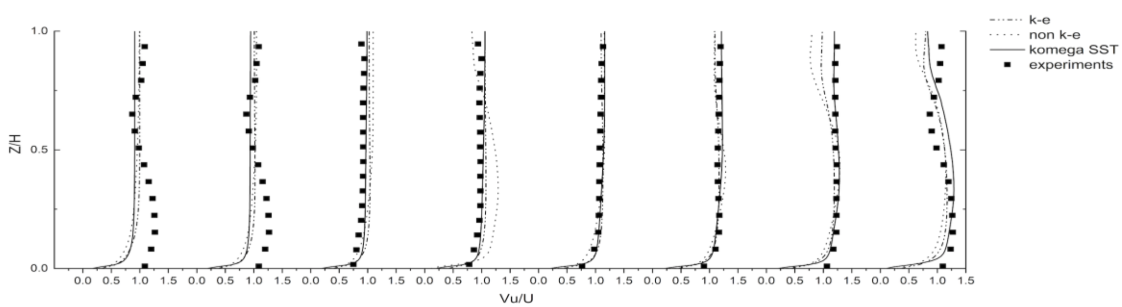

(d)

Figure 5.3 Distribution of streamwise component of velocity at 90 degrees under different jet conditions: (a) no jet, (b) S =3.5 (c) S =10 and (c) S=16.5. From the left to the right is the outer bank to the inner bank.

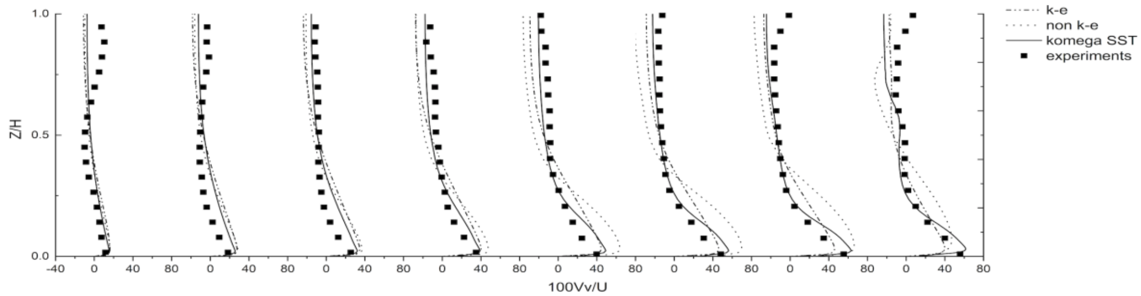

(a)

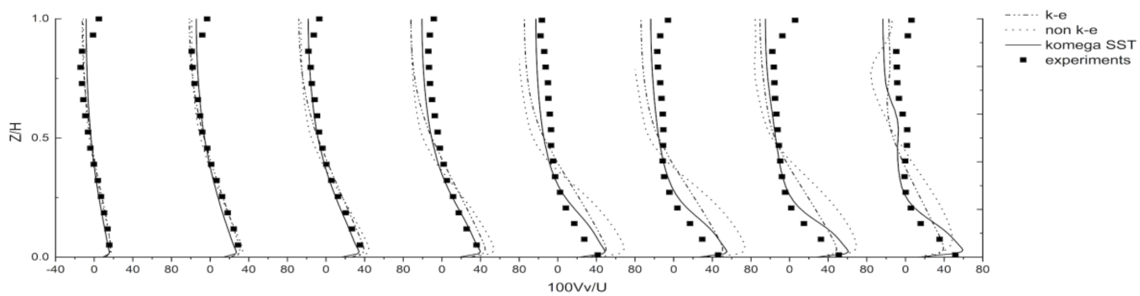

(b)

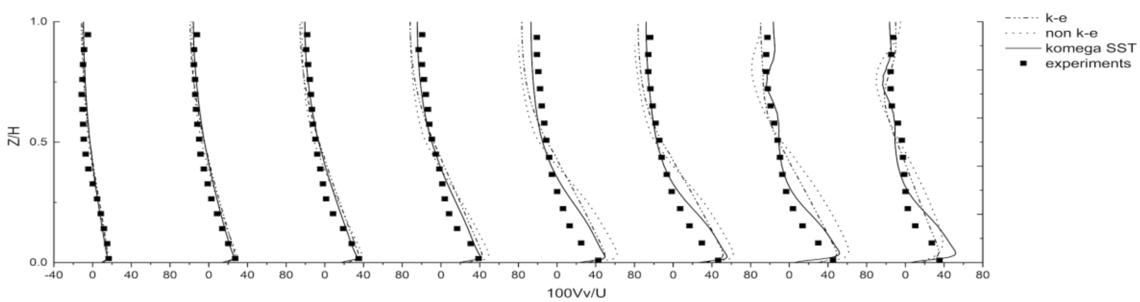

(c)

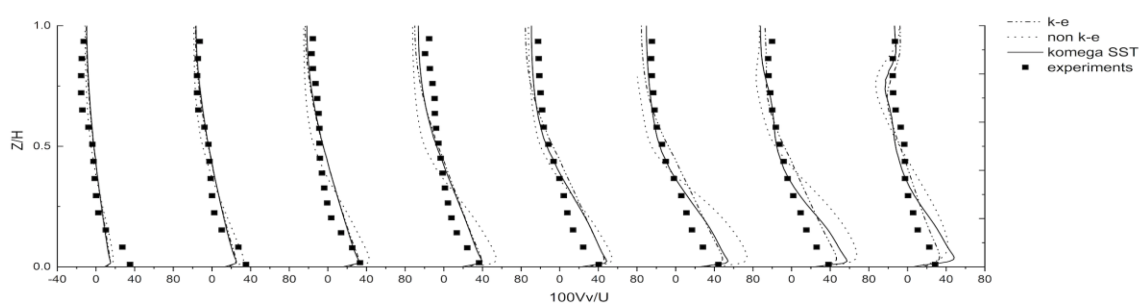

(d)

Figure 5.4 Distribution of transverse component of velocity at 90 degrees with different jet conditions: (a) no jet, (b) S =3.5 (c) S =10 and (c) S=16.5. From the left to the right is the outer bank to the inner bank.

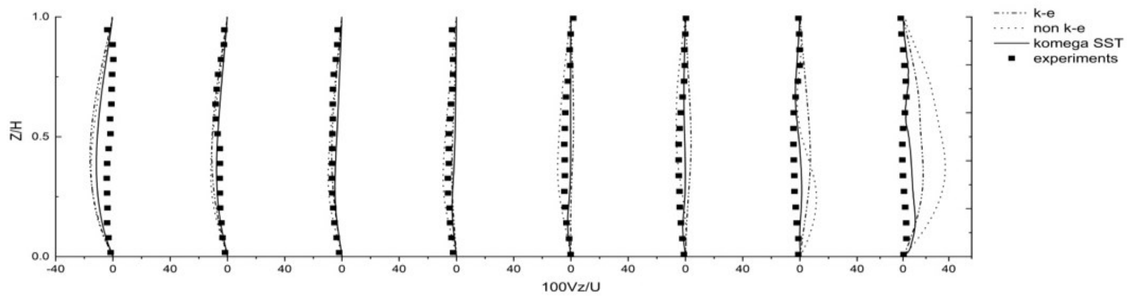

(a)

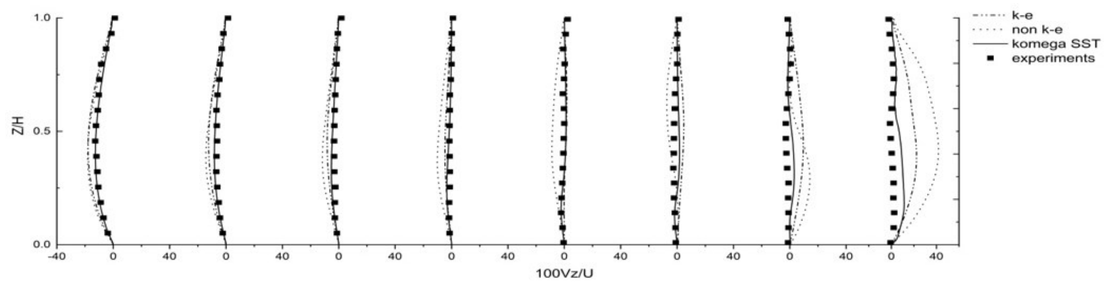

(b)

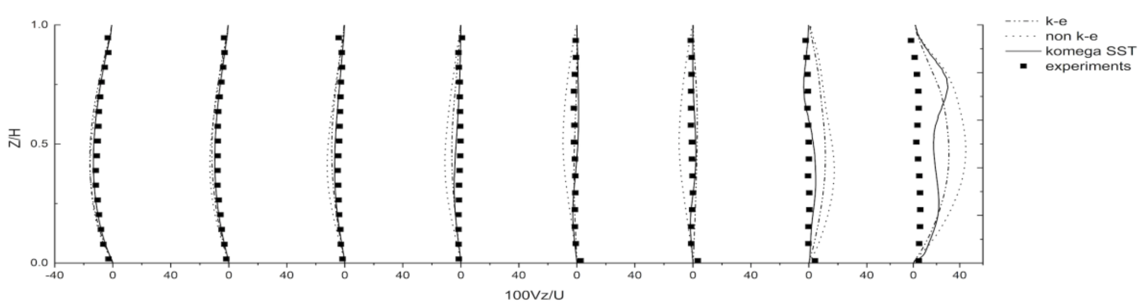

(c)

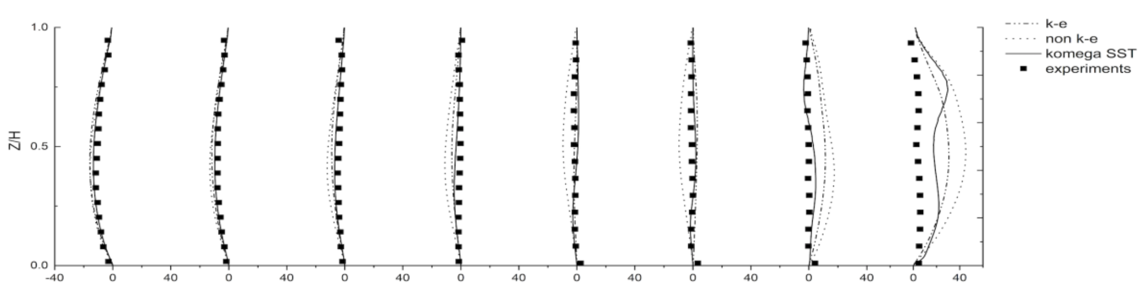

(d)

Figure 5.5 Distribution of vertical component of velocity at 90 degrees with different jet conditions: (a) no jet, (b) S =3.5 (c) S =10 and (c) S=16.5. From the left to the right is the outer bank to the inner bank.

Figure 5.5 shows the vertical component of the velocity profile. Weaker agreements of the vertical velocities were also found with the higher salinity case at the boundaries, and as the salinity increases, the disagreement was amplified. Despite this, it is obvious that the k-ω SST model exhibited better performance in predicting the vertical velocities in the bend under the influence of negatively buoyant jets. It can also be seen that the presence of negatively buoyant jets reverses the vertical velocity signs at the water's surface, and the maximum value of the vertical velocities move close to the bottom as salinity increases.

5.3.3 Secondary flow pattern

The plots of streamlines at the 90-degree section under the no-jet condition and three different salinity cases are presented in Figure 5.6. In this part, secondary flow properties were only compared using the results obtained by the k-ω SST model to the experimental measurements since this model provided the best performance. As mentioned in the velocity properties, the outer bank cells under all the various scenarios were not captured by the k-ω SST model. However, the classical radial flow (also known as the main cell) towards the inner wall, which was caused by the imbalance between the centrifugal force and the lateral pressure gradient, can be seen at the 90-degree section with good agreement. As can be seen in Figure 5.6, the center of the main cell is moving upward to the water's surface in both the numerical results and the measurements when salinity increases. Moreover, at the inner bank side, there are regions with adverse velocity vectors, which have been widely demonstrated as separation zones. It has been reported that flow separation is promoted by the difference between the pressure gradient force caused by the streamline curvature and the inertial forces (BLANCKAERT,2015). As the salinity increases, it can be found that the separation zones enlarge (marked by the red line).

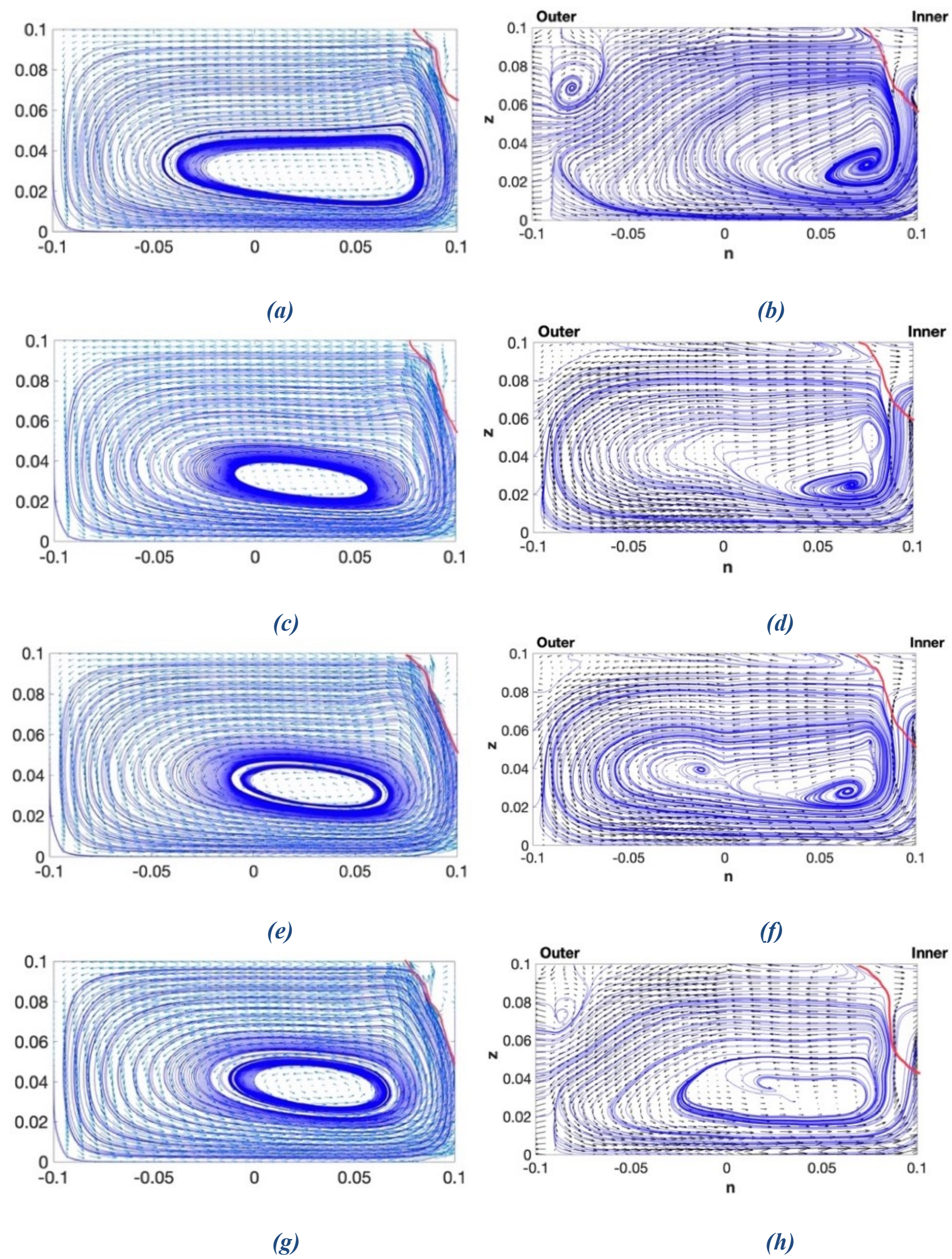

Figure 5.6 Secondary flows at the 90 degree section under different conditions: a, b- No jet; c, d - s==3.5; e, f - S=10; g, h - S=16.5. The left column figures represent the numerical results, and the right column are the experimental results.

To obtain better comprehension of the secondary flow, the averaged streamwise vorticities for all the scenarios considered at the 90-degree cross-sectional plane were calculated and presented in Figure 5.7. As shown, the positive vorticity covers most of the channel cross-section, which represents the presence of the classical helical flow in a bend. The negative values of the vorticity at the outer bank side proved the existence of the outer bank circulation cell, which has an opposite sense of rotation to the main cell. At the inner bank, negative values were also observed within a narrow region, representing the separation zones of the bend, and the flow separation behavior was strengthened as salinity increases. Furthermore, it can be found that the high positive vorticity cores at the inner bank of the channel are retreating and shrinking towards the inner wall as salinity increases.

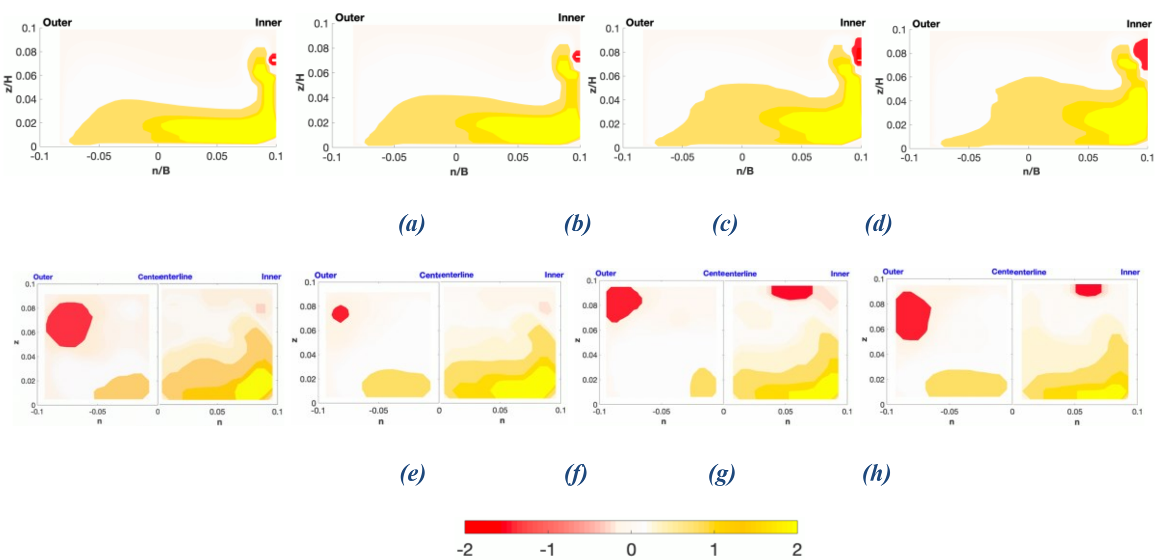

Figure 5.7 Vortex contour of the secondary flows under different conditions: a, e - No jet; b, f - s=3.5; c, g - S=10; d, h - S=16.5. Figures in the first row represent the numerical results, and the ones at the second row are from the experimental results.

5.4 Discussion

It is commonly accepted that flow behaviors in bends should be treated with an advanced turbulence model, such as the LES models, Reynolds stress models or even DNS models. Despite the high-quality performance, time and computational costs are still the primary obstacles for widely applying these models. Although problems related to the topic of this paper are quite complex, it is worth attempting to use two-equation Boussinesq turbulence models and to determine how precise the results are.

The present paper is an experimental and numerical study on a strongly curved 135-degree open channel bend. The findings of the present study involve the influences of the mixing behavior of negatively buoyant jets on the flow distribution and secondary flow cells in the bend, which are profound in environmental engineering. One crucial advantage of the present work is the direct comparison of parameters between the high-resolution three-dimensional measurements and fully three-dimensional numerical results, which helps foster a thorough understanding in model analysis. The present results imply that flow structures, with the interaction of negatively buoyant jets in a channel bend, are distinct from the bends without jets. It also shows that the flow distribution was considerably influenced by the jets mixing behavior. In a channel bend without a jet, the size of the outer bank cell is larger than that of a channel bend with jets, while the inner bank flow separation process was enhanced with the latter cases of bends with jets. Moreover, flow redistribution in a channel bend resulting from the pressure gradient imbalance was more complicated in the presence of jets, and the effects varied with respect to each velocity component at different locations. Overall, the results demonstrate that the salinity of a negatively buoyant effluent jet will have important consequences for its interaction with secondary flow structures and associated mixing in an open channel bend.

5.5 Conclusions

In this study, numerical modelling of the flow pattern with the influence of negatively buoyant jets at a strongly curved open channel bend was carried out to compare the results of using fully 3D RANS turbulent models (the standard k-ε model, non-linear k-ε model, and the k-ω SST model) with the results from an experimental channel. The performance of these models was evaluated in this channel.

The key findings of the research are listed below:

- With all the applied turbulence models, the streamwise velocities were all well predicted for the lower salinity cases. Discrepancies were found near the water's surface at the outer bank region due to the inability of resolving the outer bank cell numerically. Reasonable agreement was obtained concerning the transverse velocities between the numerical results and the measured data. The major computational differences were observed with the vertical velocity component. Overall, the k-ω SST model exhibited the best performance in the present study. The computational errors can be attributed to the use of the isotropic eddy viscosity and the rigid-lid free surface assumption.
- The velocity patterns in all three directions were influenced by the effect of secondary flow, which was attained in the channel bend by the experimental data and numerical simulations.

- The overall shapes of streamlines at each salinity case are different from each other because of the interaction between the jet mixing behavior and the secondary flow in the channel bend.
- The presence of negatively buoyant jets disturbed the development of the outer bank cell, and that interruption was attenuated as salinity increased.
- In the inner bank region, flow separation was strengthened by the participation of the negatively buoyant jets.
- High positive streamwise vorticity cores, which represent the main circulation, were found at the inner bank, and they were pushed towards the inner bank wall as salinity increased.

The present study only focuses on RANS models. The authors suggest that other turbulence models (such as LES, RSM, etc.) are worth studying, and the alternative boundary conditions need to be further investigated. Future research objectives would also involve the influence of more types of jets, the discharge location, as well as the jets' mixing characteristics.

5.A. Appendix

The numerical computational domain was the same as the geometry of the physical model and structured meshes were used to discretize the domain. The channel bed was fixed in both the physical experiment and the numerical runs. To reduce computational costs, a coarse mesh was used for the straight section, whereas a fine mesh was used in the bend section, which is the region of interest for this study. The final grid resolution was determined based on a grid independency study. For example, when the amount of the computational cells was 1.2 million, and the number of cells was increased by approximately 300000 cells, the mean absolute percentage error between the velocities in the bend calculated on the previous mesh and those on the current mesh was around 1%. Finally, the mesh with 1595280 computational cells was adopted. In the meantime, a time independency test was also performed to make sure the computational running had reached a steady state. It can be seen from the figure 5A.1 that the velocity fluctuation of the selected points basically stays stable despite the calculation was still continuing.

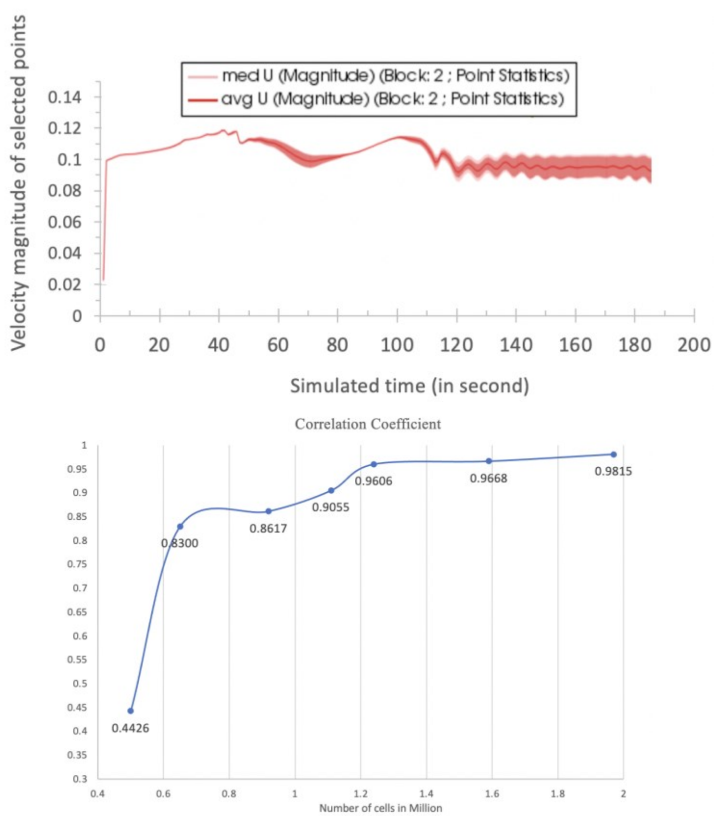

Figure 5A.1. Time independency test result (up) and Grid independency analysis (down)

The initial setting of boundary conditions upstream and downstream of a sample calculation of the numerical computational domain was given as follow in the table.

Table 5A.1 boundary conditions of the simulation

	Iinlet	***Outlet***	***jet***	***Atmos phere***	***Aottom***	***Inner wall***	***Outer wall***	***Rectangul ar weir***
Alp ha swa ter	zeroGradie nt	zeroGr adient	uniformFix edValue	symmet ry	zeroGradie nt	zeroGradie nt	zeroGradie nt	zeroGradie nt
ε	fixedValue; uniform 0.014	zeroGr adient	fixedValue; uniform 0.1	symmet ry	epsilonWall Function	epsilonWall Function	epsilonWall Function	epsilonWall Function
k	fixedValue uniform 0.1	zeroGr adient	fixedValue uniform 1	symmet ry	kqRWallFu nction	kqRWallFu nction	kqRWallFu nction	kqRWallFu nction
ν_t	zeroGradie nt	zeroGr adient	zeroGradie nt	symmet ry	nutkWallFu nction	nutkWallFu nction	nutkWallFu nction	nutkWallFu nction
ω	fixedValue	zeroGr adient	fixedValue	symmet ry	omegaWall Function	omegaWall Function	omegaWall Function	omegaWall Function
U	fixedValue uniform (0.1 0 0)	zeroGr adient	uniformFix edValue	symmet ry	noSlip	noSlip	noSlip	fixedValue

The grid conversion was made using the MATLAB toolbox, since the mesh was built based on the cartesian coordinate system. However, for better analysis, a local coordinate system was adopted in the subsequent analysis. The velocities in the streamwise, transverse and vertical direction were calculated by taking the projection of the component with the global coordinate system in x, y and z directions, respectively. There were four cross-sections in total. Consider 37-degree section for example, the code script for gird conversion is provided below.

```
A1 = xlsread(filename1);

x1=A1(:,17);
y1=A1(:,18);
z1=A1(:,19);
ux1=A1(:,5);
uy1=A1(:,6);
uz1=A1(:,7);

t=37*pi/180;   %t for slice angle 15=105-90
R = [cos(t),sin(t),0;-sin(t),cos(t),0 ; 0, 0, 1]; %stream u, trans v, vertical w

V=[ux1,uy1,uz1]';
Vn=(R*V)';
u=Vn(:,1)';
v=Vn(:,2)';
w=Vn(:,3)';

C=[x1,y1,z1]';
Vn2=(R*C)';
x=Vn2(:,1);
y=Vn2(:,2)';
z=Vn2(:,3)';


uu=u';
vv=v';
ww=w';
```

Figure 5A.2 A sample script of grid conversion

Chapter 6 Summary, Conclusions and Recommendations for Future Research

6.1 Summary and Conclusions

The present study aimed to investigate the influence of negatively buoyant jets discharging in a strongly curved open-channel bend. To accomplish this objective, this study was divided into three parts in this dissertation. The first part focused on physical modeling and data collection. The second part of the present study discussed the investigation of the underlying mechanisms of the influences that result from the negatively buoyant jets on the bend flow. The last goal of this research was to evaluate the performances of RANS turbulence models applied to this specific problem in OpenFOAM with the experimental data. It is important to know the area of application with different turbulence models and their accuracy for a better suggestion of engineering practices.

In the first part of this study (Chapter 3), a laboratory experiment was conducted to resemble an open-channel bend flow with the discharge of the negatively buoyant jets. Submerged discharges were selected for a higher mixing efficiency compared to the surface jets. The particle image velocimetry (PIV) technique was employed on a laboratory flume for a higher resolution of data acquisition. The long straight section design of the flume effectively eliminated the flow instability at the inlet section and was convenient to accurately verify the flow conditions. The fully transparent flume enabled the observation of the flow and the operation of the laser in the entire straight section (inlet and outlet) and the curved section of the flume. Diluted sodium chloride solution with three different salinity values was used as the effluent since it was readily available. Detailed experimental procedure was demonstrated in the corresponding part to ensure the replicability of the experiments.

In the second part of this study (Chapter 4), a term-by-term analysis of the downstream vorticity equation (derived from the momentum equation) was performed to reveal the relevant mechanisms behind the bend flow with negatively buoyant jets. A comparison between the simplified vorticity with the experimental data and the results calculated from the above-mentioned vorticity equation was made. Both the center region cell and the outer bank cell were investigated separately while the density varied due to salinity changes for each individual term. The objective of this section attempted to investigate, for the first time, the dependence of the circulation cells and their generating mechanism on effluents mixing in an open-channel bend.

The main idea of the third part is the application of an open-source code (OpenFOAM) to the bend flow with effluents discharged as submerged jets in fully 3D numerical modeling. The aim was to evaluate the performance of selected turbulence models for incompressible fluids with the jet density varying due to salinity changes and the flow behavior in open channel bend. There were two main issues in the numerical model. Those include, to consider the effluents distribution and to capture the flow structure. Among different turbulence models chosen for the current study, stability and accuracy are the primary influencing factors during the evaluation. Specifically, the numerical schemes for solving temporal, advection, and diffusion terms, as well as the controlling algorithms and solvers were carefully configurated and validated. Mesh type and sensitivity analyses were also conducted in the current study to eliminate the influence of mesh generation. To make a better comparison, parameters for the hydrodynamics of different cases were kept the same and compliance with the physical model. This study limited the scope of numerical work to the implementation and validation of the most popular RANS models. Therefore, the research requires further investigation.

The main conclusions may be summarized as follows:

- Multiple-cell patterns were captured in the experiment with different bend cross-sections, i.e., the center region cell, the outer bank counter-rotating cell, and the inner bank cell (also called the separation zone). The jets mainly affected the cell vorticity in the centre region at the beginning and the end of the bend, where the mixing process began and progressed, respectively. This is because of a dramatic increase in flow complexity just near the entry and exit of the bend. The failure to obtain a continuous variation on the secondary flow with respect to the increase of salinity results from the distinctive transport and mixing behavior of the dense jets in a bend.

- The maximum streamwise velocities and the depth-averaged velocities are hardly affected by the negatively buoyant jets discharged in the straight inflow portion of the bend, nevertheless, the maximum transverse and vertical velocities of the flow change with salinity.

- The centrifugal force contributes to the generation of the center region cells and the dissipation of both the center region cells and outer bank cells. The discharged jets interrupted the development of the center region cell but increased the outer bank cell vorticity. The cross-stream anisotropy and the turbulent shear stress terms oppose the center region cells, but their feedback to the salinity change does not illustrate a clear trend. In the outer bank cell, the values of these two terms do not reveal how the cross-stream turbulent stress generates or dissipates the downstream vorticity. The jet-induced turbulent stress favors the dissipation of the outer bank vorticity, although at different cross-sections, this attenuation of the outer bank cell varies.

- Kinetic energy transfer is dominated by the advective transfer caused by the secondary flow despite the existence of jet mixing. Increasing the salinity of the jet reduces the damping effect at the water's surface. However, the influence of the dense jet strengthens this damping effect at the side boundary.

- For lower salinity instances, all of the employed turbulence models provided accurate predictions of streamwise velocities, while failures in resolving the outer bank cell led to the discrepancies near the water surface in the outer bank region. In terms of transverse velocities, the numerical results and the measured data agree within a reasonable agreement. Specifically, the major computational differences were observed with the vertical velocity component. Overall, the k-ω SST model exhibited the best performance in the present study. The computational errors can be attributed to the use of the isotropic eddy viscosity and the rigid-lid free surface assumption.

- The overall shapes of streamlines at each salinity case are different from each other because of the interaction between the jet mixing behavior and the secondary flow are different in the channel bend. The developed secondary flow influenced the velocity patterns in all three directions, as shown by experimental data and numerical simulations. The presence of negatively buoyant jets disturbed the development of the outer bank cell, and the influence was attenuated as salinity increased. In the inner bank region, flow separation was strengthened by the participation of the negatively buoyant jets. The main circulation found at the lower inner bank was pushed towards the inner bank wall as salinity increased.

6.2 Recommendations for future research

The following recommendations are proposed for experimental and numerical modeling of jets influencing open-channel bend flow in future studies:

- The current study considered a flat bed with a strongly curved open channel to isolate and simplify the problems related to the streamline curvature with jets, however, flow behavior would significantly change with complex bend morphology, boundary roughness condition, effect of vegetation or even with ice on top. Therefore, it is worth investigating the capacity of the applied model with more complicated situation in the future.
- Positively buoyant jets have also received much research attention and are of great importance as negatively buoyant jets. Instead of moving downward in the

receiving waterbody, the trajectory goes up. The interaction could be totally different when discharging a positively buoyant jet into a bend flow.

- A wide range of numerical models have been applied for the cases considered in the current research, however, those models are limited in the scope of RANS-based turbulence models. More advanced models, such as DNS models, LES models, DES models, can be adopted to improve the prediction accuracy of the flow structure in bends.

References:

Ahmad, Nadeem, (2013), "Study of Vertical Dense Jet Dilution in a Marine Environment", Electronic Thesis and Dissertation Repository. 1524.

AL-Salem .S.S and Lumbers. J. P (1987), An initial evaluation of Al-Sumra Waste Stabilization Ponds in Jordan. Wat. Sci. Tech. 19(12). 33-37.

Bathurst, J. C., C. R. Thorne, and R. D. Hey (1977), Direct measurements of secondary currents in river bends, Nature, 269(5628), 504–506.

Blanckaert, K. (2009), Saturation of curvature-induced secondary flow, energy losses, and turbulence in sharp open-channel bends: Laboratory experiments, analysis, and modeling, J. Geophys. Res., 114.

Blanckaert, K.; Graf, W.H., (2001), Mean flow and turbulence in open-channel bend. J. Hydraul. Eng., 127, 835-847.

Booij, R. (2003), Measurements and large eddy simulations of the flows in some curved flumes, Journal of Turbulence, 4, doi:10.1088/1468-5248/4/1/008.

Boussinesq, J. (1868), M´emoire sur l’influence de frottement dans les mouvements r´eguliers des fluides; xii - essai sur le mouvement permanent d’un liquide dans un canal horizontal axe circulaire, J. Math. Pures Appl., 13(2).

Abad, J. D., and M. H. García (2009), Experiments in a high-amplitude Kinoshita meandering channel: 1. Implications of bend orientation on mean turbulent flow structure, Water Resour. Res., 45, W02401, doi:10.1029/2008WR007016.

Ferguson, R. I., Parsons, D. R., Lane, S. N., & Hardy, R. J. (2003). Flow in meander bends with recirculation at the inner bank. Water resources research, 39(11).

Andrle, R. (1994), Flow structure and development of circular meander pools, Geomorphology, 9, 261–270, doi:10.1016/0169-555X(94)90049-3.

Beltaos, S., Krishnappan, B. G., Rowsell, R., Carter, T., Pilling, R., & Bergeron, P. E. (2012). Flow structure and channel stability at the site of a deep scour hole, Mackenzie Delta, Canada. Arctic, 182-194.

Hey RD, Thorne CR. 1975. Secondary flows in river channels. Area 7(3): 191–195.

Bathurst JC, Thorne CR, Hey RD. 1977. Direct measurements of second- ary currents in river bends. Nature 269(5628): 504–506. DOI:10.1038/ 269504a0.

Markham AJ, Thorne CR. 1992. Geomorphology of gravel-bed river bends. In Dynamics of Gravel-bed Rivers, Billi P, Hey RD, Thorne CR, Tacconi P (eds). John Wiley & Sons: Chichester; 433–456.

Engel, F. L., & Rhoads, B. L. (2016). Three - dimensional flow structure and patterns of bed shear stress in an evolving compound meander bend. Earth Surface Processes and Landforms, 41(9), 1211-1226.

Brunner, G. W. (2006). HEC-RAS, river analysis system user’s manual: Version 4.0, U.S. Army Corps of Engineers, Hydrologic Engineer Center, Davis, Calif.

Chen, Y. L., & Hsiao, S. C. (2018). Numerical modeling of a buoyant round jet under regular waves. Ocean Engineering, 161, 154-167.

Cheng, G. C., and Farokhi, S.(1992). “On turbulent flows dominated by curvature effects.”J. Fluid Engrg., ASME, 114(1), 52–57.

Cipolina A. ,Brucato A.,Grisafi F. et al., (2005), Bench-scale investigation of inclined dense jets. J.Hydraul Eng ASCE 131(11):1017–1022.

de Vriend, H. J. (1977), A mathematical model of steady flow in curved shallow channels, J. Hydr. Res., 15(1), 37–54.

Drami D, Yacobi YZ, Stambler N, Kress N (2011) Seawater quality and microbial communities at a desalination plant marine outfall. A field study at the Israeli Mediterranean coast. Water Res 45(17):5449–5462

Duan, J. G., and P. Y. Julien (2005), Numerical simulation of the inception of channel mean- dering, Earth Surface Processes and Landforms, 30(9), 1093–1110.

Frothingham, K. M., and B. L. Rhoads (2003), Three‐dimensional flow structure and channel change in an asymmetrical compound meander loop, Embarras River, Illinois, Earth Surf. Processes Landforms, 28, 625‐644.

G. Alfonsi, (2009), Reynolds-averaged Navier–Stokes equations for turbulence modelling, Appl. Mech. Rev. 62 1–20.

Gao M, Huai WX, Li YT, Wang WJ (2017) Numerical study of the flow and dilution behaviors of round buoyant jet in counterflow. J Hydrodyn 29(1):172–175.

Gawad, S. T., et al. (1996). “Near-field mixing at an outfall.” Can. J. Civ. Eng., 23(1).

Ghaisas, Niranjan Shrinivas, (2013). "Subgrid Scale Modeling for Large Eddy Simulation of Buoyant Turbulent Flows", Open Access Dissertations. 152.

Graftieaux, L., Michard, M. & Grosjean, N. (2001), Combining PIV, POD and vortex identification algorithms for the study of unsteady turbulent swirling flows. Meas. Sci. Technol. 12, 1422–1429.

Hickin, E. J. (1978), Mean flow ‐ structure in meanders of the Squamish River, British Columbia, Can. J. Earth Sci., 15(11), 1833 ‐ 1849.

HK Schreiner, CD Rennie, A Mohammadian (2018), Trajectory of a jet in crossflow in a channel bend, Environmental Fluid Mechanics 18 (6), 1301-1319.

Huang, J. V., and Greimann, B. P. (2007). User’s manual for SRH-1D V2.0, Sedimentation and River Hydraulics Group, Technical Service Center, Bureau of Reclamation, Denver,

Ivanova, B.E. Noll, M. Aigner , (2013), A numerical study on the turbulent Schmidt numbers in a jet in crossflow, J. Eng. Gas Turbines Power, 135.

J. Ziefle, L. Kleiser, (2013), Numerical investigation of a film-cooling flow structure: effect of crossflow turbulence, J. Turbomach., 135 (4) pp. 041001:1-12

Jamieson, G Post, CD Rennie (2010), Spatial variability of three ‐ dimensional Reynolds stresses in a developing channel bend, Earth surface processes and Landforms 35 (9), 1029-1043.

Jiang, B., Law, A. W. K., and Lee, J. H. W. (2014). “Mixing of 30° and 45° inclined dense jets in shallow coastal waters.” J. Hydraul. Eng., 10.1061/(ASCE)HY.1943-7900.0000819, 241–253.

Jirka, G. H. (2004). "Integral Model for Turbulent Buoyant Jets in Unbounded Stratified Flows Part 1: Single Round Jet." Journal of Environmental Fluid Mechanics(4), 1-56.

Johannesson, H., and G. Parker (1989b), Velocity redistribution in meandering rivers, J. Hydr. Engng, 115 (8), 1019–1039.

Jones, G. R., Nash, J. D., Doneker, R. L., and Jirka, G. H. (2007). “Buoyant surface discharges into water bodies. I: Flow classification and prediction methodology.” J. Hydraul. Eng., 10.1061/(ASCE)0733-9429(2007)133:9(1010), 1010–1020.

Jordinson, R. (1956). "Flow in a jet directed normal to a wind." Technical Report R & M, 3074.

Kashyap, S. (2012), A 3 - D numerical study of flow, coherent structures and mechanisms leading to scour in a high curvature 135° channel bend with and without submerged groynes, Ph.D. Thesis, Dep. of Civil Eng., University of Ottawa, Ottawa, ON.

Keffer, J. F., and Baines, W. D. (1963). "The round turbulent jet in a cross-wind." Journal of Fluid Mechanics, 15(4), 481-497.

Kikkert, G.A., Davidson, M.J., Nokes, R.I. (2007a). Inclined negatively buoyant discharges. J. Hydraulic Eng. 133(5), 545–554.

Kikkert, G.A., Davidson, M.J. & Nokes, R.I. (2007b). Characterizing strongly advected discharges in the initial dilution zone. Environ Fluid Mech 7, 23–41.

Lai CCK, Lee JHW (2012) Mixing of inclined dense jets in stationary ambient. J Hydro-environ Res, 6:9–28

Launder, B.E.; Spalding, D.B. (March 1974). "The numerical computation of turbulent flows". Computer Methods in Applied Mechanics and Engineering. 3 (2): 269–289.

M. Rudman. (1996), Simulation of the near field of a jet in a cross flow. Experimental Thermal and Fluid Science, 12(2):134–141.

M.F. EI-Amin, S. Sun, W. Heidemann, H. Müller-steinhagen, (2010), Analysis of a turbulent buoyant confined jet modeled using realizable k-ϵ model, J. Heat Mass Transfer, 46, pp. 943-960.

Martínez-Legazpi, P., Rodríguez-Rodríguez, J., Marugán-Cruz, C. & Lasheras, J. C., (2013), Plunging to spilling transition in corner surface waves in the wake of a partially submerged vertical plate. Exp. Fluids 54 (1), 1–11.

Milione M, Zeng C (2008) The effects of temperature and salinity on population growth and egg hatching success of the tropical calanoid copepod, Acartia sinjiensis. Aquaculture 275(1–4):116–123

Morton, B. R., G. I. Taylor, and J. S. Turner (1956), Turbulent gravitational convection from maintained and instantaneous source, Proc. R. Soc.Lond., 234, 1–23.

N. Ahmad, R.E. Baddour, (2012), Dilution and penetration of vertical negatively buoyant thermal jets, J. Hydraulic Eng., 138 (10), pp. 850-857

Nanson, R. A. (2010), Flow fields in tightly curving meander bends of low width-depth ratio, Earth Surf. Process and Landforms, 35(2), 119–135.

Ottevanger, W., K. Blanckaert, and W. S. J. Uijttewaal (2012), Processes governing the flow redistribution in sharp river bends, Geomorphology, 163-164, 44–45, Meandering Channels.

Ottevanger, W., K. Blanckaert, W. S. J. Uijttewaal, and H. J. De Vriend (2013), Meander dynamics: A reduced order non‐linear model without curvature restrictions for flow and bed morphology, J. Geophys. Res., 118, 1118‐ 1131.

Palomar, P., Lara, J. L., Losada, I. J., Rodrigo, M., and Alvárez, A. (2012). "Near field brine discharge modeling. Part 1: Analysis of commercial tools." Desalin., 290, 14–27.

Prasad A K and Jensen K, (1995), Scheimpflug stereocamera for particle image velocimetry in liquid flows Appl. Opt. 34 7092-9.

R. S. Rogallo and P. Moin, (1984), Numerical simulation of turbulent flows, Ann. Rev. Fluid Mech. 16, 99-127

Reichardt,H. (1942) Gesetzmässsigkeiten der freien turbulenz. VDIForschungsheft 414 (2. Auflage 1051)

Roberts, P. J. W., and Toms, G. (1987). "Inclined dense jets in flowing current." Journal of Hydraulic Engineering, 113(3), 323-341.

Roberts, P. J. W., Ferrier, A., and Daviero, G. (1997). "Mixing in inclined dense jets." Journal of Hydraulic Engineering, 123(8), 693-699.

Salewski, M., Stankovic, D., & Fuchs, L. (2008). Mixing in Circular and Non-circular Jets in Crossflow. Flow, Turbulence and Combustion, 80, 255-283.

Sau, A., Sheu, T.W.H., Hwang, R.R. and Yang, W.C., (2004a), Three-dimensional simulation of square jets in cross-flow. Phys. Rev. E.

Scorer, R. S. (1959). "Behaviour of chimney plumes." International Journal of Air Pollution, 1(3), 198-220.

Song, C. G., I. W. Seo, and Y. D. Kim (2012), Analysis of secondary current effect in the modeling of shallow flow in open channels, Advances in Water Resources, 41, 29–48.

Stoesser, T., N. Ruether, and N. R. B. Olsen (2010), Calculation of primary and secondary flow and boundary shear stresses in a meandering channel, Adv. Water Resour., 33(2), 158–170.

Struiksma, N., Olesen, K. W., Flokstra, C., and de Vriend, H. J. (1985). Bed deformation in curved alluvial channels.'' J. Hydr. Res., Delft,The Netherlands, 23, 57–79.

Tchobanoglous, G. (1979) Waste Water Engineering: Treatment Disposal Reuse. 2nd Edition, McGraw-Hill, New York.

Tennekes, H.; Lumley, J. L. (1972). A First Course in Turbulence. MIT Press.

Weller H.G., Tabor G., Jasak H., Fureby C., (1998), A tensorial approach to computational continuum mechanics using object-oriented techniques, Computers in Physics, 12, p. 620

Yang X, Sotiropoulos F, Conzemius RJ, Wachtler JN, Strong MB (2014) Large-eddy simulation of turbulent flow past wind turbines/farms: the virtual wind simulator (VWiS). Wind Energy 18:2025–2045.

Abduo, S. S., Elmoustafa, A. M., & Salam, M. S. A. (2021). Study of counteracting the secondary flow in open channel bends. Ain Shams Engineering Journal, 12(3), 2425-2433.

Ahadiyan, J., & Musavi-Jahromi, S. H. (2009). Effects of jet hydraulic properties on geometry of trajectory in circular buoyant jets in the static ambient flow.

Ahmad, N. (2013). Study of Vertical Dense Jet Dilution in a Marine Environment.

Ahmad, N., & Baddour, R. E. (2014). A review of sources, effects, disposal methods, and regulations of brine into marine environments. Ocean & coastal management, 87, 1-7.

Akar, P. J., & Jirka, G. H. (1990). CORMIX2: An Expert System for Hydrodynamic Mixing Zone Analysis of Conventional and Toxic Multiport Diffuser Discharges. July 1990 Draft Report. Environmental Research Laboratory, USEPA, Athens, GA.

AL-Salem. S.S and Lumbers. J. P (1987), An initial evaluation of Al-Sumra Waste Stabilization Ponds in Jordan. Wat. Sci. Tech. 19(12). 33-37.

Albertson, M., Dai, Y., Jensen, R., & Rouse, H. (1950). Diffusion of Submerged Jets. Transactions Of The American Society Of Civil Engineers, 115(1), 639-664. doi: 10.1061/taceat.0006302

Alfonsi, G. (2009). Reynolds-averaged Navier–Stokes equations for turbulence modeling. Applied Mechanics Reviews, 62(4).

Aris, R. (1956). On the dispersion of a solute in a fluid flowing through a tube. Proceedings of the Royal Society of London. Series A. Mathematical and Physical Sciences, 235(1200), 67-77.

Atkins, M. D. (2016). Velocity field measurement using particle image velocimetry (PIV). In Application of Thermo-Fluidic Measurement Techniques (pp. 125-166). Butterworth-Heinemann.

Bai, R., Zhu, D., Chen, H., & Li, D. (2019). Laboratory study of secondary flow in an open channel bend by using PIV. Water, 11(4), 659.

Bai, Y., Song, X., & Gao, S. (2014). Efficient investigation on fully developed flow in a mildly curved 180 open-channel. Journal of Hydroinformatics, 16(6), 1250-1264.

Vaghefi, M., Akbari, M., & Fiouz, A. R. (2016). An experimental study of mean and turbulent flow in a 180 degree sharp open channel bend: Secondary flow and bed shear stress. KSCE Journal of Civil Engineering, 20(4), 1582-1593.

Bashitialshaaer, R., Larson, M., & Persson, K. M. (2013). An experimental study to improve the design of brine discharge from desalination plants. American Journal of Environmental Protection, 2(6), 176-182.

Bathurst, J. C., Thorne, C. R., & Hey, R. D. (1977). Direct measurements of secondary currents in river bends. Nature, 269(5628), 504-506.

Blanckaert, K. (2009), Saturation of curvature-induced secondary flow, energy losses, and turbulence in sharp open-channel bends: Laboratory experiments, analysis, and modeling, J. Geophys. Res., 114, F03015, doi:10.1029/2008JF001137.

Blanckaert, K. (2015). Flow separation at convex banks in open channels. Journal of Fluid Mechanics, 779, 432-467.

Blanckaert, K. D. V. H., & De Vriend, H. J. (2004). Secondary flow in sharp open-channel bends. Journal of Fluid Mechanics, 498, 353-380.

Blanckaert, K. D. V. H., & De Vriend, H. J. (2005). Turbulence structure in sharp open-channel bends. Journal of Fluid Mechanics, 536, 27-48.

Blanckaert, K., and H. J. de Vriend (2003), Nonlinear modeling of mean flow redistribution in curved open channels, Water Resour. Res., 39(12), 1375, doi:10.1029/2003WR002068.

Blanckaert, K., and W. H. Graf (2001), Experiments on flow in an open-channel bend. Mean flow and turbulence, J. Hydraul. Eng., 127(10), 835–847.

Blanckaert, K., and W. H. Graf (2004), Momentum transport in sharp open-channel bends, J. Hydraul. Eng., 130(3), 186–198, doi:10.1061/(ASCE)0733-9429(2004)130:3(186).

Blanckaert, K., Duarte, A., Chen, Q., & Schleiss, A. J. (2012). Flow processes near smooth and rough (concave) outer banks in curved open channels. Journal of Geophysical Research: Earth Surface, 117(F4).

Blanckaert, K., I. Schnauder, A. Sukhodolov, W. van Balen, and W. Uijttewaal (2010), Meandering: Field experiments, laboratory experiments and numerical modeling, in River, Coastal and Estuarine Morphodynamics: RCEM 2009, edited by C. A. Vionnet, M. H. Garcia, E. M. Latrubesse, and G. M. E. Perillo, Taylor & Francis Group, London, ISBN 978-0-415-55426-8.

Booij, R. (2003). Measurements and large eddy simulations of the flows in some curved flumes. Journal of turbulence, 4(1), 008.

Boussinesq, J. (1877). Theorie de l'ecoulement tourbillant. Mem. Acad. Sci., 23, 46.

Boxall, J.B., Guymer, I., & Marion, A. (2003). Transverse mixing in sinuous natural open channel flows. Journal of Hydraulic Research, 41, 153 - 165.

Bridge J S, Jarvis J. Flow and sedimentary processes in the meandering river South Esk, Glen Clova, Scotland[J]. Earth Surface Processes & Landforms, 2010, 1(4):303-336.

Nezu, I., & Nakagawa, H. (2017). Turbulence in open-channel flows. Routledge.

Perkins, H. J. (1970). The formation of streamwise vorticity in turbulent flow. Journal of Fluid Mechanics, 44(4), 721-740.

Townsend, P., Walters, K., & Waterhouse, W. M. (1976). Secondary flows in pipes of square cross-section and the measurement of the second normal stress difference. Journal of Non-Newtonian Fluid Mechanics, 1(2), 107-123.

Calaf, M., Meneveau, C., & Meyers, J. (2010). Large eddy simulation study of fully developed wind-turbine array boundary layers. Physics of fluids, 22(1), 015110.

Cavar, D., Meyer, K. E., Jakirlić, S., & Šarić, S. (2010). LES Based POD Analysis of Jet in Cross Flow. In Direct and Large-Eddy Simulation VII (pp. 253-259). Springer, Dordrecht.

Chen, Y. L., & Hsiao, S. C. (2018). Numerical modeling of a buoyant round jet under regular waves. Ocean Engineering, 161, 154-167.

Cheng, G. C., & Farokhi, S. (1992). On turbulent flows dominated by curvature effects. ASME J. Fluid Eng. 114, 52–57.

Christensen, K. T. (2004). The influence of peak-locking errors on turbulence statistics computed from PIV ensembles. Experiments in fluids, 36(3), 484-497.

Choi, Y., Stewart, J. P., & Graves, R. W. (2005). Empirical model for basin effects accounts for basin depth and source location. Bulletin of the Seismological Society of America, 95(4), 1412-1427.

Cipollina, A., Brucato, A., Grisafi, F., & Nicosia, S. (2005). Bench-scale investigation of inclined dense jets. Journal of Hydraulic Engineering, 131(11), 1017-1022.

Colt, J., & Tchobanoglous, G. (1978). Chronic exposure of channel catfish, Ictalurus punctatus, to ammonia: Effects on growth and survival. Aquaculture, 15(4), 353–372. https://doi.org/10.1016/0044-8486(78)90081-9

Christensen HB, Gislason K, Fredsoe J (1999) Secondary turbulent flow in an infinite bend. In: The 1st RCEM Symposium, University of Genova, Genova, Italy (1), pp 543–553

Constantinescu, G., Kashyap, S., Tokyay, T., Rennie, C. D., & Townsend, R. D. (2013). Hydrodynamic processes and sediment erosion mechanisms in an open channel bend of strong curvature with deformed bathymetry. Journal of Geophysical Research: Earth Surface, 118(2), 480-496.

Constantinescu, G., Koken, M., & Zeng, J. (2011). The structure of turbulent flow in an open channel bend of strong curvature with deformed bed: Insight provided by detached eddy simulation. Water Resources Research, 47(5).

Daly, B. J., & Harlow, F. H. (1970). Transport equations in turbulence. The physics of fluids, 13(11), 2634-2649.

de Vriend, H. J. (1977), A mathematical model of steady flow in curved shallow channels, J. Hydraul. Res, 15(1), 37–54.

de Vriend, H. J. (1981), Steady flow in shallow channel bends, Rep. 81-3, Fluid Mech. Lab., Dep. of Civ. Eng., Delft Univ. of Technol., Delft, Netherlands.

Demuren, A. O., & Rodi, W. (1986). Calculation of flow and pollutant dispersion in meandering channels. Journal of fluid mechanics, 172, 63-92.

Dietrich, W. E., & Whiting, P. (1989). Boundary shear stress and sediment transport in river meanders of sand and gravel. River meandering, 12, 1-50.

Doneker, R. L., & Jirka, G. H. (1990). Expert system for hydrodynamic mixing zone analysis of conventional and toxic submerged single port discharges (CORMIX1). Cornell University Ithaca United States.

Duan, J.G. (2004). Simulation of flow and mass dispersion in meandering channels. Journal of Hydraulic Engineering, 130, 964-976.

Einstein, H. A., & Harder, J. A. (1954). Velocity distribution and the boundary layer at channel bends. Eos, Transactions American Geophysical Union, 35(1), 114-120.

Einstein, H. A., & Li, H. (1958). Secondary currents in straight channels. Eos, Transactions American Geophysical Union, 39(6), 1085-1088.

El-Amin, M. F., Sun, S., Heidemann, W., & Müller-Steinhagen, H. (2010). Analysis of a turbulent buoyant confined jet modeled using realizable k–ε model. Heat and mass transfer, 46(8), 943-960.

Engel, F. L., & Rhoads, B. L. (2017). Velocity profiles and the structure of turbulence at the outer bank of a compound meander bend. Geomorphology, 295, 191-201.

Engelund, F. (1974). Flow and bed topography in channel bends. Journal of the Hydraulics Division, 100(11), 1631-1648.

Engelund, F., & Skovgaard, O. (1973). On the origin of meandering and braiding in alluvial streams. Journal of Fluid Mechanics, 57(2), 289-302.

ENGELUND, F., Flow and bed topography in channel bends, Proc. ASCE, Jnl. Hydr. Div., 100, HYl 1, Nov.1974, p. 1631.

Engman, E. T. (1986). Roughness coefficients for routing surface runoff. Journal of Irrigation and Drainage Engineering, 112(1), 39-53.

Engman, E. T., Jackson, T. J., & Schmugge, T. J. (1983, January). Implications of complete watershed soil moisture measurements to hydrologic modeling. In 1983 International Geoscience and Remote Sensing Symposium (IGARSS"83).

Esfahani, F. S., & Keshavarzi, A. (2020). Circulation cells topology and their effect on migration pattern of different multi-bend meandering rivers. International Journal of Sediment Research, 35(6), 636-650.

Falcon, M. (1984). Secondary flow in curved open channels. Annual Review of Fluid Mechanics, 16(1), 179-193.

Farhadi et al 2018, An investigation on the outer bank cell of secondary flow in channel bends. Journal of Hydro-environment Research 18 (2018) 1–11

Farhadi, A., Sindelar, C., Tritthart, M., Glas, M., Blanckaert, K., & Habersack, H. (2018). An investigation on the outer bank cell of secondary flow in channel bends. Journal of Hydro-Environment Research, 18, 1-11.

Fischer, 'H. B. 1969. Cross-sectional time scales and dispersion in estuaries. Proc. Congr. Int. Assoc. Hydraul. Res., 13th, 3:173-80

FISCHER, A. G., SCHULZ, A. R., & OLINER, L. (1968). Distribution of monoamine oxidase in the thyroid gland. Endocrinology, 82(6), 1098-1102.

Fric, T. F., & Roshko, A. (1994). Vortical structure in the wake of a transverse jet. Journal of Fluid Mechanics, 279, 1-47.

Frothingham, K.M. and Rhoads, B.L. (2003), Three-dimensional flow structure and channel change in an asymmetrical compound meander loop, Embarras River, Illinois. Earth Surf. Process. Landforms, 28: 625-644. https://doi.org/10.1002/esp.471

Gao, M., Huai, W. X., Li, Y. T., & Wang, W. J. (2017). Numerical study of the flow and dilution behaviors of round buoyant jet in counterflow. Journal of Hydrodynamics, Ser. B, 29(1), 172-175.

Gawad, S. A., McCorquodale, J. A., & Gerges, H. (1996). Near-field mixing at an outfall. Canadian Journal of Civil Engineering, 23(1), 63-75.

Ghaisas, N. S., Shetty, D. A., & Frankel, S. H. (2015). Large eddy simulation of turbulent horizontal buoyant jets. Journal of Turbulence, 16(8), 772-808.

Gholami, A., Akhtari, A. A., Minatour, Y., Bonakdari, H., & Javadi, A. A. (2014). Experimental and numerical study on velocity fields and water surface profile in a strongly-curved 90° open channel bend. Engineering Applications of Computational Fluid Mechanics, 8(3), 447–461.

Abhari, M. N., Ghodsian, M., Vaghefi, M., & Panahpur, N. (2010). Experimental and numerical simulation of flow in a 90 bend. Flow Measurement and Instrumentation, 21(3), 292-298.

Chin, D. A. 2006. Water-resources engineering. 2nd ed. Upper Saddle River, NJ: Prentice.

Kirkgöz, M. S., and M. Ardiçhoğlu. 1997. "Velocity profiles of developing and developed open channel flow." J. Hydraul. Eng. 123 (12): 1099 – 1105. https://doi.org/10.1061/(ASCE)0733-9429(1997)123:12(1099).

Graftieaux, L., Michard, M., & Grosjean, N. (2001). Combining PIV, POD and vortex identification algorithms for the study of unsteady turbulent swirling flows. Measurement Science and technology, 12(9), 1422.

Heng Xiao, Jian-Xun Wang, Roger G. Ghanem, A random matrix approach for quantifying model-form uncertainties in turbulence modeling, Computer Methods in Applied Mechanics and Engineering,Volume 313, 2017,Pages 941-965, ISSN 0045-7825, https://doi.org/10.1016/j.cma.2016.10.025.

Hey R D, Thorne C R. Secondary Flows in River Channels[J]. Area, 1975, 7(3):191-195.

Hickin E J. Mean flow structure in meanders of the Squamish River, British Columbi. [J]. Canadian Journal of Earth Sciences, 1978, 15(11):1833-1849.

Hopkins, L., Kelly, J., Wexler, A. et al. Particle image velocimetry measurements in complex geometries. Experiments in Fluids 29, 91–95 (2000). https://doi.org/10.1007/s003480050430

Hu, C., Yu, M., Wei, H., & Liu, C. (2019). The mechanisms of energy transformation in sharp open-channel bends: Analysis based on experiments in a laboratory flume. Journal of Hydrology, 571, 723-739.

Hu, C., Yu, M., Wei, H., & Liu, C. (2019). The mechanisms of energy transformation in sharp open-channel bends: Analysis based on experiments in a laboratory flume. Journal of Hydrology, 571, 723-739.

Huang, N.E., Wu, Z., Long, S.R., Arnold, K.C., Blank, K., Liu, T.W., 2009. On instantaneous frequency. Advances in Adaptive D ata Analysis 1(2), 177-229.

Ikeda, S., Yamasaka, M., & Chiyoda, M. (1987). Bed topography and sorting in bends. Journal of Hydraulic Engineering, 113(2), 190-204.

Ivanova, E. M., Noll, B. E., & Aigner, M. (2011). Computational modeling of turbulent mixing of a transverse jet. Journal of engineering for gas turbines and power, 133(2).

Ivanova, E. M., Noll, B. E., & Aigner, M. (2013). A numerical study on the turbulent Schmidt numbers in a jet in crossflow. Journal of Engineering for Gas Turbines and Power, 135(1).

Jackson R G. Velocity-bed-form-texture patterns of meander bends in the lower Wabash River of Illinois and Indiana[J]. Geological Society of America Bulletin, 1975, 86(11):

Jamieson, E. C., Post, G., & Rennie, C. D. (2010). Spatial variability of three - dimensional Reynolds stresses in a developing channel bend. Earth surface processes and Landforms, 35(9), 1029-1043.

Jeon, T.M., Baek, K.O. & Seo, I.W. Development of an empirical equation for the transverse dispersion coefficient in natural streams. Environ Fluid Mech 7, 317–329 (2007). https://doi.org/10.1007/s10652-007-9027-6

Jiang, M., Law, A. W. K., & Zhang, S. (2018). Mixing behavior of 45 inclined dense jets in currents. Journal of hydro-environment research, 18, 37-48.

Jirka, G. H. (1982). Multiport diffusers for heat disposal: a summary. Journal of the Hydraulics Division, 108(12), 1423-1468.

Jirka, G. H. (2004). Integral model for turbulent buoyant jets in unbounded stratified flows. Part I: Single round jet. Environmental Fluid Mechanics, 4(1), 1-56.

Jirka, G. H., Doneker, R. L., & Barnwell, T. O. (1991). CORMIX: an expert system for mixing zone analysis. Water Science and Technology, 24(6), 267-274.

Jirka, G.H., & Doneker, R.L. (1991). Hydrodynamic Classification of Submerged Single - Port Discharges. Journal of Hydraulic Engineering, 117, 1095-1112.

Johannesson, H., and G. Parker (1989a), Secondary flow in a mildly sinuous channel, J. Hydraul. Eng., 115(3), 289–308.

Jones, G. R., & Jirka, G. H. (1991). Classification and prediction of buoyant surface discharges. In Proceedings of the 1991 national conference on hydraulic engineering.

Kalkwijk, J. T., & De Vriend, H. J. (1980). Computation of the flow in shallow river bends. Journal of Hydraulic Research, 18(4), 327-342.

Kashyap, S.; Constantinescu, G.; Rennie, C.D.; Post, G.; Townsend, R. Influence of channel aspect ratio and curvature on flow, secondary circulation, and bed shear stress in a rectangular channel bend. J. Hydraul. Eng. 2012, 138, 1045–1059

Kawai, S., & Julien, P. Y. (1996). Point bar deposits in narrow sharp bends. Journal of Hydraulic Research, 34(2), 205-218.

Keffer, J. F., & Baines, W. D. (1963). The round turbulent jet in a cross-wind. Journal of Fluid Mechanics, 15(4), 481-496.

Khosronejad, A., Rennie, C. D., Salehi Neyshabouri, S. A. A., & Townsend, R. D. (2007). 3D numerical modeling of flow and sediment transport in laboratory channel bends. Journal of hydraulic Engineering, 133(10), 1123-1134.

Kikkawa, H., S. Ikeda, and A. Kitagawa (1976), Flow and bed topography in curved open channels, J. Hydraul. Eng. Am. Soc. Civ. Eng., 102(9), 1327–1342.

Lai, (2010), Two-Dimensional Depth-Averaged Flow Modeling with an Unstructured Hybrid Mesh, J. Hydraul. Eng., 2010, 136(1): 12-23.

Lai, C. C., & Lee, J. H. (2012). Mixing of inclined dense jets in stationary ambient. Journal of hydro-environment research, 6(1), 9-28.

Lai, Y. G. (2010). Two-dimensional depth-averaged flow modeling with an unstructured hybrid mesh. Journal of Hydraulic Engineering, 136(1), 12-23.

Leopold, L. B., & Wolman, M. G. (1960). River meanders. Geological Society of America Bulletin, 71(6), 769-793.

Leschziner, M. A., & Rodi, W. (1979). Calculation of strongly curved open channel flow. Journal of the Hydraulics Division, 105(10), 1297-1314.

Li, B., & Zhang, X. (2022). Evolution of outer bank cell in open-channel bends. Environmental Fluid Mechanics, 1-28.

Lu, W. Z., Zhang, W. S., Cui, C. Z., & Leung, A. Y. T. (2004). A numerical analysis of free-surface flow in curved open channel with velocity–pressure-free-surface correction. Computational Mechanics, 33(3), 215-224.

Metcalf & Eddy, Inc. (1979). Wastewater engineering: treatment, disposal, reuse. Tata McGraw-Hill.

Metcalf, L., Eddy, H. P., & Tchobanoglous, G. (1991). Wastewater engineering: treatment, disposal, and reuse (Vol. 4). New York: McGraw-Hill.

Millero, F. J., & Poisson, A. (1981). International one-atmosphere equation of state of seawater. Deep Sea Research Part A. Oceanographic Research Papers, 28(6), 625-629.

Moncho-Esteve, I. J., Folke, F., García-Villalba, M., & Palau-Salvador, G. (2017). Influence of the secondary motions on pollutant mixing in a meandering open channel flow. Environmental Fluid Mechanics, 17(4), 695-714.

Moncho-Esteve, I. J., García-Villalba, M., Muto, Y., Shiono, K., & Palau-Salvador, G. (2018). A numerical study of the complex flow structure in a compound meandering channel. Advances in Water Resources, 116, 95-116.

Morton, B. R., G. I. Taylor, and J. S. Turner (1956), Turbulent gravitational convection from maintained and instantaneous source, Proc. R. Soc.Lond., 234, 1–23.

Mosonyi, E., & Götz, W. (1973). Secondary currents in subsequent model bends. IN: SEDIMENT TRANSPORTATION, VOLUME 1.

Muppidi, S. (2006). Direct numerical simulations and modeling of jets in crossflow. Ph. D. Thesis.

Nanson, R., Nanson, G. C. & Huang, H. (2010). The hydraulic geometry of narrow and deep channels; evidence for flow optimisation and controlled peatland growth. Geomorphology, 117 (1-Feb), 143-154.

Nikora, V. and Roy, A.G. (2012). Secondary Flows in Rivers: Theoretical Framework, Recent Advances, and Current Challenges. In Gravel-Bed Rivers (eds M. Church, P.M. Biron and A.G. Roy). https://doi.org/10.1002/9781119952497.ch1

Njenga K.W. , Kioko K. J., Wanjiru G. P. (2013), Secondary Current and Classification of River Channels, Applied Mathematics, 4, 70-78

Odgaard, A. J. (1986), Meander flow model. I: Development, J. Hydraul. Eng., 112(12), 1117–1136.

Odgaard, A. J., & Bergs, M. A. (1988). Flow processes in a curved alluvial channel. Water Resources Research, 24(1), 45-56.

Oliver, C. J., Davidson, M. J., & Nokes, R. I. (2013). Removing the boundary influence on negatively buoyant jets. Environmental Fluid Mechanics, 13(6), 625-648.

Ottevanger, W., Blanckaert, K., & Uijttewaal, W. S. (2011). A parameter study on bank shear stresses in curved open channel flow by means of large-eddy simulation. In Proceedings of the 7th IAHR Symposium on River, Costal and Estuarine Morphodynamics (RCEM2011) (No. CONF, pp. 1917-1927). Tsinghua Univesity.

Ottevanger, W., Blanckaert, K., & Uijttewaal, W. S. (2012). Processes governing the flow redistribution in sharp river bends. Geomorphology, 163, 45-55.

Palomar, P., Lara, J. L., & Losada, I. J. (2012). Near field brine discharge modeling part 2: Validation of commercial tools. Desalination, 290, 28-42.

Patankar, S. V., & Spalding, D. B. (1972). Exhibition Road. A calculation procedure for heat, mass and momentum transfer in 3D parabolic flows. Journal of Clinical Neurophysiology, 19(5), 454-60.

Patankar, S. V., Pratap, V. S., & Spalding, D. B. (1975). Prediction of turbulent flow in curved pipes. Journal of Fluid Mechanics, 67(3), 583-595.

Pilechi, A., Mohammadian, A., Rennie, C. D., & Zhu, D. Z. (2016). Efficient method for coupling field data and numerical modeling for the estimation of transverse mixing coefficients in meandering rivers. Journal of Hydraulic Engineering, 142(6), 04016009.

Prandtl, L. (1925). 7. Bericht ü ber Untersuchungen zur ausgebildeten Turbulenz. ZAMM ‐ Journal of Applied Mathematics and Mechanics/Zeitschrift für Angewandte Mathematik und Mechanik, 5(2), 136-139.

Prasad, A. K., & Jensen, K. (1995). Scheimpflug stereocamera for particle image velocimetry in liquid flows. Applied optics, 34(30), 7092-7099.

Reichardt,H. (1942) Gesetzmässsigkeiten der freien turbulenz. VDIForschungsheft 414 (2. Auflage 1051)

Roberts, P. J., & Toms, G. (1987). Inclined dense jets in flowing current. Journal of Hydraulic Engineering, 113(3), 323-340.

Roberts, P. J., Ferrier, A., & Daviero, G. (1997). Mixing in inclined dense jets. Journal of Hydraulic Engineering, 123(8), 693-699.

Rogallo, R. S., & Moin, P. (1984). Numerical simulation of turbulent flows. Annual review of fluid mechanics, 16(1), 99-137.

Rotta, J. C. (1951). Statistische theorie nichthomogener turbulenz. Zeitschrift für Physik, 129(6), 547-572.

Rozovskii, I. L. (1957), Flow of Water in Bends of Open Channels, 233 pp., Acad. Sci.d of Ukraine, Kiev.

Russell P, Vennell R (2019) High resolution observations of an outer-bank cell of secondary circulation in a natural river bend. J Hydraul Eng 145(5):1–10

Rüther, N., & Olsen, N. R. (2005). Three-dimensional modeling of sediment transport in a narrow 90 channel bend. Journal of Hydraulic Engineering, 131(10), 917-920.

Salewski, M., Stankovic, D., & Fuchs, L. (2008). Mixing in circular and non-circular jets in crossflow. Flow, Turbulence and Combustion, 80(2), 255-283.

Sau, A., Sheu, T. W., Tsai, S. F., Hwang, R. R., & Chiang, T. P. (2004). Structural development of vortical flows around a square jet in cross-flow. Proceedings of the Royal Society of London. Series A: Mathematical, Physical and Engineering Sciences, 460(2051), 3339-3368.

Schlichting, H., Gersten, K. (2000). Onset of Turbulence (Stability Theory). In: Boundary-Layer Theory. Springer, Berlin, Heidelberg. https://doi.org/10.1007/978-3-642-85829-1_15

Schlüter, J. U., & Schönfeld, T. (2000). LES of jets in cross flow and its application to a gas turbine burner. Flow, Turbulence and Combustion, 65(2), 177-203.

Schnauder, I. and Sukhodolov, A.N. (2012), Flow in a tightly curving meander bend: effects of seasonal changes in aquatic macrophyte cover. Earth Surf. Process. Landforms, 37: 1142-1157. https://doi.org/10.1002/esp.3234

Schreiner, H. K., Rennie, C. D., & Mohammadian, A. (2018). Trajectory of a jet in crossflow in a channel bend. Environmental Fluid Mechanics, 18(6), 1301-1319.

Scorer, R. S. (1959). The rise of bent-over hot plumes. In Advances in Geophysics (Vol. 6, pp. 399-411). Elsevier.

Shaheed, R., Mohammadian, A., & Yan, X. (2021). A Review of Numerical Simulations of Secondary Flows in River Bends. Water, 13(7), 884.

Shukry, A. (1950). Flow around bends in an open flume. Transactions of the American Society of Civil Engineers, 115(1), 751-778.

Smith, R. (1983). Longitudinal dispersion coefficients for varying channels. Journal of Fluid Mechanics, 130, 299-314. doi:10.1017/S002211208300110X

Song Z.R., (2003), General Formula for Calculating Curve Circulation, Journal ofSediment Research,(4):5(In Chinese).

Song, C. G., I. W. Seo, and Y. D. Kim (2012), Analysis of secondary current effect in the modeling of shallow flow in open channels, Advances in Water Resources, 41, 29–48.

Stoesser, T., N. Ruether, and N. R. B. Olsen (2010), Calculation of primary and secondary flow and boundary shear stresses in a meandering channel, Adv. Water Resour., 33(2), 158–170.

Stone, M. C. and Hotchkiss, R. H. (2007). “Turbulence descriptions in two cobble-bed reaches.” J. Hydraul. Eng., Vol. 133, No. 12, pp. 1367–1378.

Struiksma, N., K. W. Olesen, C. Flokstra, and H. J. de Vriend (1985), Bed deformation in curved alluvial channels, J. Hydraul. Res., 23(1), 57–79.

Taylor, G. I. (1946). Dynamics of a mass of hot gas rising in air (Vol. 919). Technical Information Division, Oak Ridge Operations.

Termini, D. (2015). Momentum transport and bed shear stress distribution in a meandering bend: Experimental analysis in a laboratory flume. Advances in Water Resources, 81, 128-141.

Termini, D., & Piraino, M. (2011). Experimental analysis of cross‐sectional flow motion in a large amplitude meandering bend. Earth Surface Processes and Landforms, 36(2), 244-256.

Thomson, J. On the origin of the windings of rivers in alluvial plains, with remarks on the flow of water in pipes. Royal Soc. Lond. Proc. 1876, 25, 5–8.

Thorne, C. R., Zevenbergen, L. W., Pitlick, J. C., Rais, S., Bradley, J. B., & Julien, P. Y. (1985). Direct measurements of secondary currents in a meandering sand-bed river. Nature, 315(6022), 746-747.

Van Balen, W., Uijttewaal, W. S., & Blanckaert, K. (2009). Large-eddy simulation of a mildly curved open-channel flow. Journal of Fluid Mechanics, 630, 413-442.

Van Balen, W., Uijttewaal, W. S., & Blanckaert, K. (2010). Large-eddy simulation of a curved open-channel flow over topography. Physics of Fluids, 22(7), 075108.

Wang, X., Rennie, C. D., & Mohammadian, A. (2022). Experimental Studies on the Influence of Negatively Buoyant Jets on Flow Distribution in a 135-Degree Open Channel Bend. Water, 14(12), 1898.

Wei, M., Blanckaert, K., Heyman, J., Li, D., & Schleiss, A. J. (2016). A parametrical study on secondary flow in sharp open-channel bends: experiments and theoretical modelling. Journal of hydro-environment research, 13, 1-13.

Weller, H. G., Tabor, G., Jasak, H., & Fureby, C. (1998). A tensorial approach to computational continuum mechanics using object-oriented techniques. Computers in physics, 12(6), 620-631.

Westerweel, J., Elsinga, G. E., & Adrian, R. J. (2013). Particle image velocimetry for complex and turbulent flows. Annual Review of Fluid Mechanics, 45, 409-436.

Whiting, P. J., & Dietrich, W. E. (1993). Experimental studies of bed topography and flow patterns in large - amplitude meanders: 1. Observations. Water Resources Research, 29(11), 3605-3614.

Wilcox, D. C. (1994). Simulation of transition with a two-equation turbulence model. AIAA journal, 32(2), 247-255.

Wilcox, D. C. (1994). Turbulence Modeling for CFD. sl. DCW Industries, La Canada, Calif, USA.

Yan, X., & Mohammadian, A. (2017). Numerical modeling of vertical buoyant jets subjected to lateral confinement. Journal of Hydraulic Engineering, 143(7), 04017016.

Yan, X., Rennie, C. D., & Mohammadian, A. (2020). A three-dimensional numerical study of flow characteristics in strongly curved channel bends with different side slopes. Environmental Fluid Mechanics, 20(6), 1491-1510.

Ye, J., & McCorquodale, J. A. (1997). Three-dimensional numerical modelling of mass transport in curved channels. Canadian Journal of Civil Engineering, 24(3), 471-479.

Ye, J., & McCorquodale, J. A. (1998). Simulation of curved open channel flows by 3D hydrodynamic model. Journal of Hydraulic Engineering, 124(7), 687-698.

Ye, J., Mccorquodale, J. A., & Barron, R. M. (1998). A three‐dimensional hydrodynamic model in curvilinear co‐ordinates with collocated grid. International journal for numerical methods in fluids, 28(7), 1109-1134.

Yen, C. L., & Lee, K. T. (1995). Bed topography and sediment sorting in channel bend with unsteady flow. Journal of Hydraulic Engineering, 121(8), 591-599.

Yuan, L. L., & Street, R. L. (1998). Trajectory and entrainment of a round jet in crossflow. Physics of fluids, 10(9), 2323-2335.

Yuan, L. L., Street, R. L., & Ferziger, J. H. (1999). Large-eddy simulations of a round jet in crossflow. Journal of Fluid Mechanics, 379, 71-104.

Zeitoun, M. A., McIlhenny, W. F. and Reid, R. O. 1970. Conceptual designs of outfall systems for desalting plants. Res. and Devel. Progress Report, 550 Office of Saline Water, US Dept. of Interior, Washington DC

Zeitoun, M. A., Reid, R. O., McHilhenny, W. F., & Mitchell, T. M. (1972). Model studies of ocean outfall systems for desalination plants. Office of Saline Water, US Department of the Interior, Washington DC.

Zeng, J., Constantinescu, G., Blanckaert, K., & Weber, L. (2008). Flow and bathymetry in sharp open‐channel bends: Experiments and predictions. Water resources research, 44(9).

Zhang, S., Jiang, B., Law, A. W. K., & Zhao, B. (2016). Large eddy simulations of 45 inclined dense jets. Environmental Fluid Mechanics, 16(1), 101-121.

Zhu, H., Lu, S., Wang, L., Xu, J., & Yuan, S. (2022). Numerical Study of Mixing Process by Point Source Pollution with Different Release Positions in a Sinuous Open Channel. Water, 14(12), 1903.

Ziefle, J., & Kleiser, L. (2009). Large-eddy simulation of a round jet in crossflow. AIAA journal, 47(5), 1158-1172.

Zimmerman, C., & Kennedy, J. F. (1978). Transverse bed slopes in curved alluvial streams. Journal of the Hydraulics Division, 104(1), 33-48.